Electronic Supplementary Material (ESI) for Journal of Materials Chemistry A.

Amino Acids as Highly Efficient Modulators for Single Crystals of Zirconium and Hafnium Metal-Organic Frameworks

Ross J. Marshall,[a] Claire L. Hobday,[b] Colin F. Murphie,[a] Sarah L. Griffin,[a] Carole A. Morrison,[b] Stephen A. Moggach[b]* and Ross S. Forgan[a]*

[a]WestCHEM School of Chemistry, University of Glasgow, Joseph Black Building, University Avenue, Glasgow, G12 8QQ, UK.
Email: Ross.Forgan@glasgow.ac.uk
Web: http://www.forganlab.com

[b]EaSTCHEM School of Chemistry, University of Edinburgh, Joseph Black Building, West Mains Road, Edinburgh, EH9 3JJ, UK.
Email: s.moggach@ed.ac.uk
Web: http://www.moggach.chem.ed.ac.uk

SUPPORTING INFORMATION

Table of Contents

S1. General Experimental Remarks

All ligands, modulators, chemicals and solvents were purchased from Alfa Aesar, Acros Organics, Sigma-Aldrich and Tokyo Chemical Industry and used without further purification.

Powder X-ray Diffraction Experiments: PXRD measurements were carried out at 298 K using a PANalytical X'Pert PRO diffractometer (λ (CuKα) = 1.4505 Å) on a mounted bracket sample stage. Data were collected over the range 2Θ = 3 – 45 ° or 5 – 45 °. When comparison of the PXRD patterns was required, identical step size / scan speed parameters were used. (University of Glasgow)

Microwave Synthesis: Microwave reactions were performed in 35 ml pressure vials using a CEM Discover SP microwave, equipped with an Explorer 12 Hybrid autosampler. The power was allowed to fluctuate to maintain a constant temperature of 100 °C throughout the reaction. (University of Glasgow)

Single Crystal X-ray Diffraction: Data for **Hf-L6** were collected on Agilent Technologies SuperNova diffractometer using CuKα radiation, and data for **Hf-L7** were collected on a Bruker Apex II (λ (MoKα = 0.71073 Å) diffractometer (*University of Edinburgh).

Scanning Electron Microscopy: Powder samples were deposited onto conductive carbon tabs mounted on an aluminium stub and coated with Pd for 150 seconds using a Polaron SC7640 sputter coater. The prepared samples were transferred to and imaged using a Philips XL30 ESEM tungsten filament electron microscope, operating at an acceleration voltage of 20 Kv. (University of Glasgow)

Gas Uptake: N_2 adsorption isotherms were carried out at 77 K on a Quantachrome Autosorb iQ gas sorption analyser. Samples were degassed under vacuum at 120 °C for 20 hours using the internal turbo pump. BET surface areas were calculated from the isotherms using the Micropore BET Assistant and pore-size distribution analysis was carried out using QSDFT (N_2 on carbon at 77 K, slit/cylindrical pore model) both in the Quantachrome ASiQwin operating software. (University of Glasgow)

Thermal Gravimetric Analysis (TGA): Measurements were carried out using a TA Instruments Q500 Thermogravimetric Analyser. Measurements were collected from room temperature to 1000 °C with a heating rate of 10 °C / min under an N_2 atmosphere. (University of Glasgow)

Nuclear Magnetic Resonance (NMR): NMR spectra were recorded on either a Bruker AVIII 400 MHz spectrometer or a Bruker AVI 500 MHz Spectrometer and referenced to residual solvent peaks. (University of Glasgow)

S2. Amino Acid Modulation of Zr MOFs

The effect of amino acid modulation was examined using a general synthetic procedure for the Zr MOFs of **L1-L8**. A range of amino acids were utilised to examine the effect of size, charge and hydrophobicity on modulation in the synthesis of MOFs with general formula $[Zr_6O_4(OH)_4(\mathbf{L})_6]_n$, which we have shortened to **Zr-L** for convenience.

The amino acid (2.25 mmol, 5 eq) was added directly to a 50 ml Pyrex screw top jar followed by addition of $ZrCl_4$ (0.105 g, 0.45 mmol, 1 eq) as a 5 ml *N,N*-dimethylformamide (DMF, reagent grade) solution containing concentrated HCl (0.04 ml). The resulting mixture was sonicated for 5 minutes. The ligand (0.45 mmol, 1 eq) was subsequently added to the reaction flask as a DMF solution (5 ml). The reaction mixture was subject to sonication for a further 5 minutes to aid solvation of the reactants. The glass jar was placed in the oven at 120°C for a period of 24 hours before being removed and allowed to cool to room temperature. The products were added to centrifuge tubes and centrifuged for 20 minutes. The reaction DMF was decanted from the centrifuge tube and the product was subject to centrifugation a further three times, once with fresh DMF (30 ml) and twice with MeOH (2 x 30 ml). It was subsequently found that **Zr-L8** was sensitive to MeOH, and so in these cases the MeOH was replaced by acetone. The centrifuge tube was then placed in the desiccator under vacuum for a minimum of 24 hours where it remained until it was analysed by PXRD. Tables S1-S8 detail the exact masses of reagents used, while Figures S1-S8 show stacked PXRD patterns of the resulting material, allowing us to assess extent of modulation in each case.

Table S1. Amino acid modulated synthesis of **Zr-L1**.

L1		**$ZrCl_4$**		**HCl**	**Modulator**		
Moles (mmol)	**Mass (g)**	**Moles (mmol)**	**Mass (g)**	**Volume (ml)**	**Amino Acid**	**Moles (mmol)**	**Mass (g)**
0.45	0.0748	0.45	0.1049	0.04	unmodulated		
0.45	0.0748	0.45	0.1049	0.04	L-proline	2.25	0.2590
0.45	0.0748	0.45	0.1049	0.04	4-aminobenzoic acid	2.25	0.3086
0.45	0.0748	0.45	0.1049	0.04	beta alanine	2.25	0.2005
0.45	0.0748	0.45	0.1049	0.04	L-leucine	2.25	0.2952
0.45	0.0748	0.45	0.1049	0.04	L-tryptophan	2.25	0.4595
0.45	0.0748	0.45	0.1049	0.04	L-arginine	2.25	0.3920
0.45	0.0748	0.45	0.1049	0.04	DL-threonine	2.25	0.2680

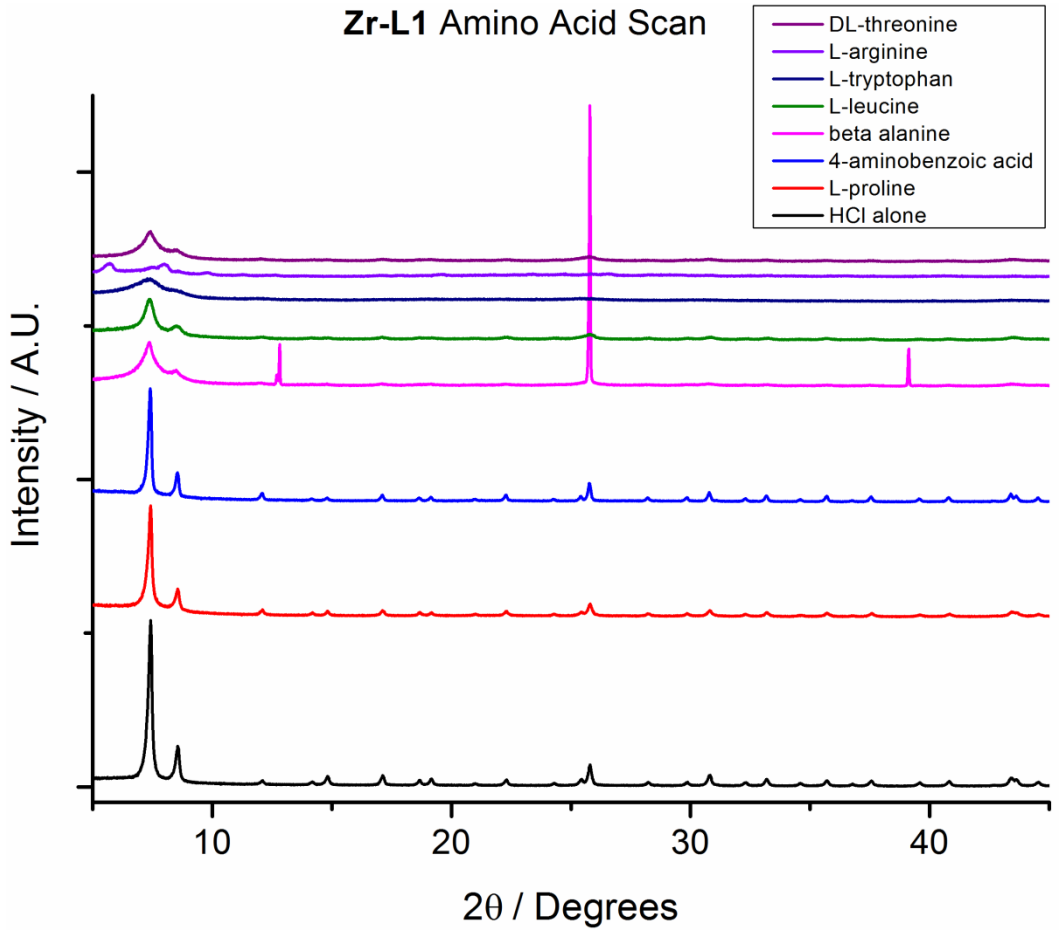

Figure S1. Stacked PXRD patterns for amino acid modulated syntheses of **Zr-L1**.

Table S2. Amino acid modulated synthesis of **Zr-L2**.

L2		$ZrCl_4$		HCl	Modulator		
Moles (mmol)	**Mass (g)**	**Moles (mmol)**	**Mass (g)**	**Volume (ml)**	**Amino Acid**	**Moles (mmol)**	**Mass (g)**
0.45	0.1103	0.45	0.1049	0.04	unmodulated		
0.45	0.1103	0.45	0.1049	0.04	L-proline	2.25	0.2590
0.45	0.1103	0.45	0.1049	0.04	4-aminobenzoic acid	2.25	0.3086
0.45	0.1103	0.45	0.1049	0.04	beta alanine	2.25	0.2005
0.45	0.1103	0.45	0.1049	0.04	L-leucine	2.25	0.2952
0.45	0.1103	0.45	0.1049	0.04	L-tryptophan	2.25	0.4595
0.45	0.1103	0.45	0.1049	0.04	L-arginine	2.25	0.3920
0.45	0.1103	0.45	0.1049	0.04	DL-threonine	2.25	0.2680

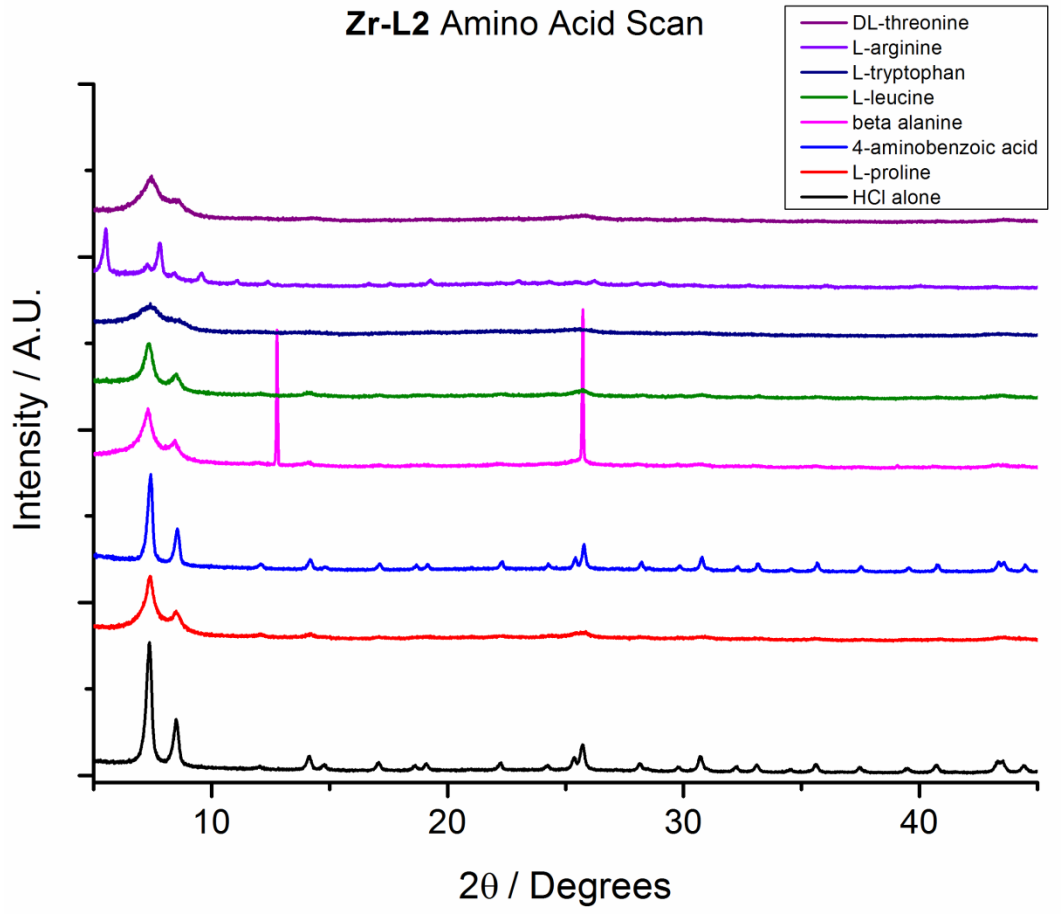

Figure S2. Stacked PXRD patterns for amino acid modulated syntheses of **Zr-L2**.

Table S3. Amino acid modulated synthesis of **Zr-L3**.

L3		$ZrCl_4$		HCl	Modulator		
Moles (mmol)	**Mass (g)**	**Moles (mmol)**	**Mass (g)**	**Volume (ml)**	**Amino Acid**	**Moles (mmol)**	**Mass (g)**
0.45	0.0950	0.45	0.1049	0.04	unmodulated		
0.45	0.0950	0.45	0.1049	0.04	L-proline	2.25	0.2590
0.45	0.0950	0.45	0.1049	0.04	4-aminobenzoic acid	2.25	0.3086
0.45	0.0950	0.45	0.1049	0.04	beta alanine	2.25	0.2005
0.45	0.0950	0.45	0.1049	0.04	L-leucine	2.25	0.2952
0.45	0.0950	0.45	0.1049	0.04	L-tryptophan	2.25	0.4595
0.45	0.0950	0.45	0.1049	0.04	L-arginine	2.25	0.3920
0.45	0.0950	0.45	0.1049	0.04	DL-threonine	2.25	0.2680

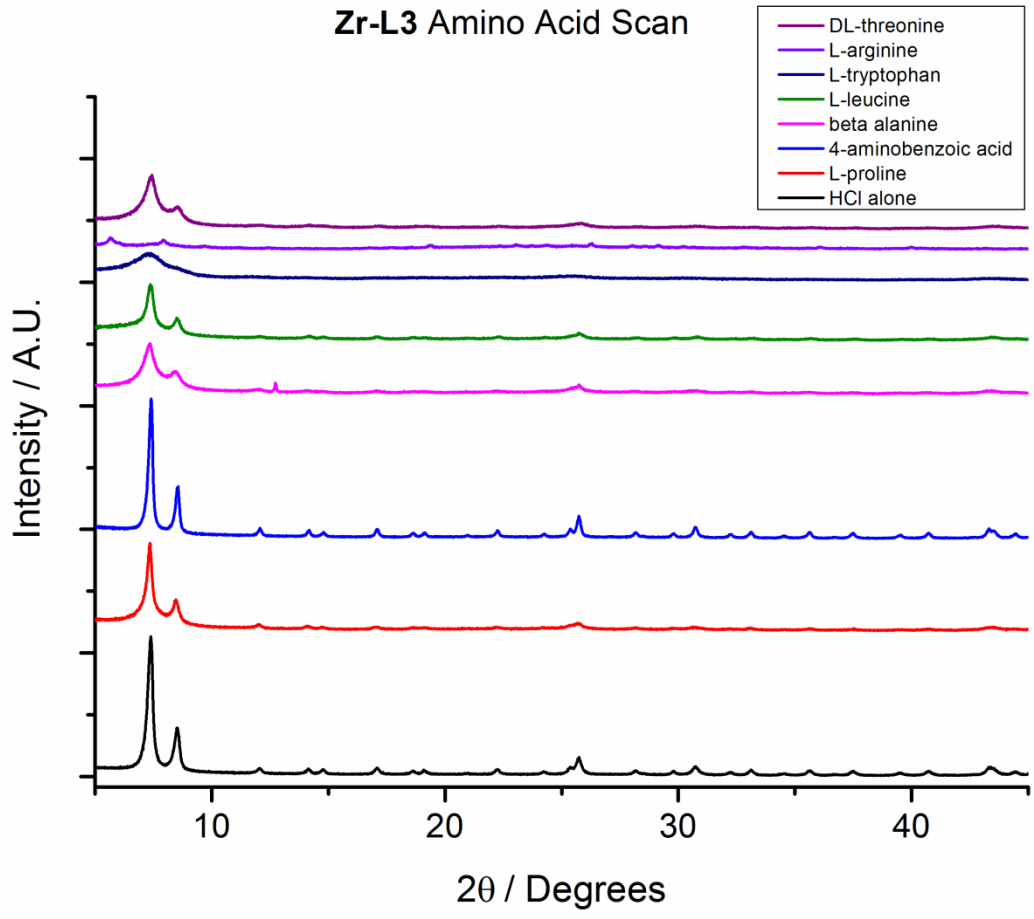

Figure S3. Stacked PXRD patterns for amino acid modulated syntheses of **Zr-L3**.

Table S4. Amino acid modulated synthesis of **Zr-L4**.

L4		$ZrCl_4$		HCl	Modulator		
Moles (mmol)	**Mass (g)**	**Moles (mmol)**	**Mass (g)**	**Volume (ml)**	**Amino Acid**	**Moles (mmol)**	**Mass (g)**
0.45	0.0815	0.45	0.1049	0.04	unmodulated		
0.45	0.0815	0.45	0.1049	0.04	L-proline	2.25	0.2590
0.45	0.0815	0.45	0.1049	0.04	4-aminobenzoic acid	2.25	0.3086
0.45	0.0815	0.45	0.1049	0.04	beta alanine	2.25	0.2005
0.45	0.0815	0.45	0.1049	0.04	L-leucine	2.25	0.2952
0.45	0.0815	0.45	0.1049	0.04	L-tryptophan	2.25	0.4595
0.45	0.0815	0.45	0.1049	0.04	L-arginine	2.25	0.3920
0.45	0.0815	0.45	0.1049	0.04	DL-threonine	2.25	0.2680

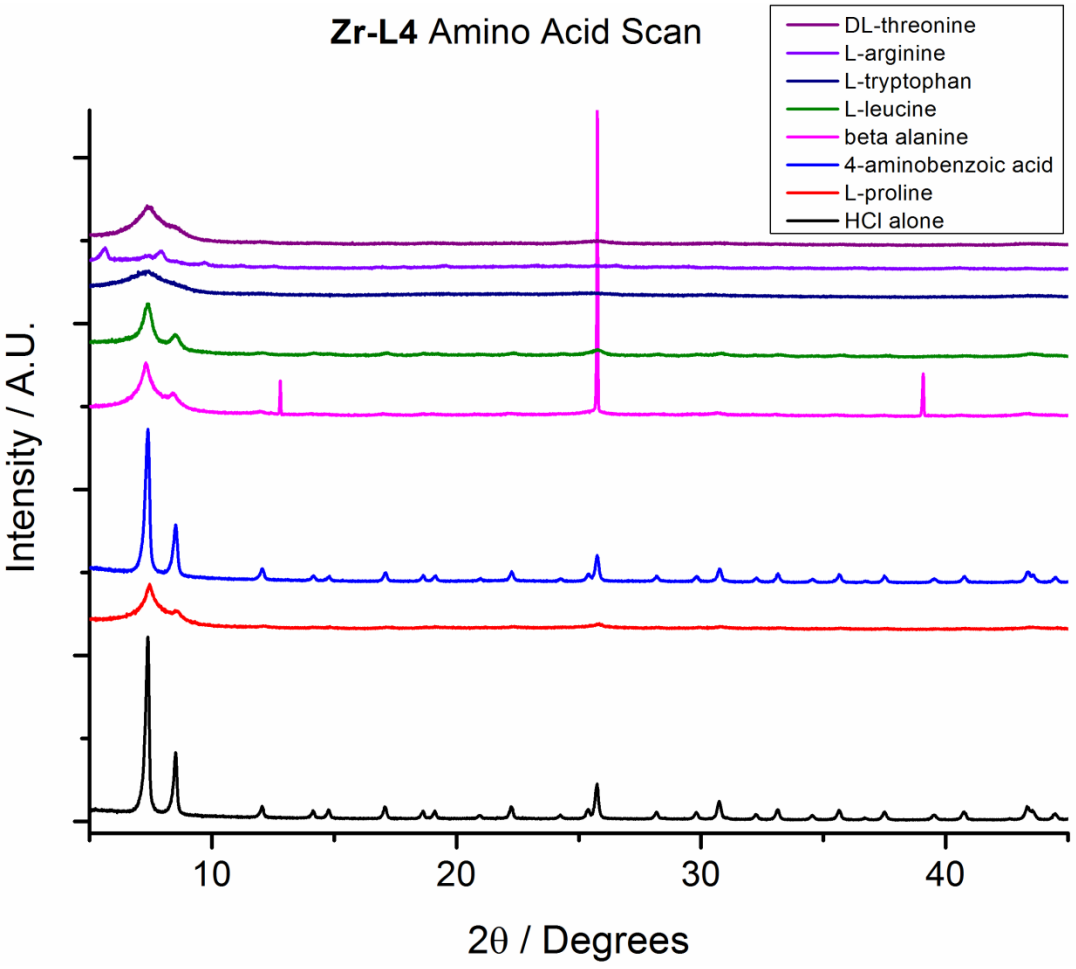

Figure S4. Stacked PXRD patterns for amino acid modulated syntheses of **Zr-L4**.

Table S5. Amino acid modulated synthesis of **Zr-L5**.

L5		$ZrCl_4$		HCl	Modulator		
Moles (mmol)	**Mass (g)**	**Moles (mmol)**	**Mass (g)**	**Volume (ml)**	**Amino Acid**	**Moles (mmol)**	**Mass (g)**
0.45	0.0973	0.45	0.1049	0.04	unmodulated		
0.45	0.0973	0.45	0.1049	0.04	L-proline	2.25	0.2590
0.45	0.0973	0.45	0.1049	0.04	4-aminobenzoic acid	2.25	0.3086
0.45	0.0973	0.45	0.1049	0.04	beta alanine	2.25	0.2005
0.45	0.0973	0.45	0.1049	0.04	L-leucine	2.25	0.2952
0.45	0.0973	0.45	0.1049	0.04	L-tryptophan	2.25	0.4595
0.45	0.0973	0.45	0.1049	0.04	L-arginine	2.25	0.3920
0.45	0.0973	0.45	0.1049	0.04	DL-threonine	2.25	0.2680

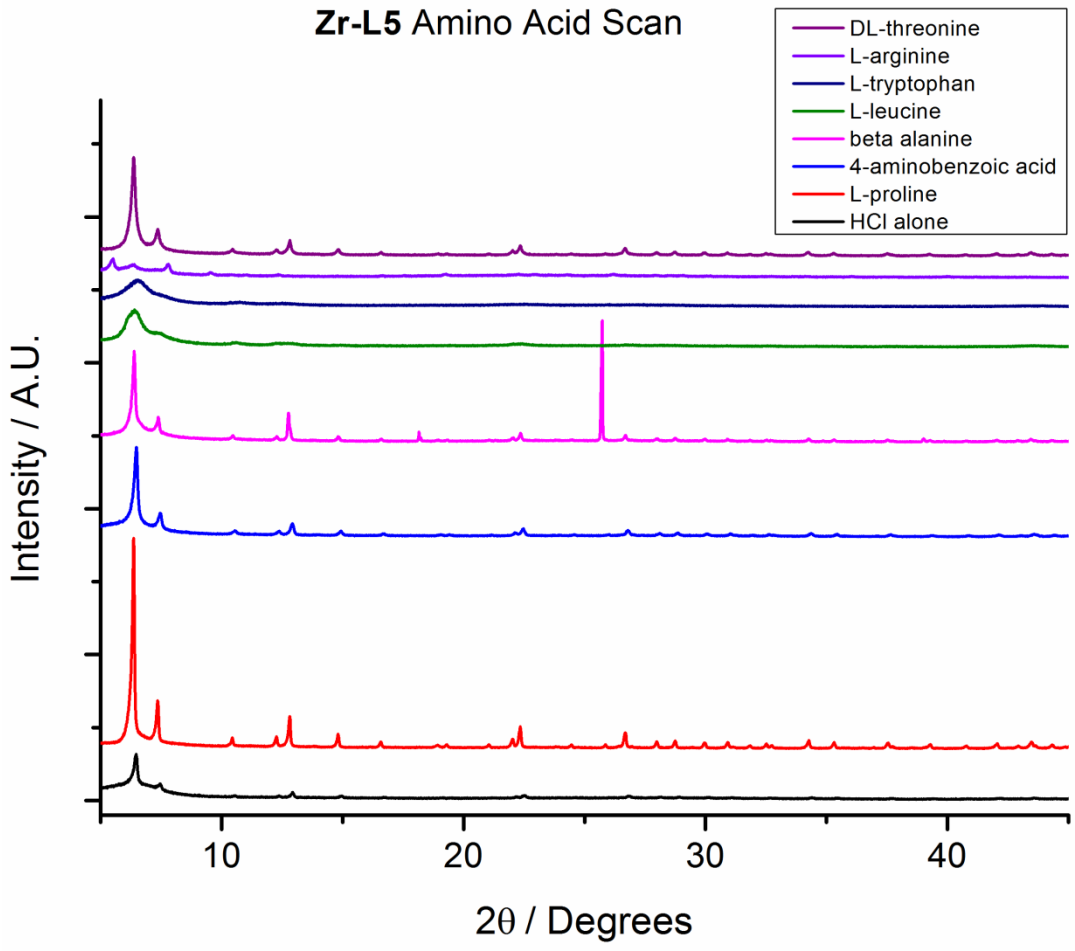

Figure S5. Stacked PXRD patterns for amino acid modulated syntheses of **Zr-L5**.

Table S6. Amino acid modulated synthesis of **Zr-L6**.

L6		$ZrCl_4$		HCl	Modulator		
Moles (mmol)	**Mass (g)**	**Moles (mmol)**	**Mass (g)**	**Volume (ml)**	**Amino Acid**	**Moles (mmol)**	**Mass (g)**
0.45	0.1090	0.45	0.1049	0.04	unmodulated		
0.45	0.1090	0.45	0.1049	0.04	L-proline	2.25	0.2590
0.45	0.1090	0.45	0.1049	0.04	4-aminobenzoic acid	2.25	0.3086
0.45	0.1090	0.45	0.1049	0.04	beta alanine	2.25	0.2005
0.45	0.1090	0.45	0.1049	0.04	L-leucine	2.25	0.2952
0.45	0.1090	0.45	0.1049	0.04	L-tryptophan	2.25	0.4595
0.45	0.1090	0.45	0.1049	0.04	L-arginine	2.25	0.3920
0.45	0.1090	0.45	0.1049	0.04	DL-threonine	2.25	0.2680

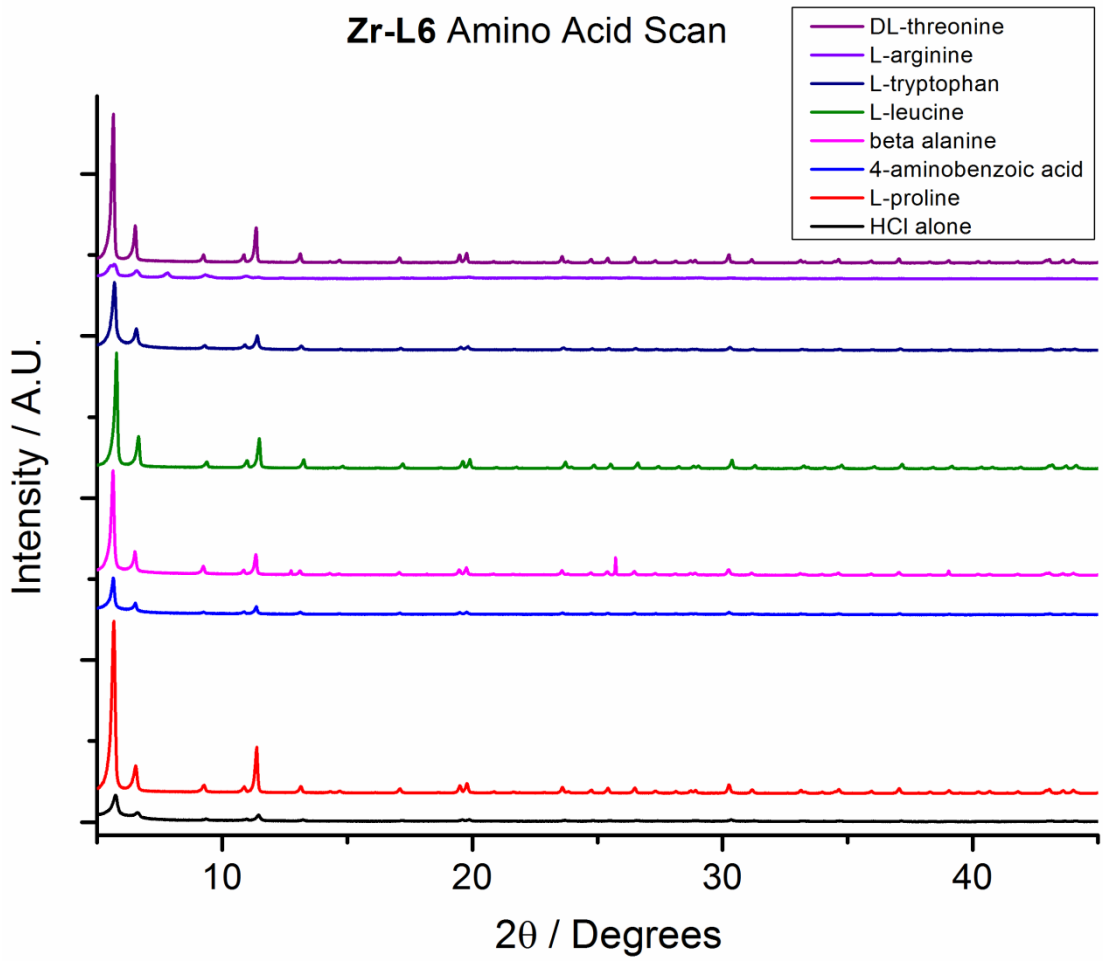

Figure S6. Stacked PXRD patterns for amino acid modulated syntheses of **Zr-L6**.

Table S7. Amino acid modulated synthesis of **Zr-L7**.

L7		$ZrCl_4$		HCl	Modulator		
Moles (mmol)	**Mass (g)**	**Moles (mmol)**	**Mass (g)**	**Volume (ml)**	**Amino Acid**	**Moles (mmol)**	**Mass (g)**
0.45	0.1216	0.45	0.1049	0.04	unmodulated		
0.45	0.1216	0.45	0.1049	0.04	L-proline	2.25	0.2590
0.45	0.1216	0.45	0.1049	0.04	4-aminobenzoic acid	2.25	0.3086
0.45	0.1216	0.45	0.1049	0.04	beta alanine	2.25	0.2005
0.45	0.1216	0.45	0.1049	0.04	L-leucine	2.25	0.2952
0.45	0.1216	0.45	0.1049	0.04	L-tryptophan	2.25	0.4595
0.45	0.1216	0.45	0.1049	0.04	L-arginine	2.25	0.3920
0.45	0.1216	0.45	0.1049	0.04	DL-threonine	2.25	0.2680

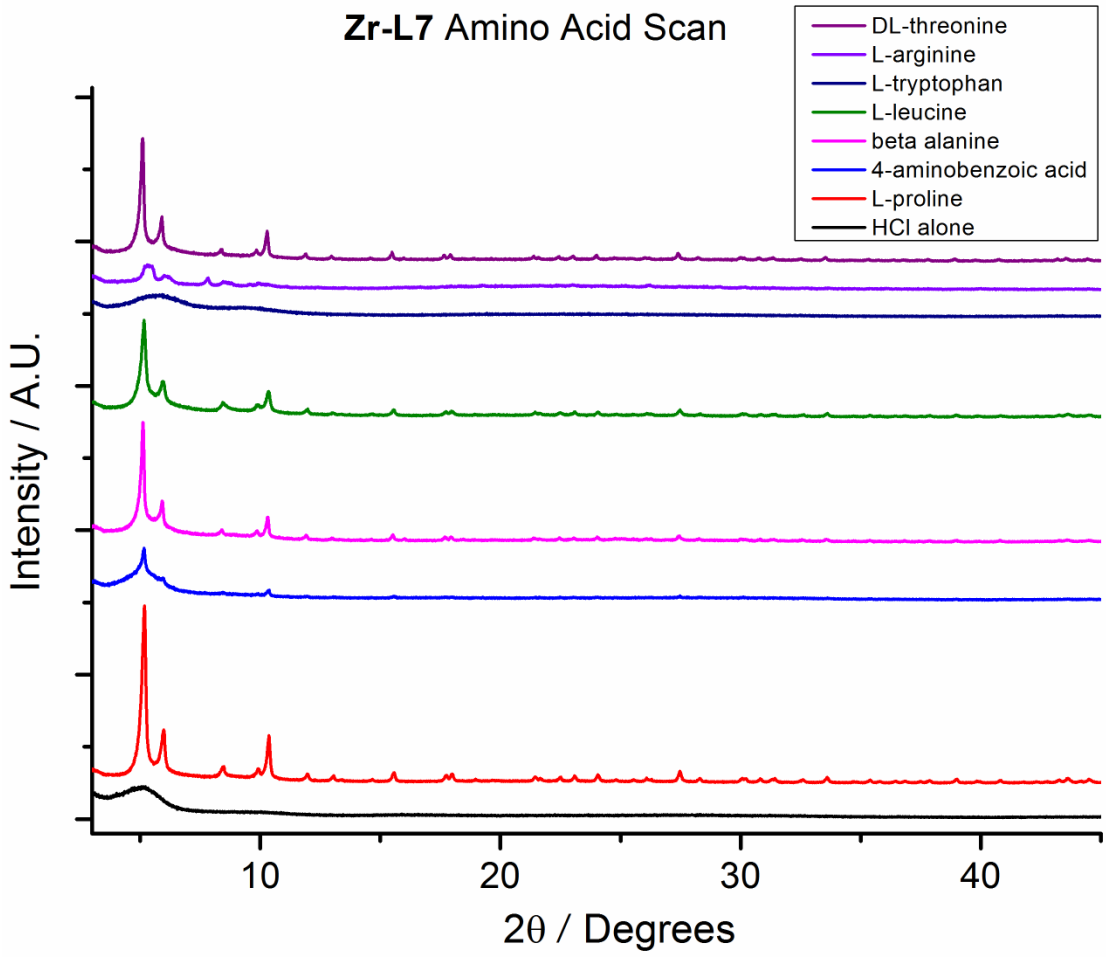

Figure S7. Stacked PXRD patterns for amino acid modulated syntheses of **Zr-L7**.

Table S8. Amino acid modulated synthesis of **Zr-L8**.

L8		$ZrCl_4$		HCl	Modulator		
Moles (mmol)	**Mass (g)**	**Moles (mmol)**	**Mass (g)**	**Volume (ml)**	**Amino Acid**	**Moles (mmol)**	**Mass (g)**
0.45	0.1207	0.45	0.1049	0.04	unmodulated		
0.45	0.1207	0.45	0.1049	0.04	L-proline	2.25	0.2590
0.45	0.1207	0.45	0.1049	0.04	4-aminobenzoic acid	2.25	0.3086
0.45	0.1207	0.45	0.1049	0.04	beta alanine	2.25	0.2005
0.45	0.1207	0.45	0.1049	0.04	L-leucine	2.25	0.2952
0.45	0.1207	0.45	0.1049	0.04	L-tryptophan	2.25	0.4595
0.45	0.1207	0.45	0.1049	0.04	L-arginine	2.25	0.3920
0.45	0.1207	0.45	0.1049	0.04	DL-threonine	2.25	0.2680

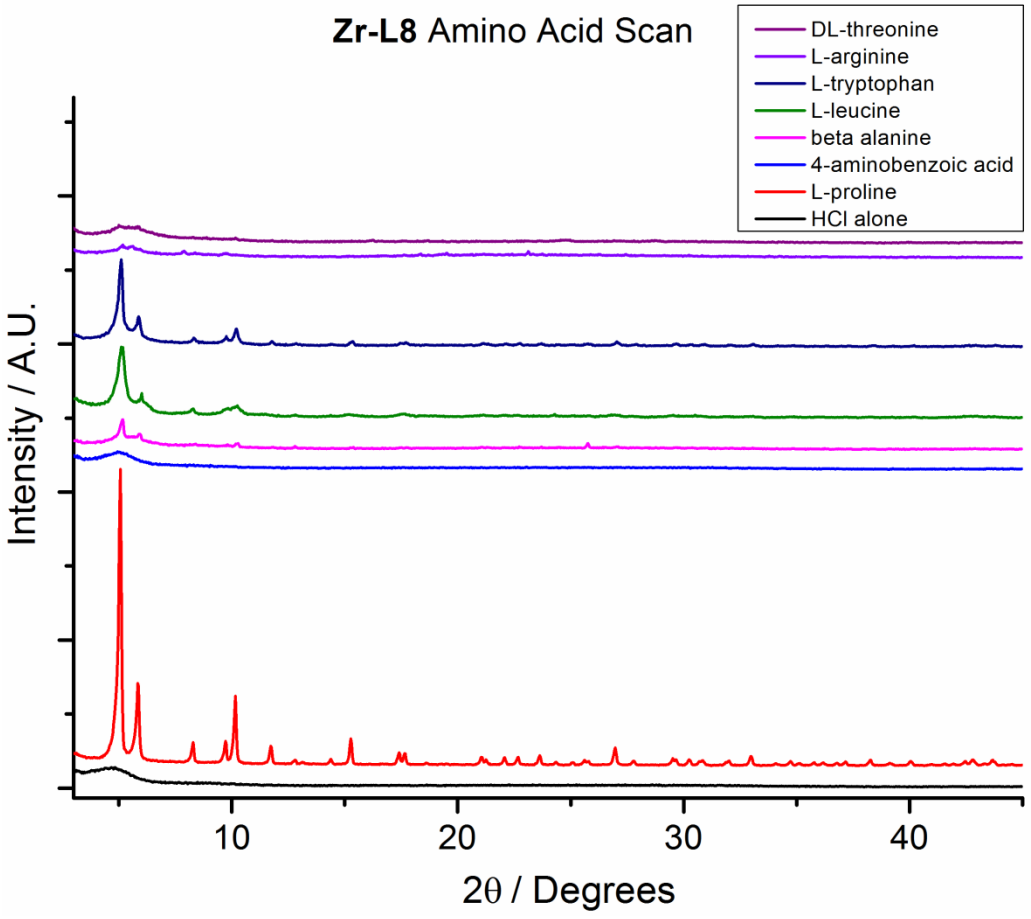

Figure S8. Stacked PXRD patterns for amino acid modulated syntheses of **Zr-L8**.

The results have been summarised in Table S9.

Table S9. Summary of amino acid modulation of Zr MOFs.

	Modulator						
	L-proline	4-amino benzoic acid	beta alanine	L-leucine	L-trytophan	L-arginine	DL-threonine
L1	•	•	—	—	—	—	—
L2	—	•	—	—	—	—	—
L3	—	•	—	—	—	—	—
L4	—	•	—	—	—	—	—
L5	+	+	+	—	—	—	+
L6	+	•	+	+	+	—	+
L7	+	•	+	+	•	•	+
L8	+	•	•	+	+	•	•
Key: + represents enhanced crystallinity, — represents a decline in crystallinity, • represents very little effect on crystallinity compared with the HCl-only sample.							

In general, there was no benefit to using amino acid modulators in the syntheses of the zirconium terephthalate MOFs of **L1-L4**. One equivalent of HCl alone in the syntheses was enough to induce formation of crystalline material, and addition of amino acids actually inhibited the formation of the MOFs, except in the case of 4-aminobenzoic acid, which was tolerated but did not enhance crystallinity.

For the Zr MOFs of the longer linkers, **L5-L8**, clear improvements in crystallinity were observed for a number of amino acid modulators. No clear pattern emerges other than the fact that smaller, hydrophobic amino acids such as L-proline and L-leucine were the most efficient modulators. When L-arginine is incorporated into the MOF syntheses, sticky gums rather than fine powders resulted. As L-proline gave the best results for all the Zr MOFs of **L5-L8**, it was taken forward as the amino acid of choice for modulation of the MOFs.

S3. SEM Images of Zr-L5, Zr-L6, Zr-L7 and Zr-L8

The effect of L-proline modulation of MOF morphology was examined using SEM. The Zr-MOFs synthesised solvothermally in the presence of five equivalents of L-proline and one equivalent of HCl, as described in Section S2, were sputtered with Pd and imaged by SEM.

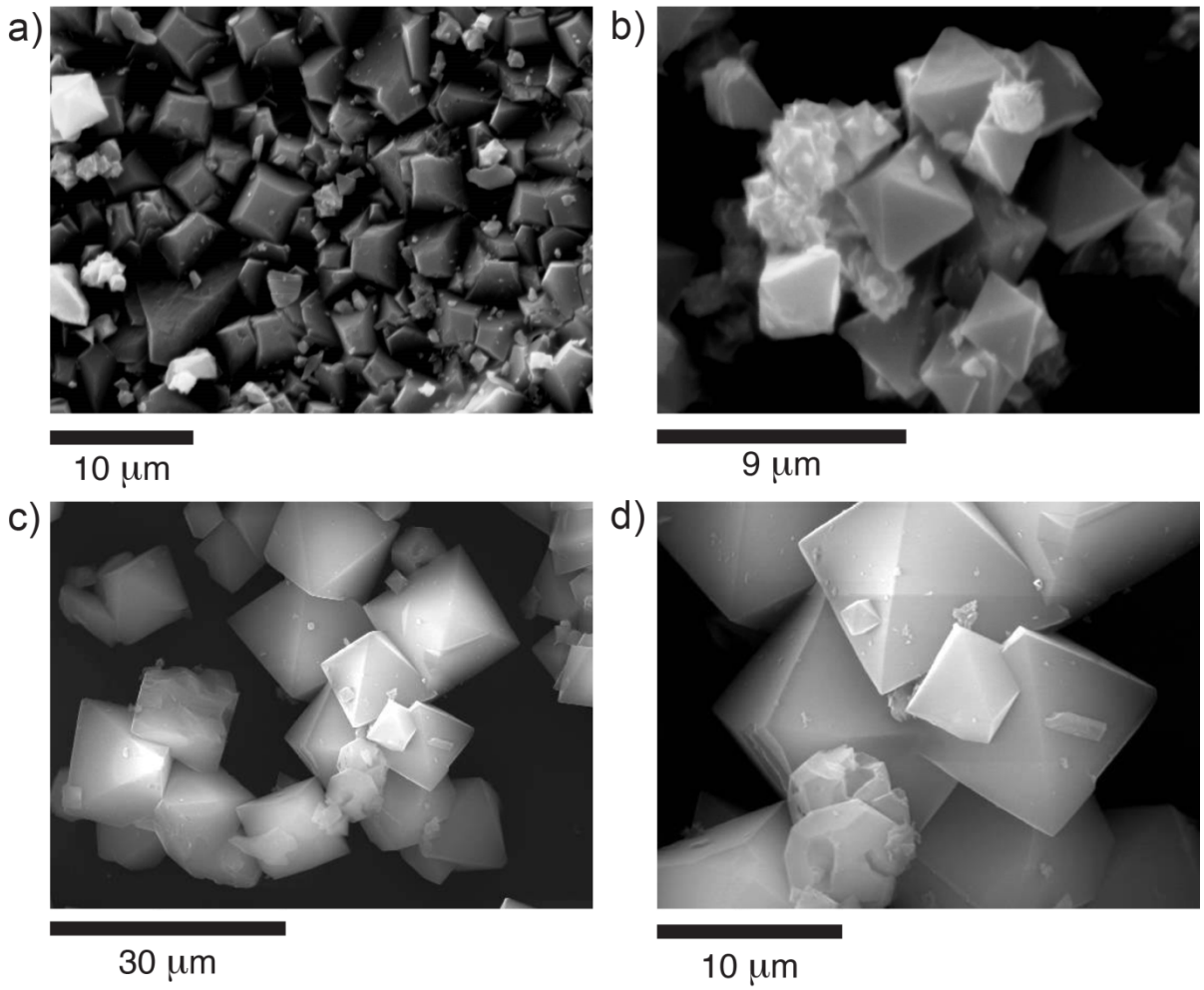

Figure S9. SEM images of MOFs synthesised in the presence five equivalents of L-proline and one equivalent of HCl. a,b) **Zr-L5**, showing crystalline sheets with occasional single crystals, and c,d) **Zr-L6**, showing discrete octahedral crystals.

Zr-L5 forms sheets of intergrown octahedral crystals around 10 μm in size (Figure S9a), but also some individual octahedra amongst the microcrystalline material (Figure S9b). In contrast, **Zr-L6** forms well-defined octahedral single crystals in the 10-20 μm range, with occasional larger crystals (Figures S9c and S9d).

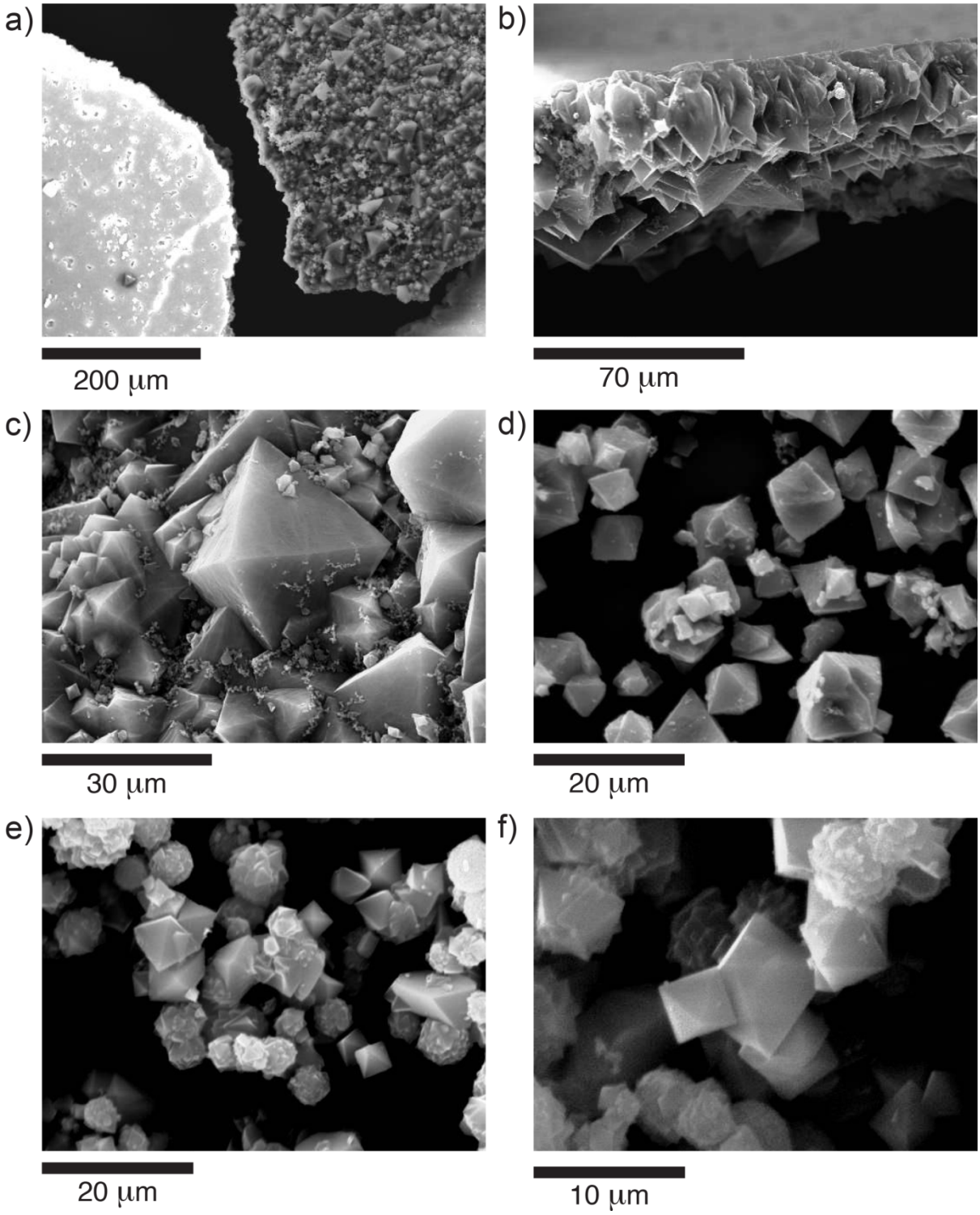

Figure S10. SEM images of MOFs synthesised in the presence five equivalents of L-proline and one equivalent of HCl. a-d) **Zr-L7**, showing crystalline sheets with occasional single crystals, and e,f) **Zr-L8**, showing a mixture of octahedral crystals and spherical microcrystalline assemblies.

Zr-L7 grows in large sheets of crystals, presumably on the edges of the reaction vessels, as both smooth and rough sides can be observed (Figures S10a and S10b). These sheets contain

some large octahedral crystals, around 30 μm, intergrown with other smaller crystals (Figure S10c), with some free octahedra of similar sizes also observed (Figure S10d). **Zr-L8** forms discrete octahedra around 5-10 μm in size, but also spherical aggregates of microcrystalline material which have similar sizes (Figures S10e and S10f). These spherical assemblies show triangular faces from the smaller octahedral crystals that comprise them.

S4. The Effect of L-Proline Modulation on Zr-L6 Particle Morphology

The effect of L-proline modulation was examined by carrying out syntheses under the same conditions as in Section S2, but with varying amounts of L-proline modulator added to the solvothermal reactions (Table S10). One equivalent of HCl is used in each synthesis as an additional modulating agent.

Table S10. Synthetic parameters for L-proline modulated syntheses of **Zr-L6**.[a]

L6		**$ZrCl_4$**		**HCl**	**L-Proline**		
Moles (mmol)	**Mass (g)**	**Moles (mmol)**	**Mass (g)**	**Volume (ml)**	**Equivalents**	**Moles (mmol)**	**Mass (g)**
0.45	0.1090	0.45	0.1049	0.04	0	0	0
0.45	0.1090	0.45	0.1049	0.04	2	0.90	0.1036
0.45	0.1090	0.45	0.1049	0.04	4	1.80	0.2072
0.45	0.1090	0.45	0.1049	0.04	6	2.70	0.3109
0.45	0.1090	0.45	0.1049	0.04	8	3.60	0.4145
0.45	0.1090	0.45	0.1049	0.04	10	4.50	0.5181

[a]Samples were washed with acetone rather than methanol after synthesis.

In addition to PXRD, which was used to confirm the crystallinity of the samples and formation of **Zr-L6** (See manuscript, Figure 3b), SEM imaging was used to monitor the effect on particle morphology of **Zr-L6** when differing amounts of L-proline were incorporated into the synthesis.

Samples were prepared for SEM imaging as described in Section S1, and images are shown overleaf in Figures S11 and S12.

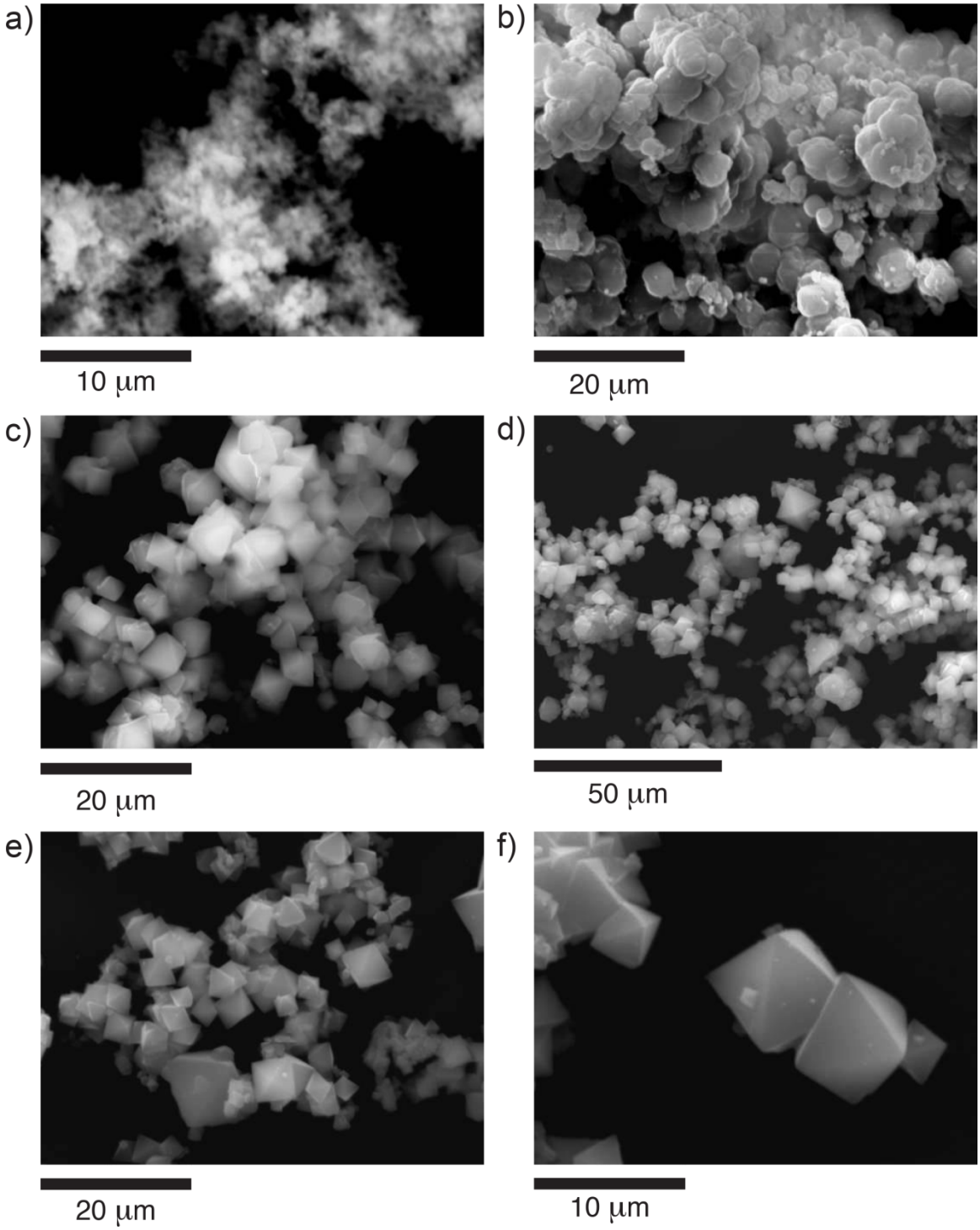

Figure S11. SEM images of the products of **Zr-L6** syntheses carried out in the presence of a) no L-proline, b) two equivalents of L-proline, c,d) four equivalents of L-proline, and e,f) six equivalents of L-proline.

When no L-proline is incorporated into the synthesis, PXRD analysis indicated that **Zr-L6** does not form, and the SEM image (Figure S11a) shows very small particles with no defined morphology. With two equivalents of L-proline in the synthesis, peaks for **Zr-L6** are seen by

PXRD, but the material (Figure S11b) shows a globular intergrown morphology with no evidence of individual crystals. Subsequent syntheses, with four (Figures S11c and 11d) and six (Figures S11e and 11f) equivalents of L-proline, generate discrete, well-defined octahedral crystals of **Zr-L6** around 5-20 μm in size. When syntheses with eight (Figures S12a and S12b) and ten (Figures S12c and S12d) equivalents of L-proline are attempted, no further increase in crystallinity or particle size occurs, indicating that four to six equivalents of L-proline is the optimal modulator concentration for both overall bulk crystallinity and individual crystal size. As such, attempts to prepare single crystals suitable for X-ray diffraction of **Zr-L6**, **Zr-L7** and **Zr-L8** were focussed on this modulator range, with other experimental parameters such as temperature and reaction time varied also (see Section S6).

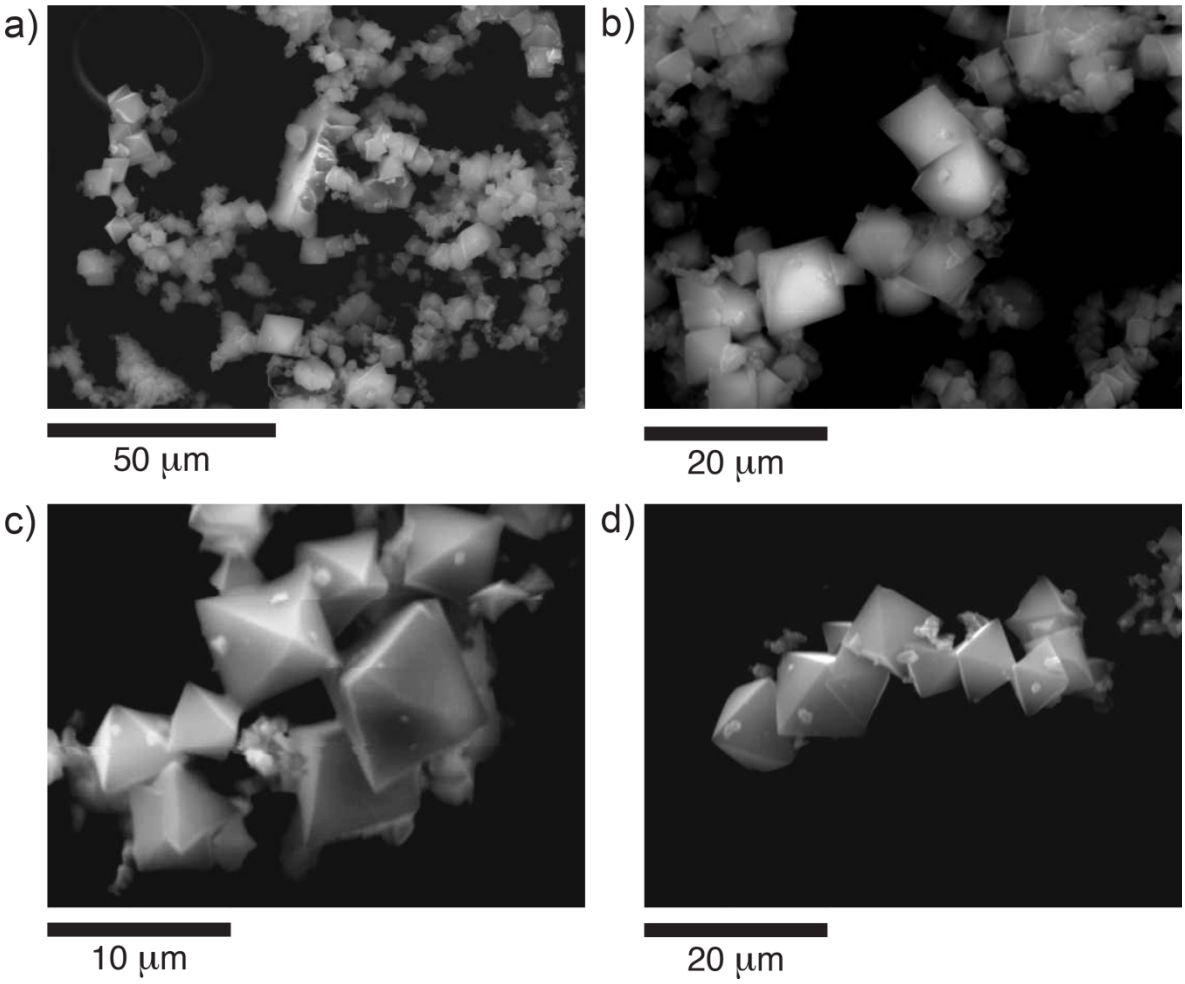

Figure S12. SEM images of the products of **Zr-L6** syntheses carried out in the presence of a,b) eight equivalents of L-proline, and c,d) ten equivalents of L-proline.

S5. Microwave Assisted Synthesis of Zr-L6

The efficacy of L-proline modulated synthesis under rapid microwave heating[S1] was investigated for **Zr-L6**. One equivalent of HCl was also used during microwave syntheses of **Zr-L6**, to enable comparisons of the materials properties with those prepared through our typical solvothermal synthetic procedure, as described in Section S2.

L-proline (0.259 g, 2.25 mmol 5 eq), **L6** (0.109 g, 0.45 mmol, 1 eq) and zirconium tetrachloride (0.105 g, 0.45 mmol, 1 eq) were added to a 35 ml microwave vial. DMF (10 ml) was added, followed by hydrochloric acid (0.04 ml) and the vial was sealed. The reaction vessel was then subject to an automated microwave programme consisting of 5 minutes of stirring at 30 °C to homogenously distribute the reagents, followed by heating at 100 °C for 1 hour without stirring. The bulk material was collected from the vial upon completion, centrifuged once with fresh DMF and two times with acetone, before being placed in a desiccator under vacuum for drying. For activation, **Zr-L6** was added to 50 ml PYREX reagent bottles and stirred in $CHCl_3$, then left to settle. The $CHCl_3$ was exchanged for fresh $CHCl_3$ a further 2 times over 48 hours, before being collected by centrifugation and placed in a desiccator under vacuum for drying. The $CHCl_3$ activated samples were used for subsequent analysis.

The analytical data collected for microwave synthesised **Zr-L6** samples (Figure S13) showed comparable particle size, morphology and porosity to samples prepared by heating for 24 hours in the oven.

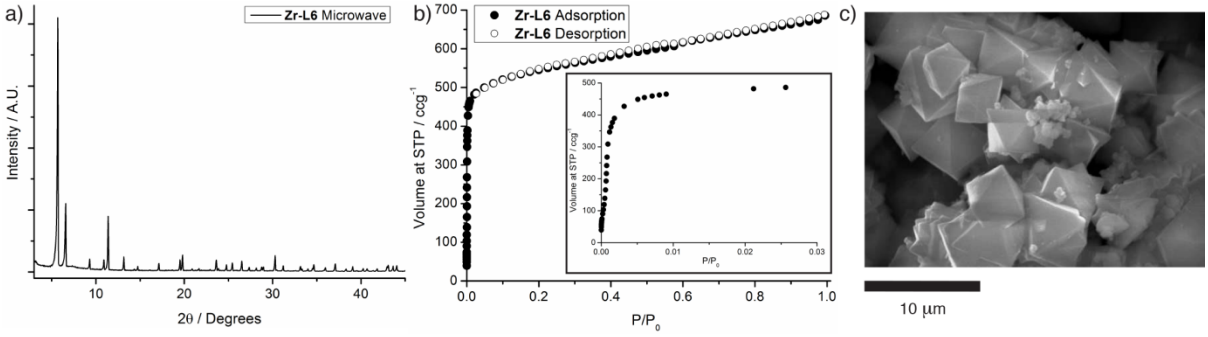

Figure S13. Characterisation of microwave synthesised **Zr-L6** by a) PXRD, b) N_2 adsorption isotherm at 77 K and c) SEM imaging show it to be comparable to solvothermally synthesised material.

The material is highly crystalline with no evidence of defects in the PXRD pattern, with SEM images showing octahedral crystals around 5-20 μm in size. The BET surface area measured from the N_2 adsorption isotherm at 77 K is 2100 m^2g^{-1}, which is slightly lower than would be expected. These results demonstrate the versatility of our L-proline modulated procedure, with much reduced modulator quantities and reaction times greatly improving the efficiency of synthesis of UiO-66 series MOFs.

S6. Crystal Structures of Zr-L6, Zr-L7 and Zr-L8

Synthetic conditions were modified in attempts to obtain single crystals of the Zr MOFs suitable for X-ray diffraction. At the time, **Zr-L5** was the only member of the isoreticular series to have been characterised by single crystal X-ray diffraction,[S2] and so attempts were made to grow crystals of **Zr-L6**, **Zr-L7** and **Zr-L8** by varying reaction times, temperatures and modulator ratios. During the course of this study, solid-state structures of **Zr-L6** have been published by a number of groups.[S3-S6] Our own crystal structures of **Zr-L6**, **Zr-L7** and **Zr-L8** have featured in preliminary communications discussing their mechanical properties.[S7, S8] Successful conditions for crystal growth are detailed below.

Zr-L6. Zirconium tetrachloride (0.210 g, 0.90 mmol, 1 eq), **L6** (0.218 g, 0.90 mmol, 1 eq) and L-proline (0.500 g, 4.50 mmol, 5 eq) were added to a 50 ml screw top Pyrex jar. 20 ml of DMF was added, followed by HCl (0.08 ml, 1 eq). The reaction mixture was sonicated for several minutes until a homogeneous white suspension remained. The white suspension was transferred to an acid digestion vessel and sealed before being placed in the oven at 120 °C for 24 hours. The reaction vessel was removed from the oven and allowed to cool to room temperature. The contents of the acid digestion vessel were removed by pipette and added to a 50 ml centrifuge tube. The reaction DMF was exchanged for fresh DMF several times. The crystals were retained in DMF before being analysed by SCXRD. Crystal structure data for **Zr-L6** is available from the CCDC, deposition number 1441659.[S7]

Zr-L7. Zirconium tetrachloride (0.052 g, 0.225 mmol, 1 eq), **L7** (0.061 g, 0.225 mmol, 1 eq) (0.060 g, 0.225 mmol, 1 eq) and L-proline (0.104 g, 0.900 mmol, 4 eq) were added to a 50 ml screw top Pyrex jar. 10 ml of DMF was added and the mixture was sonicated for 5 minutes.

HCl (0.02 ml, 1 eq) was added to the resulting suspension and the jar was placed in the sonicator for 5 minutes. The glass jar was placed in the oven at 100 °C for 48 hours, and allowed to cool to room temperature after it was removed. The reaction solvent was exchanged for fresh DMF several times. The crystals were retained in DMF before being analysed by SCXRD. Crystal structure data for **Zr-L7** is available from the CCDC, deposition number 1441660.[S7]

Zr-L8. Zirconium tetrachloride (0.052 g, 0.225 mmol, 1 eq), **L8** (0.060 g, 0.225 mmol, 1 eq) and L-proline (0.104 g, 0.900 mmol, 4 eq) were added to a 50 ml screw top Pyrex jar. 10 ml of DMF was added and the mixture was sonicated for 5 minutes. HCl (0.02 ml, 1 eq) was added to the resulting suspension and the jar was placed in the sonicator for 5 minutes. The glass jar was placed in the oven at 100 °C for 48 hours, and allowed to cool to room temperature after it was removed. The reaction DMF was exchanged for fresh DMF several times. The crystals were retained in DMF before being analysed by SCXRD. Crystal structure data for **Zr-L8** is available from the CCDC, deposition number 1418959.[S8]

S7. Molecular Dynamics Calculations

Molecular dynamics calculations were utilised to elucidate the disorder in the structures of **Zr-L7** and **Zr-L8**. We have previously used these calculations to examine the structures of **Zr-L6** and **Zr-L7** in a preliminary communication discussing their mechanical properties.[S7]

Computational methods. All *ab initio* (Born-Oppenheimer) MD calculations were performed using the Quickstep module of the CP2K (version 2.6) simulation package.[S9] The BLYP[S10, S11] exchange-correlation functional with semi-empirical dispersion corrections to the energies and gradients from the DFT-D3[S12] method (cut-off radius 10 Å) were used throughout. Energies and forces were calculated utilizing the Gaussian plane-wave scheme, which is a dual basis set method wherein a linear combination of Gaussian-type orbitals is used to describe the Kohn-Sham molecular orbitals, while the electron density is described by an auxiliary plane-wave basis set (expressed at an energy cut-off of 350 Ry, accompanied by the relative cutoff of 50 Ry for the Gaussian basis set collocation). The double-zeta quality MOLOPT basis set[S13-S16] was used for all elements, in conjunction with the relativistic, norm-

conserving Goedecker-Teter-Hutter pseudopotentials, optimized for use against the BLYP functional. During each SCF cycle, the electronic structure was explicitly minimized to a tolerance of 10^{-7} Hartree. The equations of motion were integrated using a time step of 0.55 fs.

Results obtained for **Zr-L6** and **Zr-L7** have been reported [S7] in a preliminary communication; herein the work is extended to include **Zr-L8**. As significantly different crystallographic unit cell parameters had been obtained experimentally for **Zr-L7** (a = 29.3248(8) Å) and **Zr-L8** (a = 29.8884(3) Å) a natural question to raise was whether this lattice expansion was simply due to substituting atom X (as defined in Scheme 1 in the main text) from nitrogen (in the case of **L7**), to carbon (in the case of **L8**). To this end, the modeling work for **Zr-L8** took as its starting point the crystal structure of **Zr-L7**, with atom identities manually edited. The unit cell was then recast to its primitive cell settings, thereby reducing the volume of the crystallographic unit cells to a quarter of its conventional setting, which represented a considerable reduction in computational resource required. The resulting unit cell was still relatively large, however (a = ~20 Å, $\alpha = \beta = \gamma$ = ~60 °), which by definition results in a compact 1st Brillouin zone. Thus the constraint that the QUICKSTEP module employs Γ-point sampling only of the Brillouin zone was not a concern in this work.

Equilibration of the model was initiated under the isobaric-isothermal ensemble regime (NPT; constant number of particles, pressure and temperature) for 6 ps. The temperature was set to 300 K and controlled by a chain of Nosé-Hoover thermostats[S17] coupled to every degree of freedom (the so-called massive thermostat) with a frequency of 4000 cm^{-1}, which is high enough to properly sample the fast vibrational motion of the C-H bond in the linker. The barostat was set up with a coupling time constant of 300 fs and an external pressure of 1 bar. In addition, a reference unit cell of constant volume was defined alongside the MOF model to fix the number of grid points used to compute the Coulomb and exchange-correlation energies. This was used to mitigate any effects of varying grid points due to potential volume fluctuations of the simulation box. It has been shown previously that the use of such a reference cell avoids any discontinuities in the potential energy profile when the volume is permitted to vary.[S18-S20] The resulting unit cell volume was observed to expand over a time period of 3 ps by ca. 7 %, where after no further change was observed over a further 3 ps (see Figure S14, overleaf).

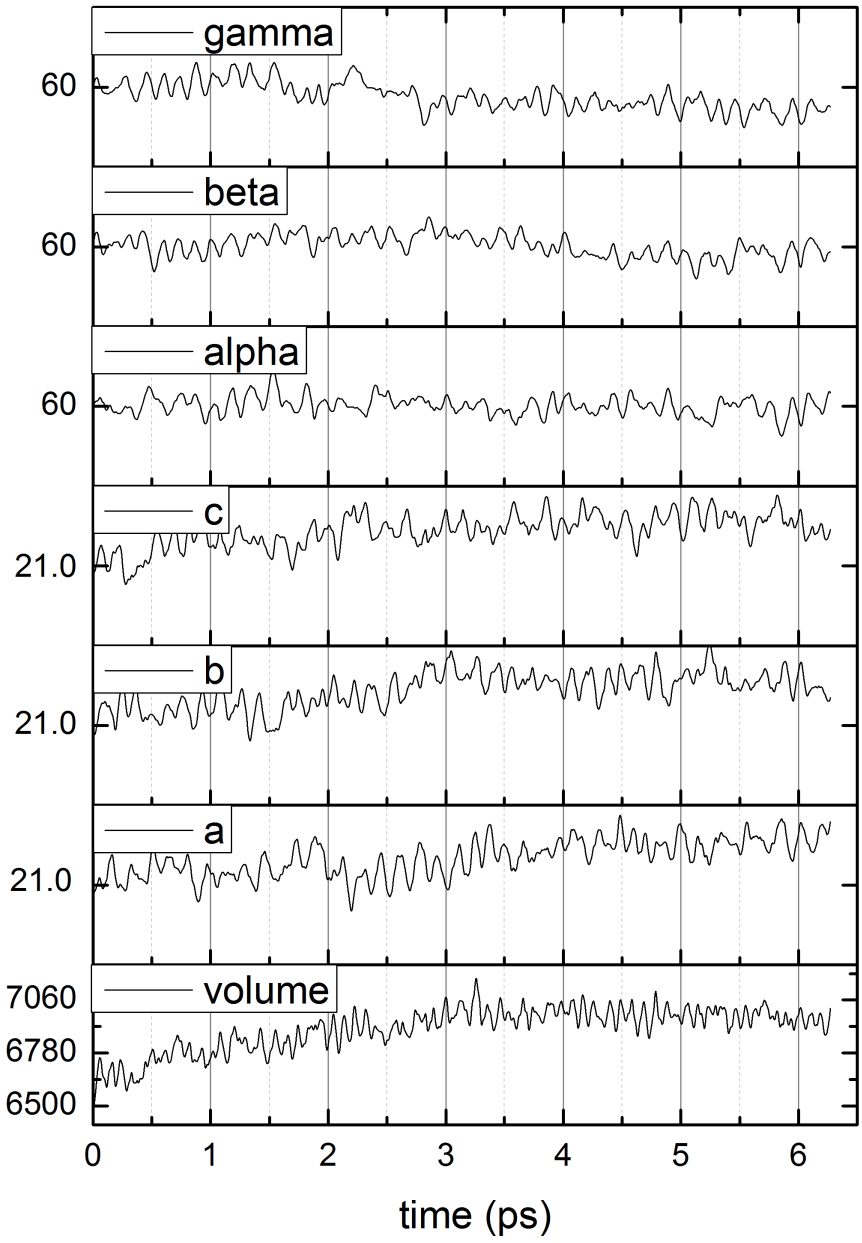

Figure S14. Evolution of unit cell parameters (a, b, c reported in Å, volume in Å^3 and alpha, beta, gamma in °) for MOF system **Zr-L8** in NPT MD simulation. Starting structure taken from **Zr-L7** crystallographic unit cell, following manual edit of ligand X atoms (N swapped for C).

The equilibrated unit cell parameters for **Zr-L8** corresponded to a = 21.3(2), b =21.4(2), c = 21.4(2) Å, α = 60.0(6), β = 60.9(7) and γ = 59.4(9) °, demonstrating that in the absence of symmetry constraints the crystal system remained unchanged over the course of the dynamics run. This primitive unit cell setting corresponds to a conventional unit cell with a = 30.2(3) Å, which closely matches the experimental unit cell parameters obtained for **Zr-L8** (a =

29.8884(3) Å). Moreover, the experimental unit cell expansion (Δa = 0.6 Å) closely matches the simulated unit cell expansion ($\Delta \mathbf{a}$ = 0.4(3) Å), thus confirming that the expansion in the cubic unit cell lattice vector is entirely due to identity of atom X in the linker.

The unit cell parameters were then fixed at $a = b = c$ = 21.3 Å, $\alpha = \beta = \gamma = 60°$, and the ensemble switched to NVT for production run dynamics (3 ps). The resulting trajectory was then analysed numerically to determine the time-averaged mean atomic positions (simply, the positions of all atoms, averaged over all time frames) and to calculate the atomic probability density functions (via numerical calculation of the variances and co-variances of each atom, using methods described previously).[S21-S23]

The former allows an overlay image against the experimental structure to be obtained (Figures S15a and S15b); the latter are analogous to the thermal ellipsoid model used in crystallographic refinements, and are displayed in Figure S15c at the standard 50% probability level. The output data were processed graphically using Mercury CSD 3.5.1.[S24]

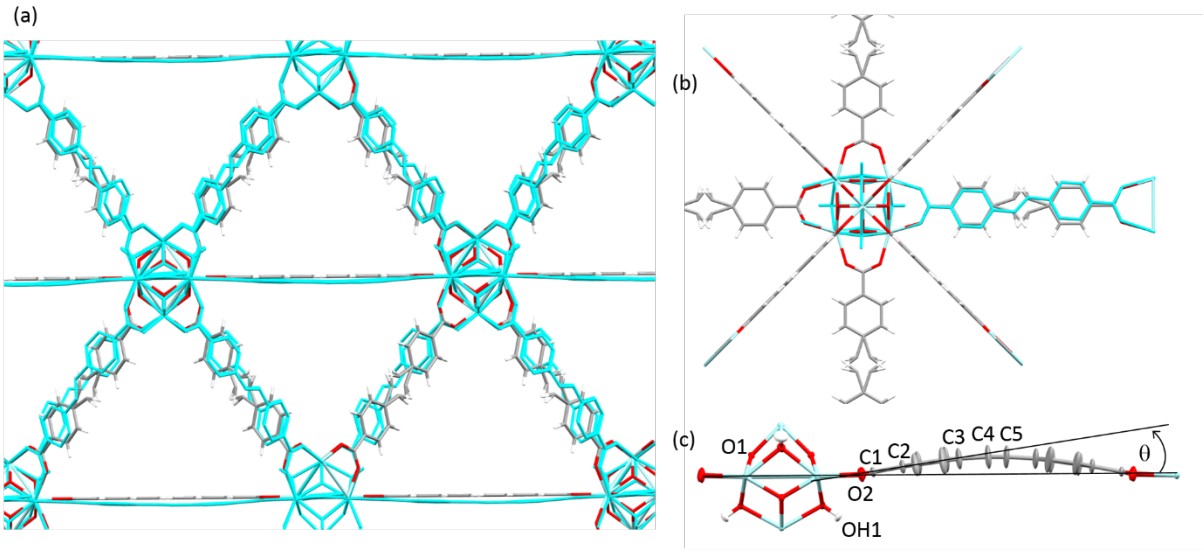

Figure S15. Mean atomic positions model for **Zr-L8** (in cyan) superimposed on the crystallographically disordered structure; a) a packing structure viewed along the [110] axis, and b) an enlarged view of one frustrated ligand. c) Calculated atomic pair distribution functions drawn at the standard 50% level, emphasizing atomic motion in linker. θ is defined as the intersection angle between the planes drawn through the equatorial Zr atoms and the C atoms of the aromatic ring in the linker. C – grey, O – red, Zr –light blue, H – white, omitted for clarity in the ligand only.

The molecular dynamics simulation demonstrated that the geometrically frustrated stilbene linker in **Zr-L8** is accommodated by bowing out of the horizontal mirror plane by an angle θ (defined in Figure S15c) that was observed to vary from 1 to 10 ° (plotted for all six independent linkers (due to the absence of symmetry constraints) in Figure S16).

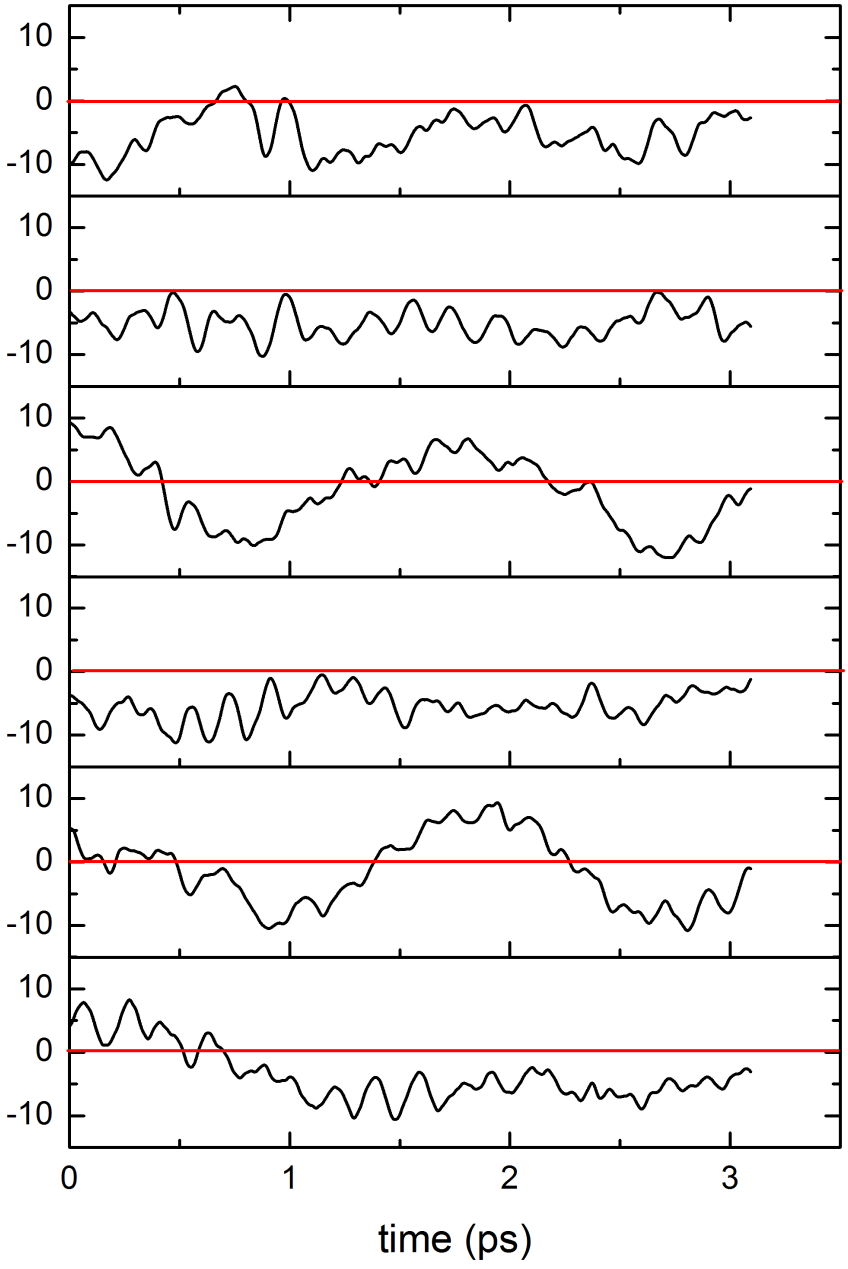

Figure S16. Plot showing the variation in ligand bow angle θ (defined in Figure S14c) against time for the six ligands in **Zr-L8**.

From this plot it is readily apparent that around half of the ligands appear to flex above and below the horizontal mirror plane (marked by the θ = 0° horizontal line). The absence of such

behavior for the remaining ligands is more than likely a sampling issue: if the dynamical trajectory were run for a longer time this behavior would be expected to be observed for all ligands in **Zr-L8**. The mean average value for θ observed for **Zr-L8** was 5(3)°, compared to 5(3)° for **Zr-L7** and 3(2)° for **Zr-L6**, as reported in our earlier publication,[S7] indicating that ligand flexing in **Zr-L8** appears to occur to a similar degree as observed for the N-substituted **L7**.

The time averaged MD parameters reported in Table S11 are very similar to those reported earlier for **Zr-L6** and **Zr-L7**,[S7] and good agreement is also observed for those parameters that can be confidently described in the crystallographic model. The cage Zr•••Zr and Zr-O2 simulated distances agree (to within 0.07 Å) with those reported for the structurally related UiO-66 (**Zr-L1**) by EXAFs and X-ray powder diffraction.[S25] As with **Zr-L6** and **Zr-L7** (and UiO-66) *r*Zr•••O(1) lengthens by *ca.* 0.2 Å if the μ^3-O(1) atoms are capped with hydrogen. While this finding could not be confirmed by the best-fit space group assigned from the crystallographic study (*Fm-3m*) in this work, it is substantiated by a recent structural report of **Zr-L6**[5] and by modelling work on UiO-66 by Valenzano *et al.*, whose equivalent Zr-O(1)H and Zr-O(1) distances agree with ours to within 0.02 Å.[S25]

Table S11. Selected parameters from the experimentally derived crystal structure of **Zr-L8** compared with the time-averaged structures derived from MD simulation.

Parameters[a] (*r*/Å, ∠/°)	**Zr-L8 expt**	**Zr-L8 time averaged MD[b]**
Av. *r*Zr•••Zr	3.482	3.579(6)
Av. *r*Zr•••O1 (cluster)	2.112	Zr•••O1 = 2.096(4) Zr•••OH1 = 2.302(6)
Av. *r*Zr-O2 (ligand)	2.221	2.26(6)
Av. *r*O-C1	1.248	1.276(5)
Av. *r*C1-C2	1.501	1.472(1)
Av. rC_{arom}-C_{arom}	1.391	1.371(13)
Av. *r*C3-C4	1.473	1.454(2)
Av. *r*C4=C5	1.326	1.307(20)
∠α[a]	0	7(3)

[a]See Figure S15c for atom labelling. [b]Parameters obtained from averaging atomic coordinates (*P*1 model) over production run (NVT) trajectory.

Finally, from the atomic PDFs derived from the MD trajectory (Figure S15c), and consistent with thermal expansion studies of other MOFs,[S26] it is readily apparent that the most dynamical components of the system are the light-weight linker units, with the heavier $Zr_6O_4(OH)_4$ cluster exhibiting much smaller thermal motion. As the dynamics trajectory was harvested for a small representative sampling of the MOF structure (the model is based on just the primitive setting of the unit cell, over a time span of only 3 ps) we do not expect to capture much of the low energy lattice mode behavior which is known to be centrally important in establishing quantitatively correct atomic PDFs.[S21-S23] However the current analysis is adequate to demonstrate which components of the structure undergo the most significant thermal motion.

With the single crystal structures of **Zr-L7** and **Zr-L8** in hand, and the disorder model proven valid by the molecular dynamics simulations, PXRD patterns for the two MOFs were predicted using Mercury CSD 3.5.1[S24] and compared with the experimental patterns collected from the bulk syntheses described in Section S2 (Figure S17).

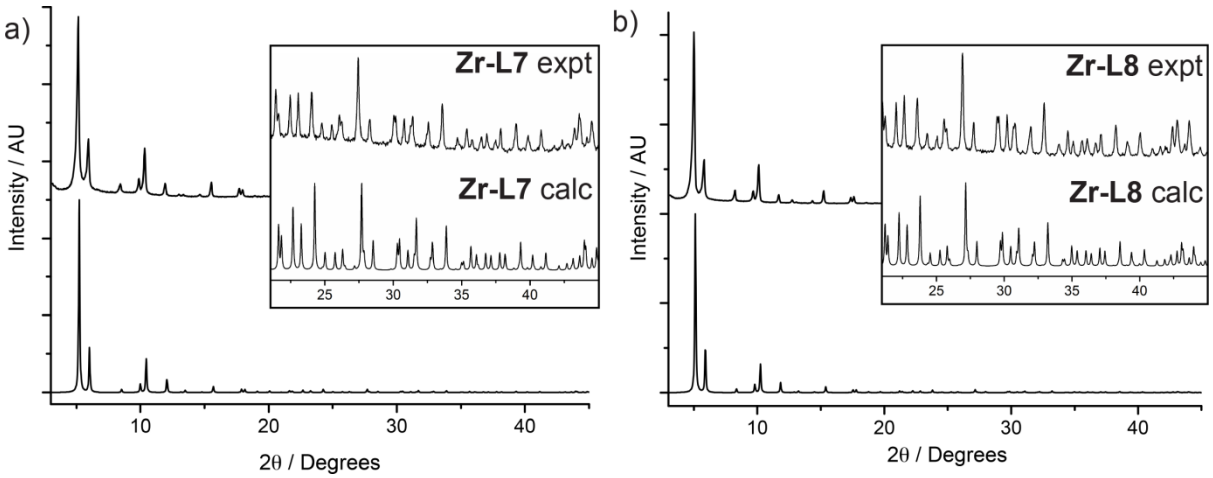

Figure S17. Stacked PXRD patterns of a) **Zr-L7** and b) **Zr-L8**, showing very close correlation between the predicted patterns derived from single crystal structures and the patterns recorded experimentally from bulk MOF samples.

The predicted and experimental patterns closely match in both cases, confirming the phase purity of the MOFs and the representative nature of the single crystal structures.

S8. Amino Acid Modulation of Hf MOFs

Initially, the effect of HCl addition to the synthesis of **Hf-L6** was examined by carrying out solvothermal syntheses containing varying quantities of HCl. This process was inspired by the study of UiO-67 (**Zr-L6**) synthesis in the presence of HCl carried out by Farha *et al.*[S27]

Hafnium tetrachloride (0.144 g, 0.45 mmol, 1 eq) was added to a 50 ml screw top Pyrex jar, followed by 10 ml of DMF. The desired amount of HCl was added and the jar was placed in the sonicator for 5 minutes. **L6** (0.109 g, 0.45 mmol, 1 eq) was added and the resulting suspension was sonicated for 5 minutes. The glass jar was placed in the oven at 120 °C for a period of 24 hours before being removed and allowed to cool to room temperature. The mixture was centrifuged, and the product was washed with fresh DMF (30 ml) and MeOH (2 x 30 ml). The product was kept under vacuum for a minimum of 24 hours where it remained until it was analysed by PXRD (Figure S18).

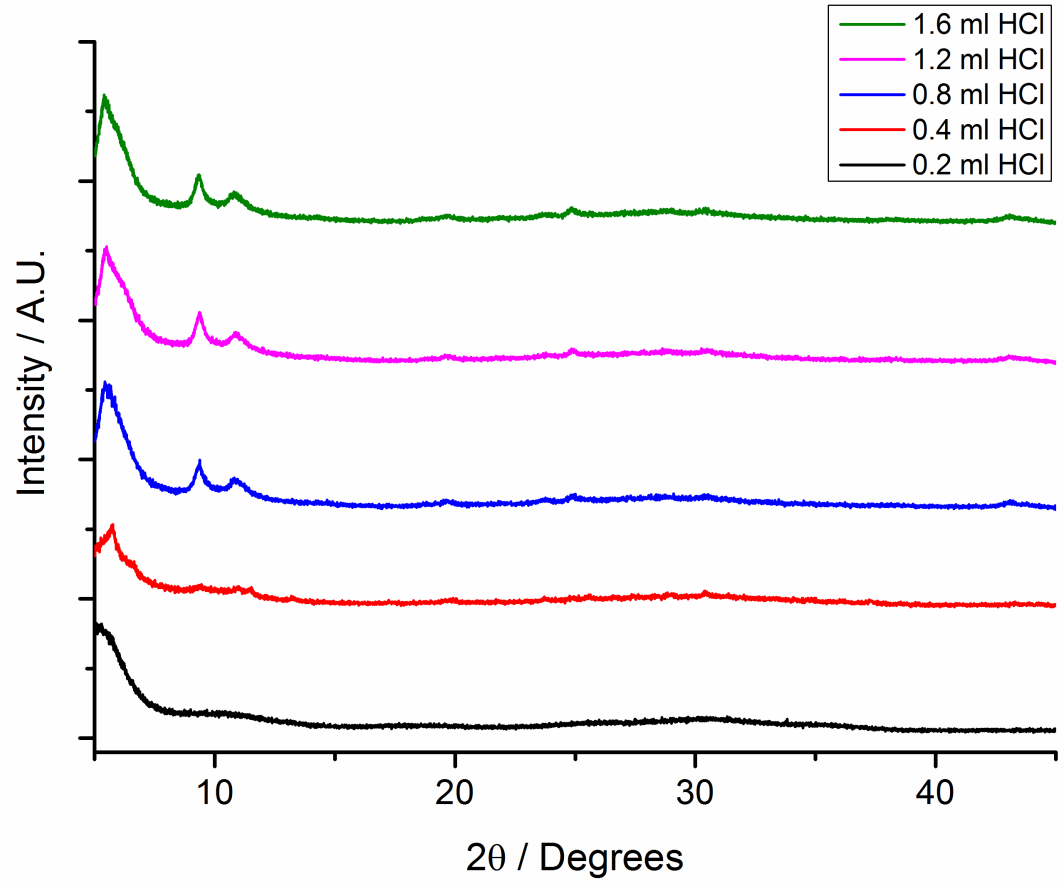

Figure S18. Stacked PXRD patterns of the products of attempted **Hf-L6** synthesis in the presence of varying amounts of HCl, as denoted by the key.

None of the isolated solids showed any peaks related to **Hf-L6** or indeed any crystalline solids, and so it is clear that while HCl can promote the synthesis of **Zr-L6**, it does not for the analogous **Hf-L6**. Subsequently, the syntheses to assess the efficacy of amino acids as modulators followed the same general procedure as for the Zr MOFs, but substituting $HfCl_4$ for $ZrCl_4$. It was decided not to attempt to modulate the syntheses of the Hf MOFs with L-arginine, as it did not enhance any syntheses of the analogous Zr MOFs and yielded sticky tars rather than crystalline solids.

The amino acid (2.25 mmol, 5 eq) was added directly to a 50 ml Pyrex screw top jar followed by addition of $HfCl_4$ (0.144 g, 0.45 mmol, 1 eq) as a 5 ml DMF solution containing HCl (0.04 ml). The resulting mixture was sonicated for 5 minutes. The ligand (0.45 mmol, 1eq) was subsequently added to the reaction flask as a DMF solution (5 ml). The reaction mixture was subject to sonication for a further 5 minutes to aid solvation of the reactants. The glass jar was placed in the oven at 120 °C for a period of 24 hours before being removed and allowed to cool to room temperature. The products were added to centrifuge tubes and centrifuged for 20 minutes. The reaction DMF was decanted from the centrifuge tube and the product was subject to centrifugation a further three times, once with fresh DMF (30 ml) and twice with methanol (2 x 30 ml). **Hf-L8** was washed with acetone rather than MeOH. The centrifuge tube was then placed in the desiccator under vacuum for a minimum of 24 hours where it remained until it was analysed by PXRD.

Tables S12-S19 detail the exact masses of reagents used, while Figures S19-S26 show stacked PXRD patterns if the resulting material, allowing us to assess extent of modulation in each case.

Table S12. Amino acid modulated synthesis of **Hf-L1**.

L1		$HfCl_4$		HCl	Modulator		
Moles (mmol)	**Mass (g)**	**Moles (mmol)**	**Mass (g)**	**Volume (ml)**	**Amino Acid**	**Moles (mmol)**	**Mass (g)**
0.45	0.0748	0.45	0.1441	0.04	unmodulated		
0.45	0.0748	0.45	0.1441	0.04	L-proline	2.25	0.2590
0.45	0.0748	0.45	0.1441	0.04	4-amino benzoic acid	2.25	0.3086
0.45	0.0748	0.45	0.1441	0.04	beta alanine	2.25	0.2005
0.45	0.0748	0.45	0.1441	0.04	L-leucine	2.25	0.2952
0.45	0.0748	0.45	0.1441	0.04	L-tryptophan	2.25	0.4595
0.45	0.0748	0.45	0.1441	0.04	L-arginine	2.25	0.3920
0.45	0.0748	0.45	0.1441	0.04	DL-threonine	2.25	0.2680

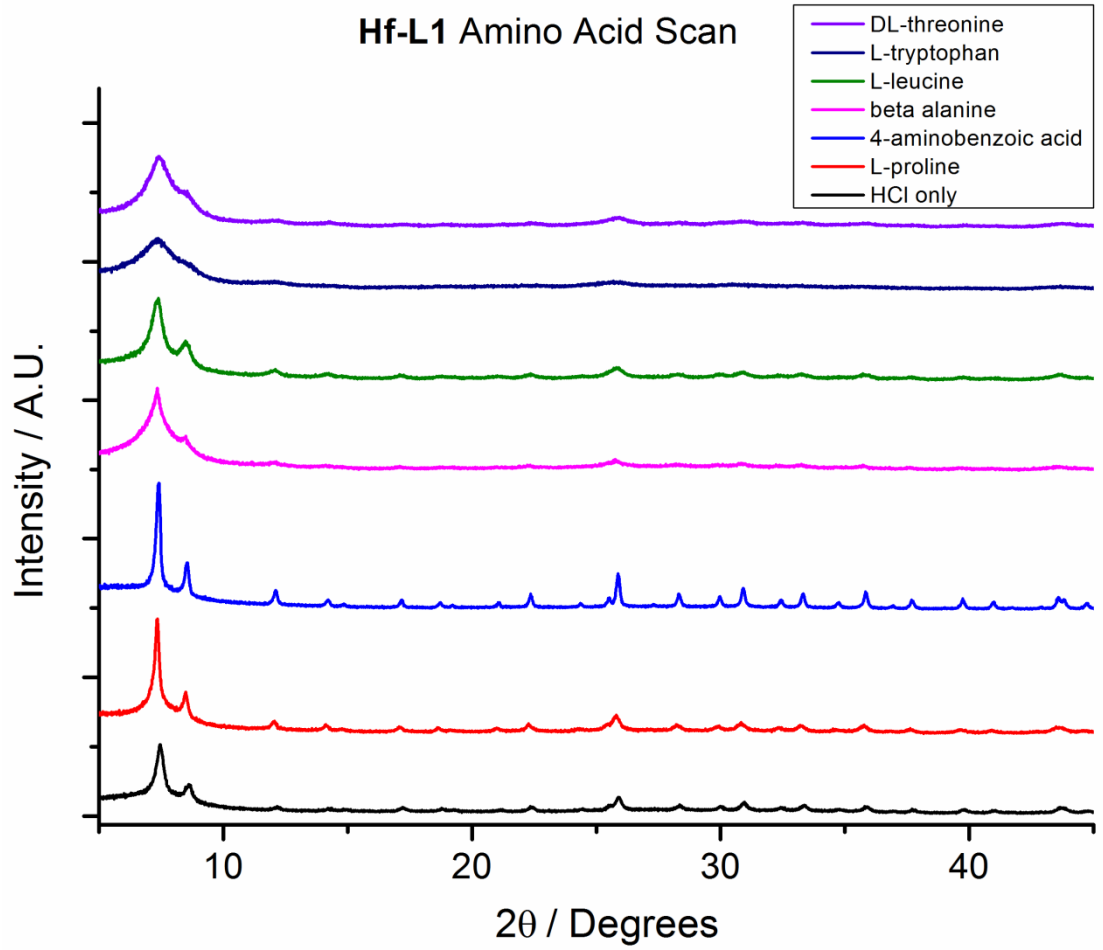

Figure S19. Stacked PXRD patterns for amino acid modulated syntheses of **Hf-L1**.

Table S13. Amino acid modulated synthesis of **Hf-L2**.

L2		$HfCl_4$		HCl	Modulator		
Moles (mmol)	**Mass (g)**	**Moles (mmol)**	**Mass (g)**	**Volume (ml)**	**Amino Acid**	**Moles (mmol)**	**Mass (g)**
0.45	0.1103	0.45	0.1441	0.04	unmodulated		
0.45	0.1103	0.45	0.1441	0.04	L-proline	2.25	0.2590
0.45	0.1103	0.45	0.1441	0.04	4-amino benzoic acid	2.25	0.3086
0.45	0.1103	0.45	0.1441	0.04	beta alanine	2.25	0.2005
0.45	0.1103	0.45	0.1441	0.04	L-leucine	2.25	0.2952
0.45	0.1103	0.45	0.1441	0.04	L-tryptophan	2.25	0.4595
0.45	0.1103	0.45	0.1441	0.04	L-arginine	2.25	0.3920
0.45	0.1103	0.45	0.1441	0.04	DL-threonine	2.25	0.2680

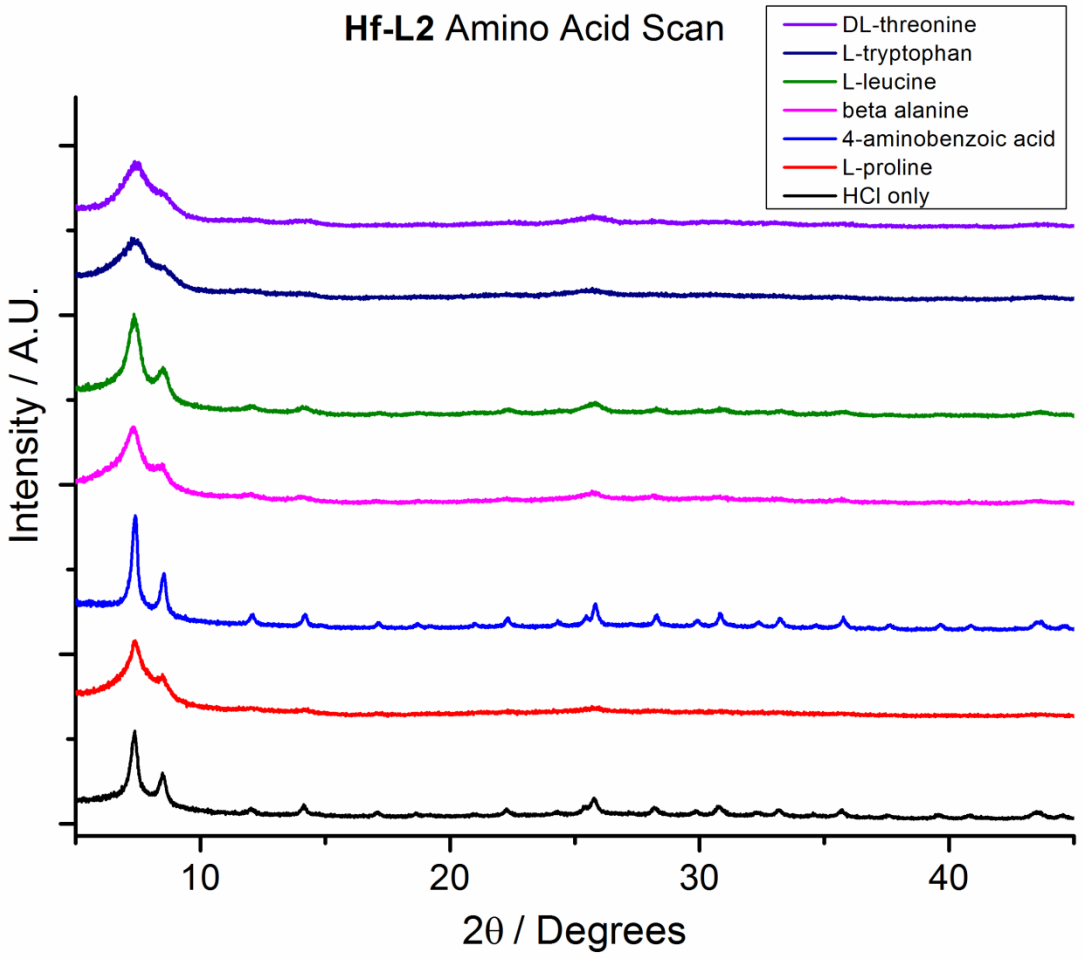

Figure S20. Stacked PXRD patterns for amino acid modulated syntheses of **Hf-L2**.

Table S14. Amino acid modulated synthesis of **Hf-L3**.

L3		$HfCl_4$		HCl	Modulator		
Moles (mmol)	**Mass (g)**	**Moles (mmol)**	**Mass (g)**	**Volume (ml)**	**Amino Acid**	**Moles (mmol)**	**Mass (g)**
0.45	0.0950	0.45	0.1441	0.04	unmodulated		
0.45	0.0950	0.45	0.1441	0.04	L-proline	2.25	0.2590
0.45	0.0950	0.45	0.1441	0.04	4-amino benzoic acid	2.25	0.3086
0.45	0.0950	0.45	0.1441	0.04	beta alanine	2.25	0.2005
0.45	0.0950	0.45	0.1441	0.04	L-leucine	2.25	0.2952
0.45	0.0950	0.45	0.1441	0.04	L-tryptophan	2.25	0.4595
0.45	0.0950	0.45	0.1441	0.04	L-arginine	2.25	0.3920
0.45	0.0950	0.45	0.1441	0.04	DL-threonine	2.25	0.2680

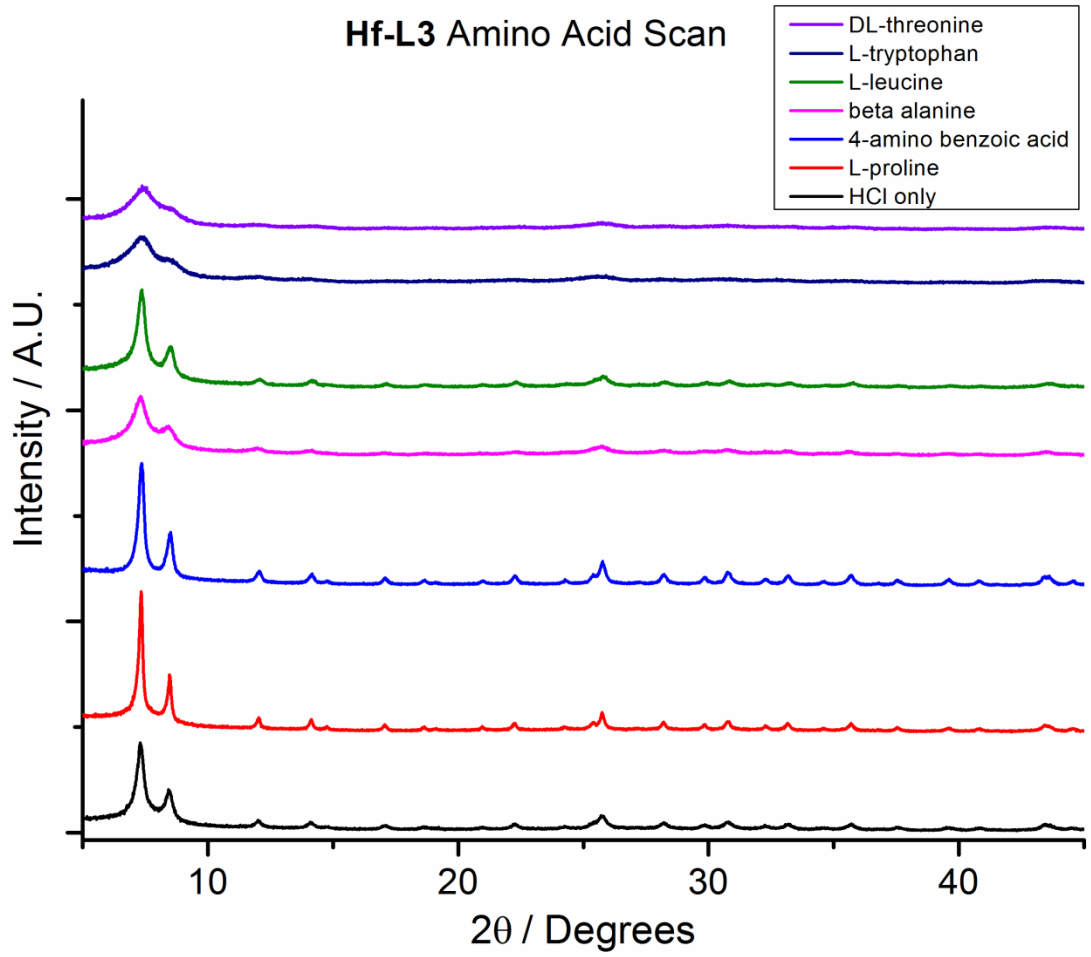

Figure S21. Stacked PXRD patterns for amino acid modulated syntheses of **Hf-L3**.

Table S15. Amino acid modulated synthesis of **Hf-L4**.

L4		$HfCl_4$		HCl	Modulator		
Moles (mmol)	**Mass (g)**	**Moles (mmol)**	**Mass (g)**	**Volume (ml)**	**Amino Acid**	**Moles (mmol)**	**Mass (g)**
0.45	0.0815	0.45	0.1441	0.04	unmodulated		
0.45	0.0815	0.45	0.1441	0.04	L-proline	2.25	0.2590
0.45	0.0815	0.45	0.1441	0.04	4-amino benzoic acid	2.25	0.3086
0.45	0.0815	0.45	0.1441	0.04	beta alanine	2.25	0.2005
0.45	0.0815	0.45	0.1441	0.04	L-leucine	2.25	0.2952
0.45	0.0815	0.45	0.1441	0.04	L-tryptophan	2.25	0.4595
0.45	0.0815	0.45	0.1441	0.04	L-arginine	2.25	0.3920
0.45	0.0815	0.45	0.1441	0.04	DL-threonine	2.25	0.2680

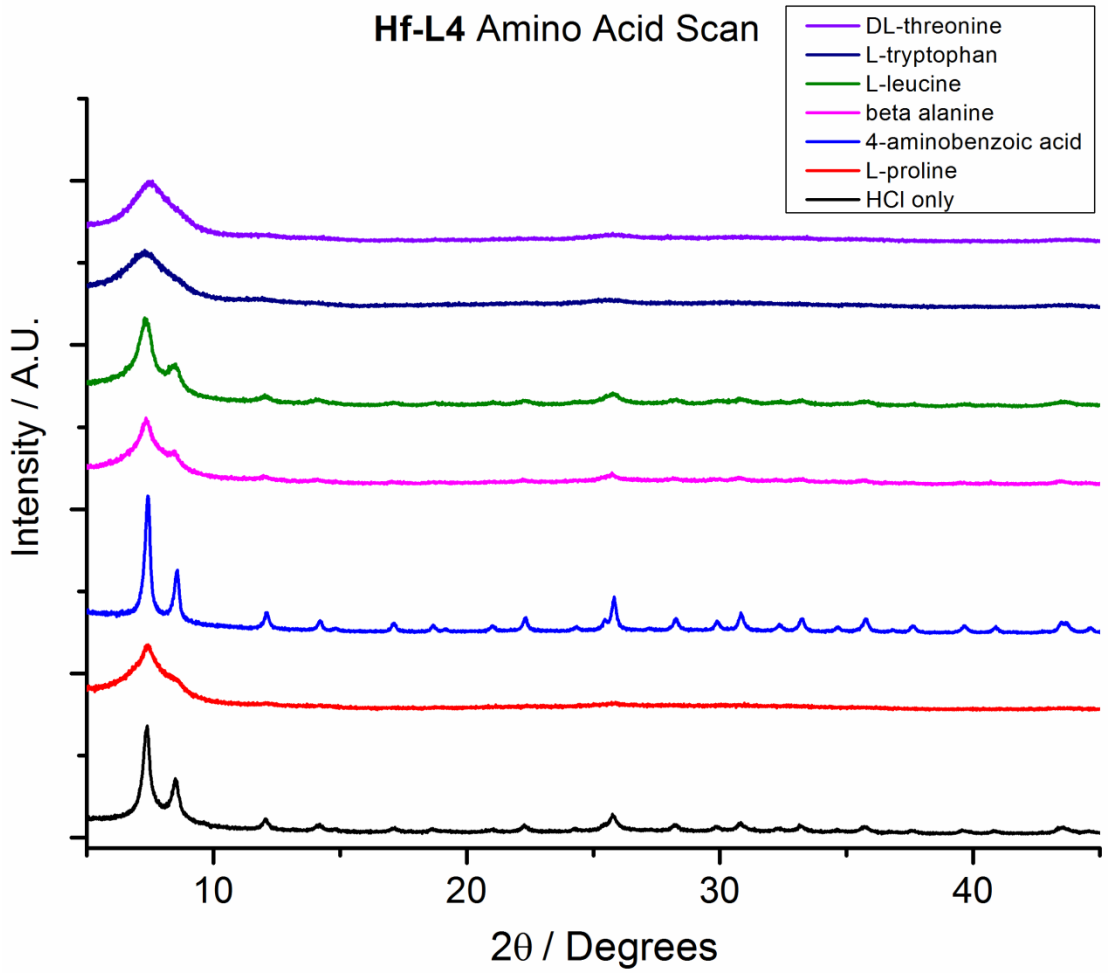

Figure S22. Stacked PXRD patterns for amino acid modulated syntheses of **Hf-L4**.

Table S16. Amino acid modulated synthesis of **Hf-L5**.

L5		$HfCl_4$		HCl	Modulator		
Moles (mmol)	**Mass (g)**	**Moles (mmol)**	**Mass (g)**	**Volume (ml)**	**Amino Acid**	**Moles (mmol)**	**Mass (g)**
0.45	0.0973	0.45	0.1441	0.04	unmodulated		
0.45	0.0973	0.45	0.1441	0.04	L-proline	2.25	0.2590
0.45	0.0973	0.45	0.1441	0.04	4-amino benzoic acid	2.25	0.3086
0.45	0.0973	0.45	0.1441	0.04	beta alanine	2.25	0.2005
0.45	0.0973	0.45	0.1441	0.04	L-leucine	2.25	0.2952
0.45	0.0973	0.45	0.1441	0.04	L-tryptophan	2.25	0.4595
0.45	0.0973	0.45	0.1441	0.04	L-arginine	2.25	0.3920
0.45	0.0973	0.45	0.1441	0.04	DL-threonine	2.25	0.2680

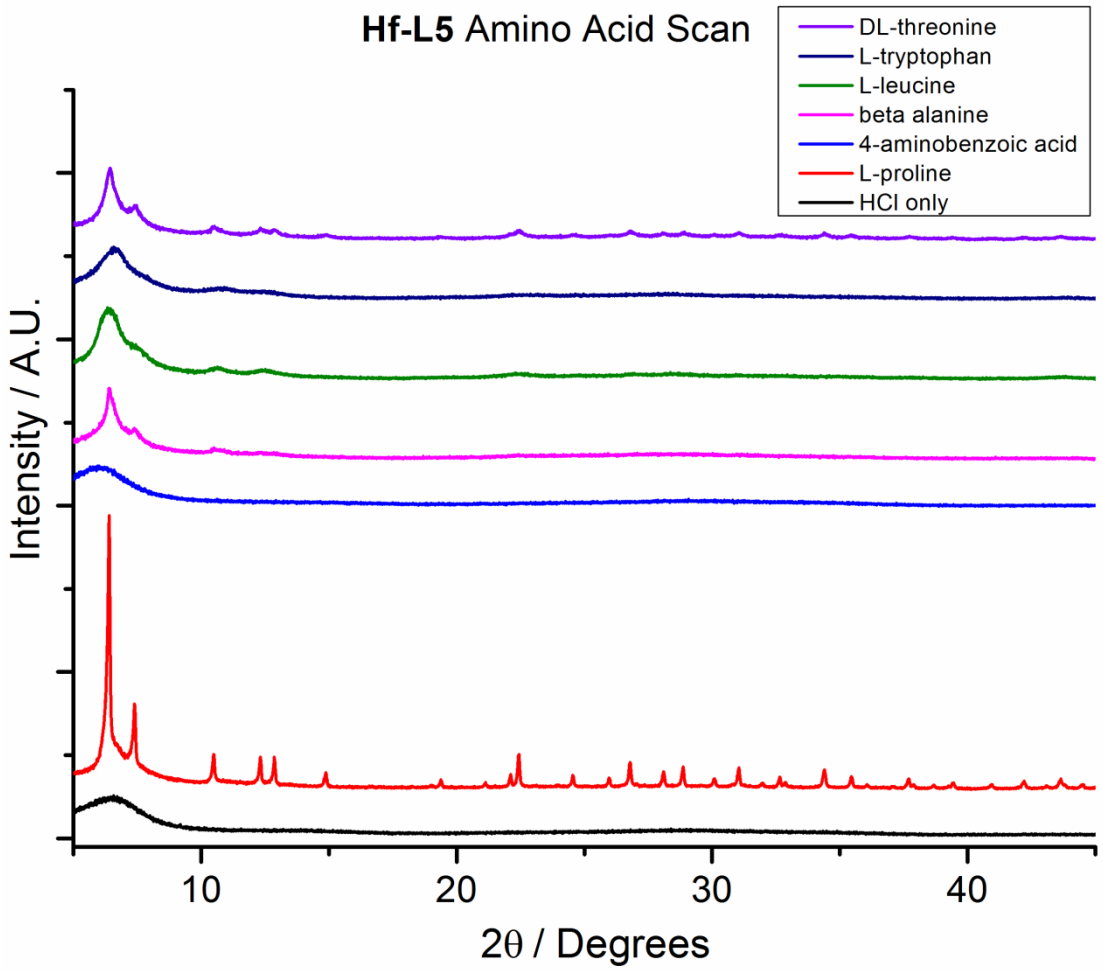

Figure S23. Stacked PXRD patterns for amino acid modulated syntheses of **Hf-L5**.

Table S17. Amino acid modulated synthesis of **Hf-L6**.

L6		$HfCl_4$		HCl	Modulator		
Moles (mmol)	**Mass (g)**	**Moles (mmol)**	**Mass (g)**	**Volume (ml)**	**Amino Acid**	**Moles (mmol)**	**Mass (g)**
0.45	0.1090	0.45	0.1441	0.04	unmodulated		
0.45	0.1090	0.45	0.1441	0.04	L-proline	2.25	0.2590
0.45	0.1090	0.45	0.1441	0.04	4-amino benzoic acid	2.25	0.3086
0.45	0.1090	0.45	0.1441	0.04	beta alanine	2.25	0.2005
0.45	0.1090	0.45	0.1441	0.04	L-leucine	2.25	0.2952
0.45	0.1090	0.45	0.1441	0.04	L-tryptophan	2.25	0.4595
0.45	0.1090	0.45	0.1441	0.04	L-arginine	2.25	0.3920
0.45	0.1090	0.45	0.1441	0.04	DL-threonine	2.25	0.2680

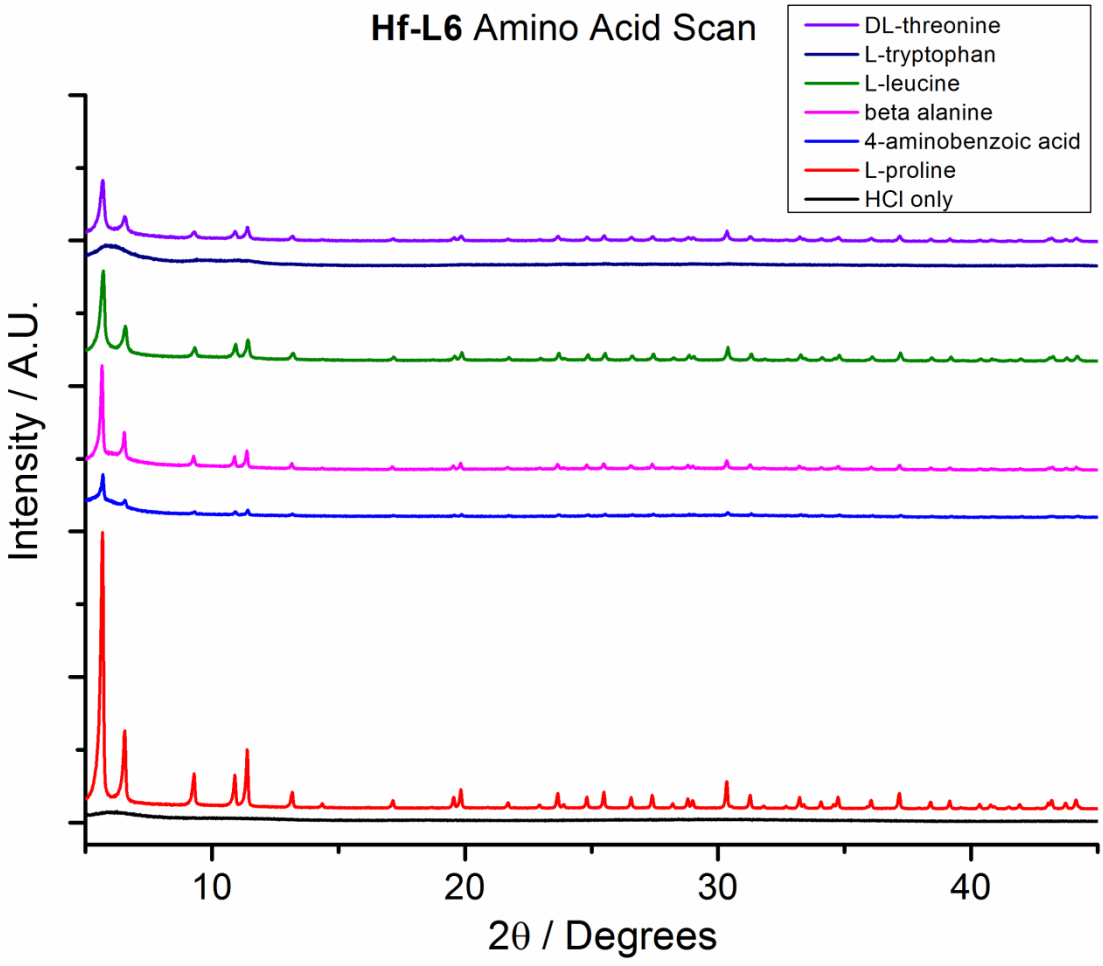

Figure S24. Stacked PXRD patterns for amino acid modulated syntheses of **Hf-L6**.

Table S18. Amino acid modulated synthesis of **Hf-L7**.

L7		$HfCl_4$		HCl	Modulator		
Moles (mmol)	**Mass (g)**	**Moles (mmol)**	**Mass (g)**	**Volume (ml)**	**Amino Acid**	**Moles (mmol)**	**Mass (g)**
0.45	0.1216	0.45	0.1441	0.04	unmodulated		
0.45	0.1216	0.45	0.1441	0.04	L-proline	2.25	0.2590
0.45	0.1216	0.45	0.1441	0.04	4-amino benzoic acid	2.25	0.3086
0.45	0.1216	0.45	0.1441	0.04	beta alanine	2.25	0.2005
0.45	0.1216	0.45	0.1441	0.04	L-leucine	2.25	0.2952
0.45	0.1216	0.45	0.1441	0.04	L-tryptophan	2.25	0.4595
0.45	0.1216	0.45	0.1441	0.04	L-arginine	2.25	0.3920
0.45	0.1216	0.45	0.1441	0.04	DL-threonine	2.25	0.2680

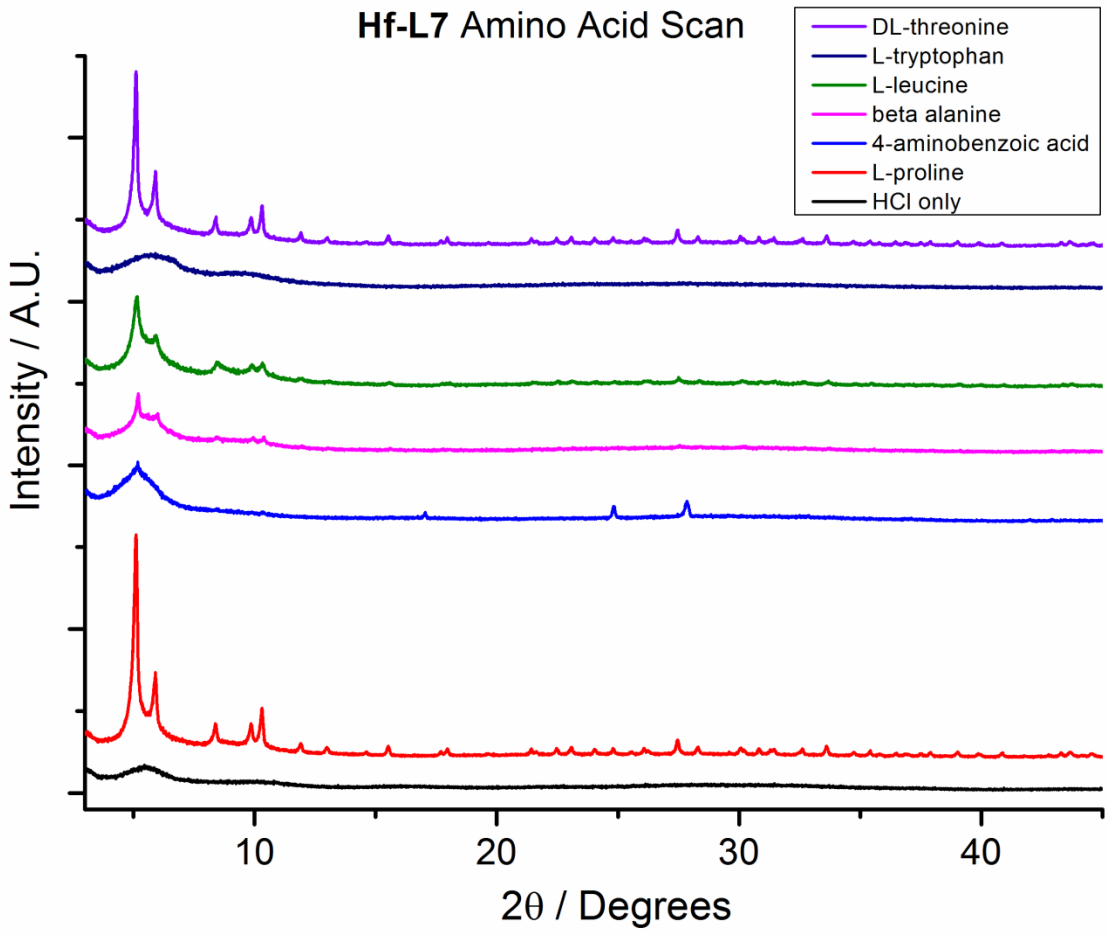

Figure S25. Stacked PXRD patterns for amino acid modulated syntheses of **Hf-L7**.

Table S19. Amino acid modulated synthesis of **Hf-L8**.

L8		$HfCl_4$		HCl	Modulator		
Moles (mmol)	**Mass (g)**	**Moles (mmol)**	**Mass (g)**	**Volume (ml)**	**Amino Acid**	**Moles (mmol)**	**Mass (g)**
0.45	0.1207	0.45	0.1441	0.04	unmodulated		
0.45	0.1207	0.45	0.1441	0.04	L-proline	2.25	0.2590
0.45	0.1207	0.45	0.1441	0.04	4-amino benzoic acid	2.25	0.3086
0.45	0.1207	0.45	0.1441	0.04	beta alanine	2.25	0.2005
0.45	0.1207	0.45	0.1441	0.04	L-leucine	2.25	0.2952
0.45	0.1207	0.45	0.1441	0.04	L-tryptophan	2.25	0.4595
0.45	0.1207	0.45	0.1441	0.04	L-arginine	2.25	0.3920
0.45	0.1207	0.45	0.1441	0.04	DL-threonine	2.25	0.2680

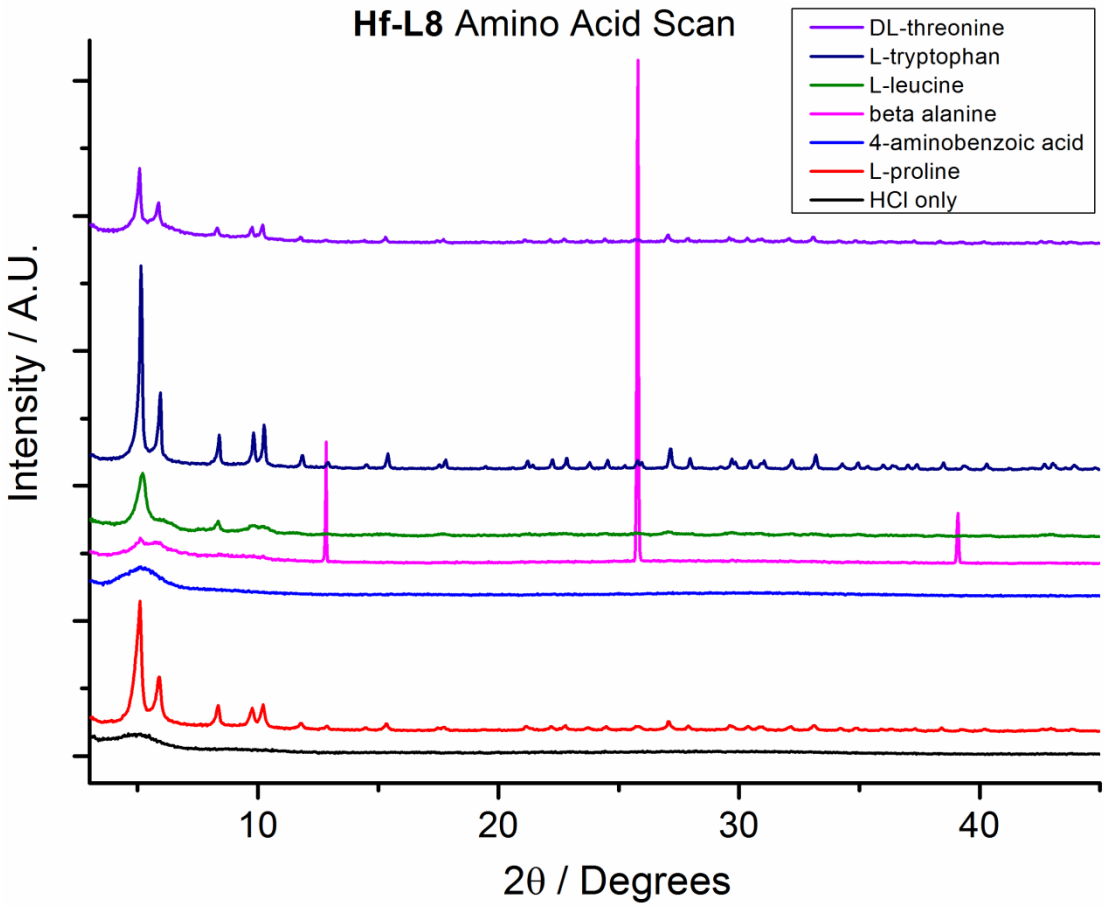

Figure S26. Stacked PXRD patterns for amino acid modulated syntheses of **Hf-L8**.

The results are summarised in Table S20.

Table S20. Summary of amino acid modulation of Hf MOFs.

	Modulator					
	L-proline	4-amino benzoic acid	beta alanine	L-leucine	L-trytophan	DL-threonine
L1	**+**	**+**	—	—	—	—
L2	—	**+**	—	—	—	—
L3	**+**	**+**	—	•	—	—
L4	—	**+**	—	—	—	—
L5	**+**	•	**+**	•	•	**+**
L6	**+**	**+**	**+**	**+**	•	**+**
L7	**+**	•	**+**	**+**	•	**+**
L8	**+**	•	•	**+**	**+**	**+**

Key: + represents enhanced crystallinity, — represents a decline in crystallinity, and • represents very little effect on crystallinity compared with the unmodulated sample.

As with the analogous Zr MOFs, the syntheses of the Hf terephthalates showed little benefit to including amino acid modulators, although 4-aminobenzoic acid seemed to tentatively improve the crystallinity of the Hf MOFs of **L1-L4**. The Hf MOFs of the longer linkers, **L5-L8**, are again successfully modulated by smaller hydrophobic amino acids, with L-proline being the standout modulator. Interestingly, the small hydrophilic amino acid DL-threonine successfully modulates all these MOFs, while L-tryptophan shows a slightly more pronounced enhancement of crystallinity for **Hf-L8** compared to L-proline.

It did not prove possible to prepare single crystals of **Hf-L8** using either L-proline or L-tryptophan as modulators. SEM imaging (samples prepared as described in Section S3) of **Hf-L8** prepared by L-proline modulation showed that the MOF forms spherical microcrystalline assemblies approximately 5 μm in diameter (Figure S27). This behaviour is analogous to that of **Zr-L8**, although in the Hf case no individual single crystals are evident.

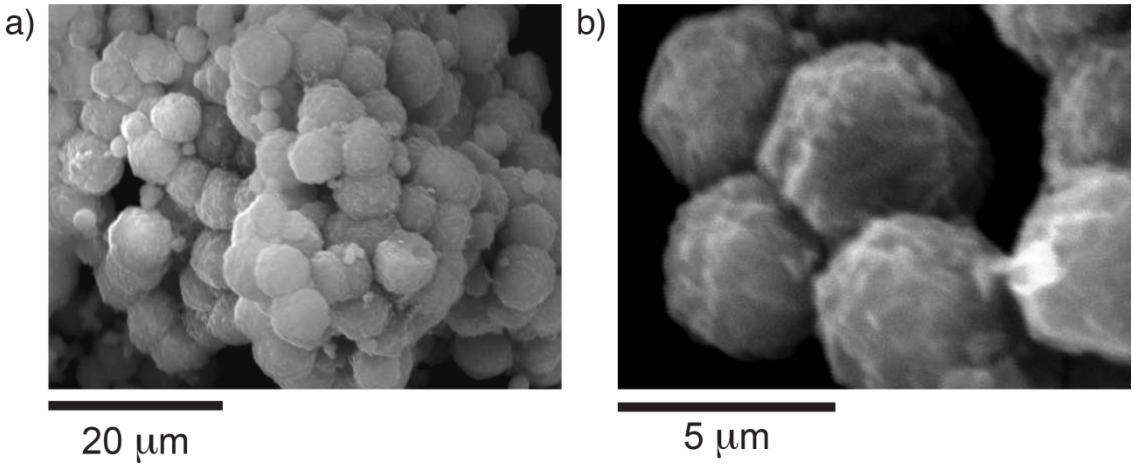

Figure S27. SEM images at different magnifications of **Hf-L8** prepared by L-proline modulation, which forms spherical microcrystalline aggregates around 5 μm in size.

S9. Crystal Structures of Hf-L6 and Hf-L7

As with the zirconium MOFs, attempts were made to synthesise the Hf MOFs as single crystals suitable for X-ray diffraction by varying reaction parameters.

Hf-L6. Hafnium tetrachloride (0.144 g, 0.45 mmol, 1 eq) and L-proline (0.259 g, 2.25 mmol, 5 eq) were added to a 50 ml screw top Pyrex jar. 10 ml of DMF was added and the jar was placed in the sonicator for 5 minutes. **L6** (0.109 g, 0.45 mmol, 1 eq) and HCl (0.04 ml) were added to the resulting suspension and the jar was placed in the sonicator for 5 minutes. The glass jar was placed in the oven at 120 °C for 24 hours. The glass jar was removed from the oven and allowed to cool to room temperature. The reaction DMF was exchanged for fresh DMF several times. The crystals were retained in DMF before being analysed by SCXRD.

Crystal Data for Hf-L6. $Hf_6O_4(OH)_4(C_{14}H_{10}O_4)_6$. (215 DMF), M_r = 2644.26, Cubic, a = 26.762(3) Å, V = 19167(6) Å^3, T = 120 K, space group Fm-3m (no. 225), Z = 4, 44943 reflections measured, 1059 unique (R_{int} = 0.083), which were used in all calculations. The final R_1 = 0.0373 for 1013 observed data [$F^2 > 2\sigma(F^2)$] and $wR_2(F^2)$ = 0.1001 (all data). Crystal structure data for **Hf-L6** is available from the CCDC, deposition number 1442842.

Single crystal X-ray diffraction data were collected and processed using an Agilent Technologies SuperNova diffractometer using CuKα radiation. The structure was refined from the **Zr-L6** analogue (CCDC deposition 1441659) against F^2 using all data using CRYSTALS.[S28] Using the SQUEEZE algorithm within PLATON,[S29] the pore volume and electron density within the voids were calculated and found to be 11923 Å^3 and contain 6115 electrons per unit cell (the equivalent of ~153 molecules of DMF) respectively. During refinement of the data, all non-hydrogen atoms were refined anisotropically, with thermal similarity and vibrational restraints applied to all non-hydrogen atoms except the Hf atom. 1,2 and 1,3 distances on the ligand were restrained, while a planarity restraint was applied to the phenyl ring. Hydrogen atoms attached to C-atoms and the hydroxyl O-atom were placed geometrically and not refined. The phenyl ring is disordered over two positions (shown in Figure S28), where the ring is 50% occupied 16 ° above or below the mirror plane which runs through the structure.

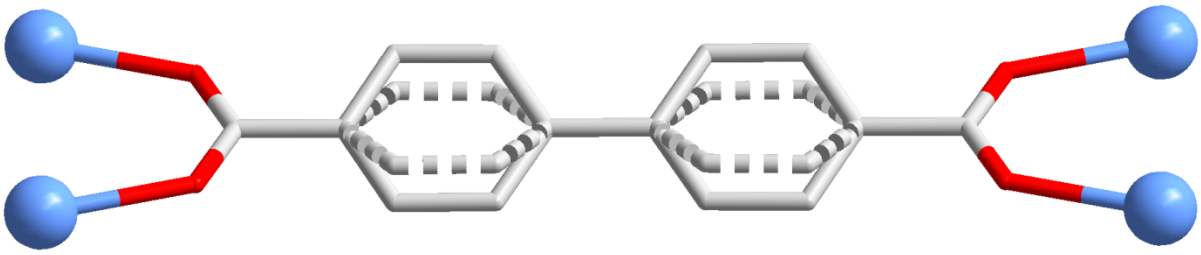

Figure S28. Representation of the **Hf-L6** crystal structure showing the two possible orientations (in filled and dashed lines) that the phenyl ring can adopt in a 1:1 disordered ratio about the mirror plane. Hydrogen atoms are omitted for clarity.

Hf-L7. Hafnium tetrachloride (0.144 g, 0.45 mmol, 1 eq) and L-proline (0.155 g, 1.35 mmol, 3 eq) were added to a 50 ml screw top Pyrex jar. 10 ml of DMF was added and the jar was placed in the sonicator for 5 minutes. **L7** (0.122 g, 0.45 mmol, 1 eq) and HCl (0.04 ml) were added to the resulting suspension and the jar was placed in the sonicator for 5 minutes. The glass jar was placed in the oven at 120 °C for 24 hours. The glass jar was removed from the oven and allowed to cool to room temperature. The reaction DMF was exchanged for fresh DMF several times. The crystals were retained in DMF before being analysed by SCXRD.

Crystal Data for Hf-L7. $Hf_6O_4(OH)_4(C_{14}H_8N_2O_4)_6$, M_r = 2896.38, Cubic, a = 29.3248(8) Å, V = 25218(2) Å^3, T = 150 K, space group Fm-3m (no. 225), Z = 4, 10347 reflections

measured, 954 unique (R_{int} = 0.073), which were used in all calculations. The final R_1 = 0.0739 for 750 observed data [$F^2 > 2\sigma(F^2)$] and $wR_2(F^2)$ = 0.1634 (all data). Crystal structure data for **Hf-L6** is available from the CCDC, deposition number 1442841.

Single crystal X-ray diffraction data were collected on a Bruker APEX II diffractometer. Integration was performed using the program Saint, while the adsorption correction was carried out using SADABS. The structure was refined from the **Zr-L7** analogue (CCDC deposition 1441660) against F^2 using all data using CRYSTALS.[S28] Using the SQUEEZE algorithm within PLATON,[S29] the pore volume and electron density within the voids were calculated and found to be 17151 Å^3 and contain 4188 electrons per unit cell (the equivalent of ~105 molecules of DMF) respectively. During refinement of the data, Hf(1) and O(1) were refined anisotropically; all other non-hydrogen atoms were refined isotropically, with thermal similarity and vibrational restraints applied to all non-hydrogen atoms except Hf. 1,2 and 1,3 distances on the ligand were restrained, while a planarity restraint was applied to the phenyl ring. Hydrogen atoms attached to C-atoms and the hydroxyl O-atom were placed geometrically and not refined. The benzene ring is disordered over 3 positions in the ligand; the ring which sits in the plane of the ligand is occupied 50% of the time and the other two positions above and below the plane occupied 25% each. (Figure S29).

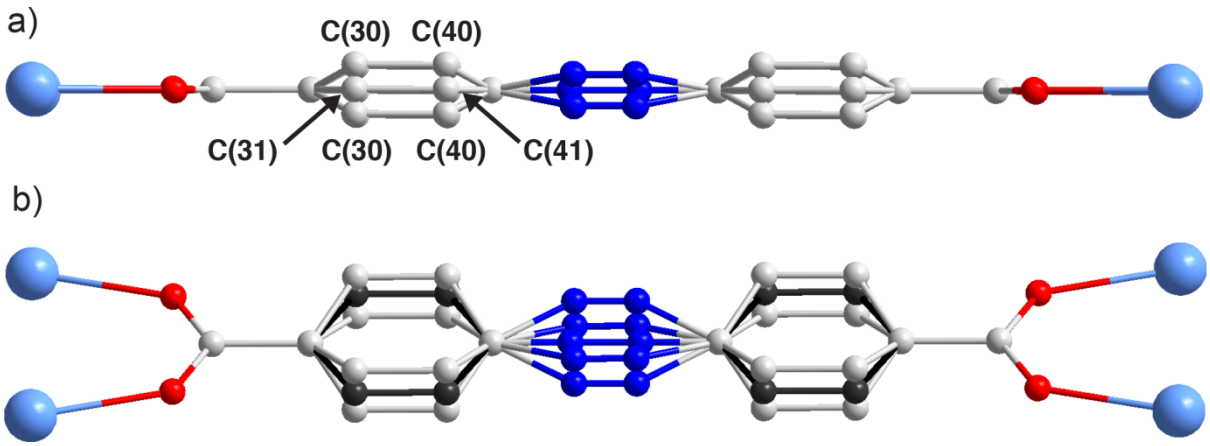

Figure S29. Representations of the **Hf-L7** crystal structure showing the three possible orientations the phenyl ring can adopt about the mirror plane. a) C(31) and C(41) are 50 % occupied and the two positions of C(30) and C(40) are both 25% occupied. b) The phenyl ring defined by C(31) and C(41) is coloured black for guidance.

Site-occupied disorder for N(1) results in 4 possible positions for the N=N bond linking across the two phenyl groups (Shown in Figure S30). The oxygen site O(1) is disordered

(50:50 hydroxide:oxide), though this could not be resolved. A 50% occupied H-atom was added to O1 in order to address the charge balance, this disorder has been seen in previous UiO structures.[S4]

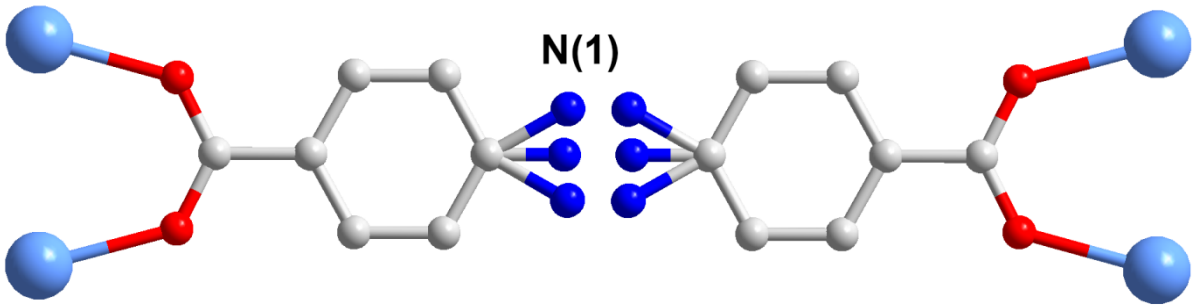

Figure S30. Representation of the **Hf-L7** crystal structure showing the four possible orientations for the azo N=N bond which is disordered over an inversion centre, and bisected by two fold axes and two mirror planes.

With the crystal structures of **Hf-L6** and **Hf-L7** in hand, it was possible to predict the powder X-ray diffraction patterns of the MOFs using Mercury CSD 3.5.1,[S24] which show close agreement with the experimental patterns for **Hf-L6** and **Hf-L7** (Figure S31), as well as their zirconium analogues, confirming their phase purity and the structural similarities of the Zr and Hf analogues.

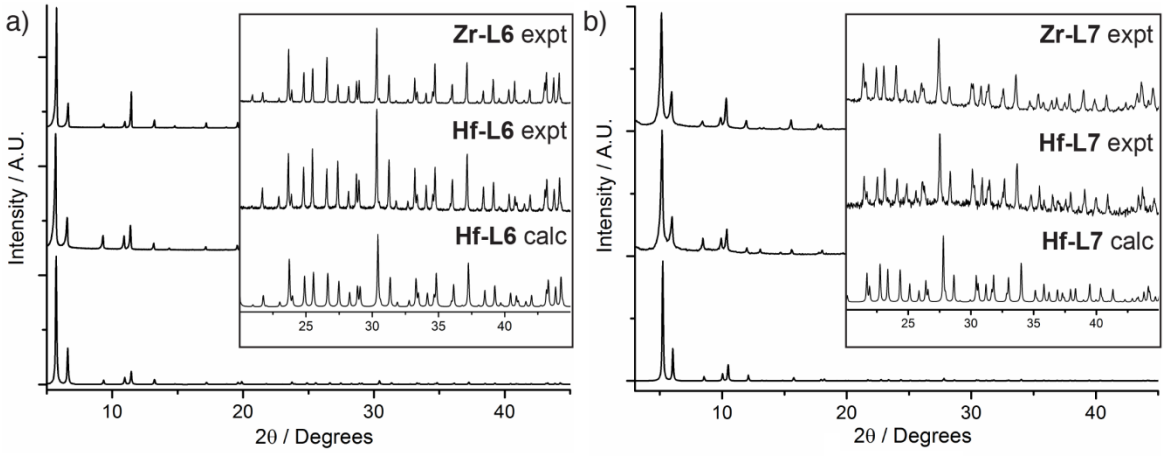

Figure S31. Stacked PXRD patterns of a) **Hf-L6** and b) **Hf-L7**, showing very close correlation between the predicted patterns derived from single crystal structures and the patterns recorded experimentally from bulk MOF samples, as well as their Zr analogues.

S10. Modulator Incorporation

Following initial synthetic investigations, Zr and Hf MOFs of **L5-L8** were synthesised in bulk quantities using the general synthetic procedure outlined above, with five equivalents of L-proline used in all cases due to its superior modulating properties and to allow direct comparison between the different MOF samples. The bulk Zr (washed with DMF and methanol) and Hf (washed with DMF and acetone) MOFs were then subject to activation conditions. For activation, the MOFs were placed in 50 ml reagent bottles and immersed in 25 ml THF, dispersed by stirring and placed in the oven at 50 °C. The THF was replenished and the process repeated consecutively over four days. After this period the THF was removed and the MOFs were placed in the desiccator under vacuum for drying. The THF activated samples were used for the remainder of the analysis.

The incorporation of modulators into the final MOF structure is a known phenomenon which can have adverse effect on material properties,[S5, S30] but also potentially introduce new reactivity and stability at defect sites.[S31, S32] The incorporation of modulators was assessed by digesting MOF samples in a mixture of DMSO-d_6 and D_2SO_4, and assessing the ratio of linker to modulator by ^{1}H NMR spectroscopy (Figures S32-S39).

The only major incorporation of L-proline was found to occur in the MOFs of **L5**, which show significant signals in the δ = 1.5-4.5 ppm range. All samples showed resonances assigned to DMSO (δ = 2.5 ppm) and residual DMF (δ = 2.7 and 2.9 ppm) in this region and an acidified water peak at δ ~ 12 ppm. Comparison of the integral ratios suggested that as many as one molecule of L-proline for every four of **L5** is included. The location of this L-proline – be it trapped in the pores, coordinated to the metal clusters as defects or simply surface bound – cannot be determined by this technique, but the high modulator to linker ratio may suggest pore trapping, rather than systematic defects at this high loading (approximately 8-10% *w/w* depending on whether L-proline is assumed to replace **L5** or not).

Of the other MOFs, it seems that a minute amount of L-proline may be retained within **Hf-L8**, but it is a very small amount that may result from insufficient washing. The source of this apparent size-selective incorporation requires additional investigation, but further suggests that the modulator is sterically trapped in the pores.

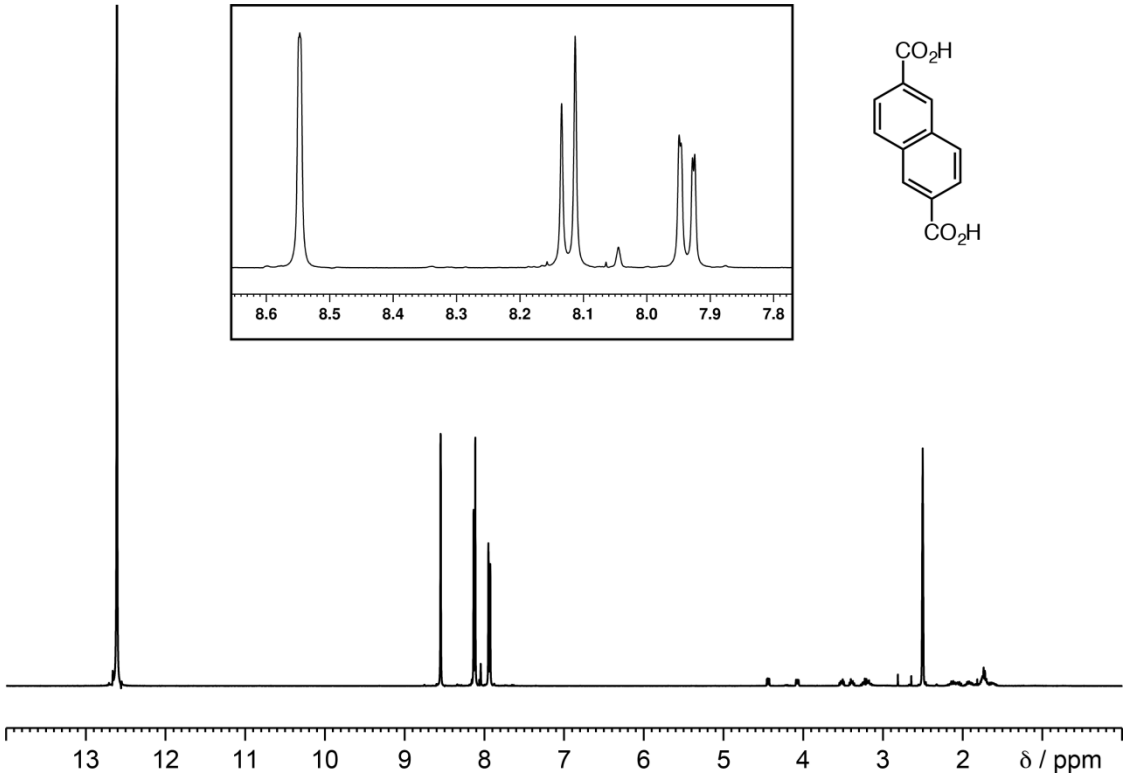

Figure S32. ^{1}H NMR (DMSO-d_6 / D_2SO_4) of digested **Zr-L5** prepared by L-proline modulation.

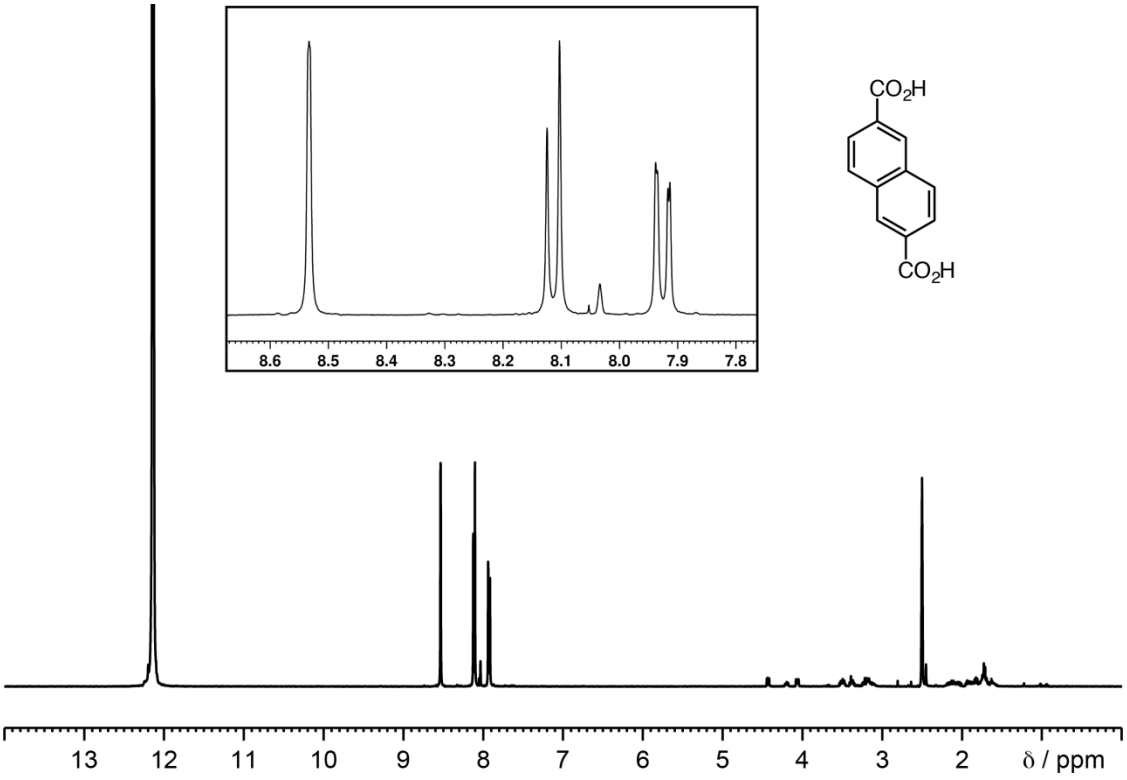

Figure S33. ^{1}H NMR (DMSO-d_6 / D_2SO_4) of digested **Hf-L5** prepared by L-proline modulation.

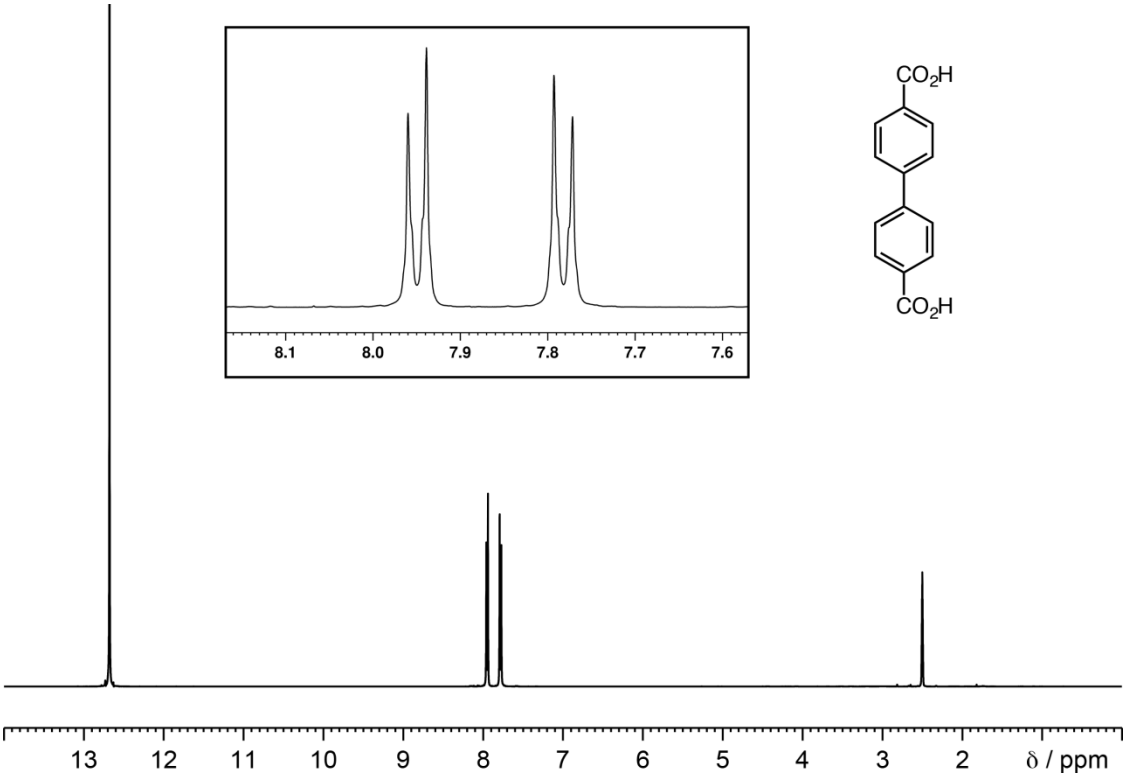

Figure S34. ^{1}H NMR (DMSO-d_6 / D_2SO_4) of digested **Zr-L6** prepared by L-proline modulation.

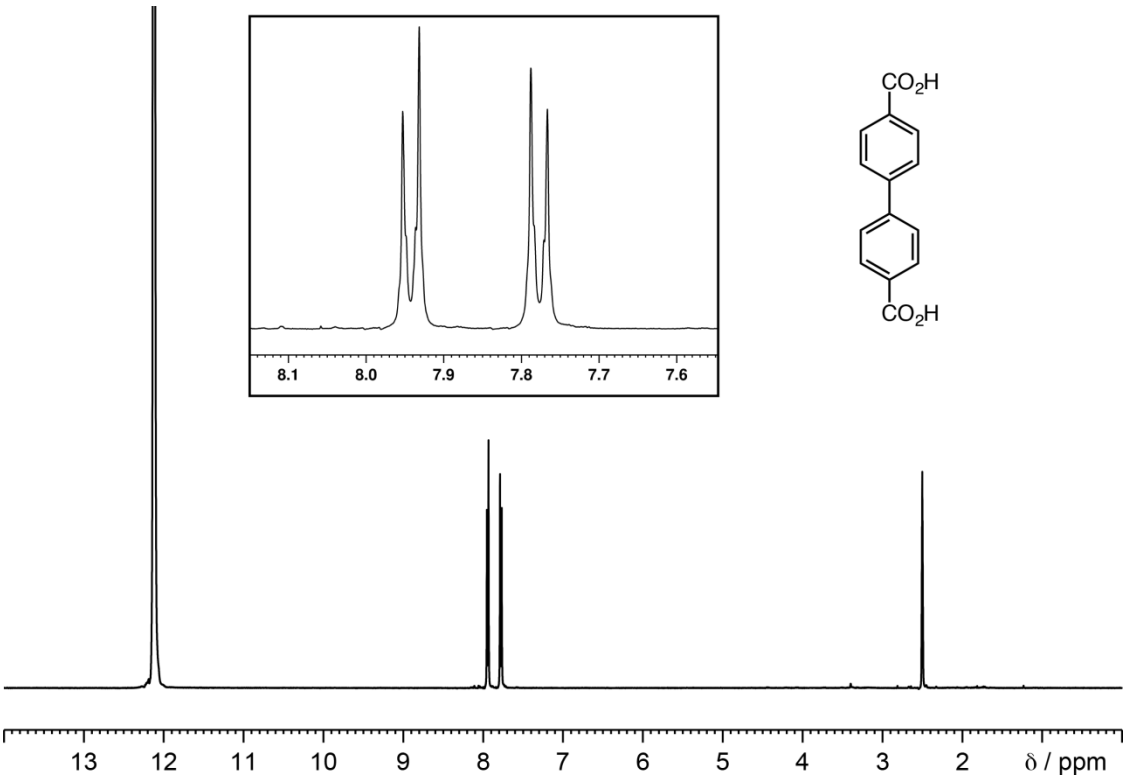

Figure S35. ^{1}H NMR (DMSO-d_6 / D_2SO_4) of digested **Hf-L6** prepared by L-proline modulation.

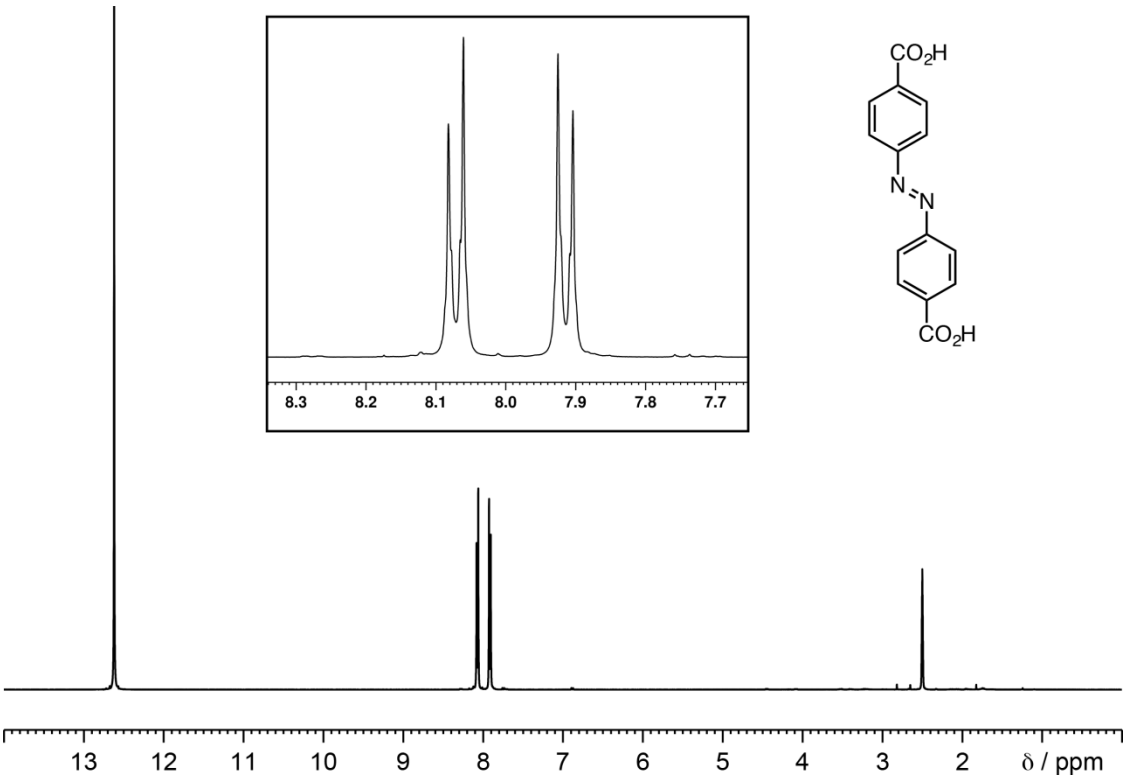

Figure S36. ^{1}H NMR (DMSO-d_6 / D_2SO_4) of digested **Zr-L7** prepared by L-proline modulation.

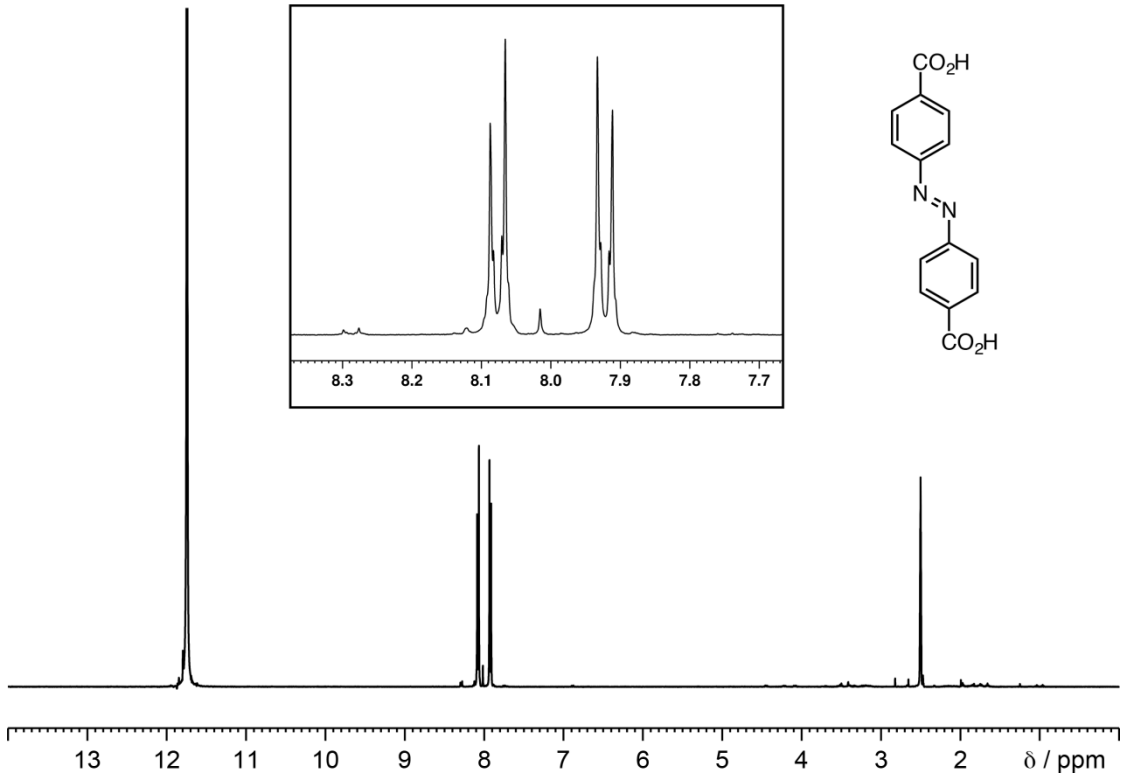

Figure S37. ^{1}H NMR (DMSO-d_6 / D_2SO_4) of digested **Hf-L7** prepared by L-proline modulation.

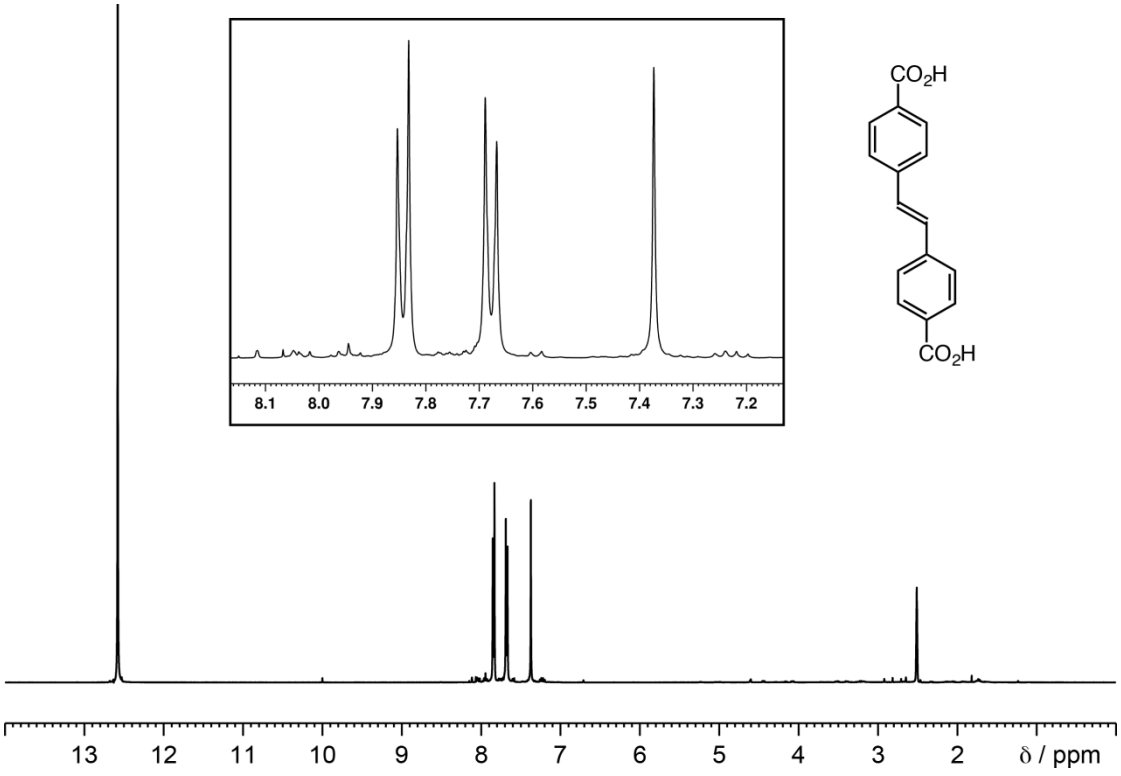

Figure S38. ^{1}H NMR (DMSO-d_6 / D_2SO_4) of digested **Zr-L8** prepared by L-proline modulation.

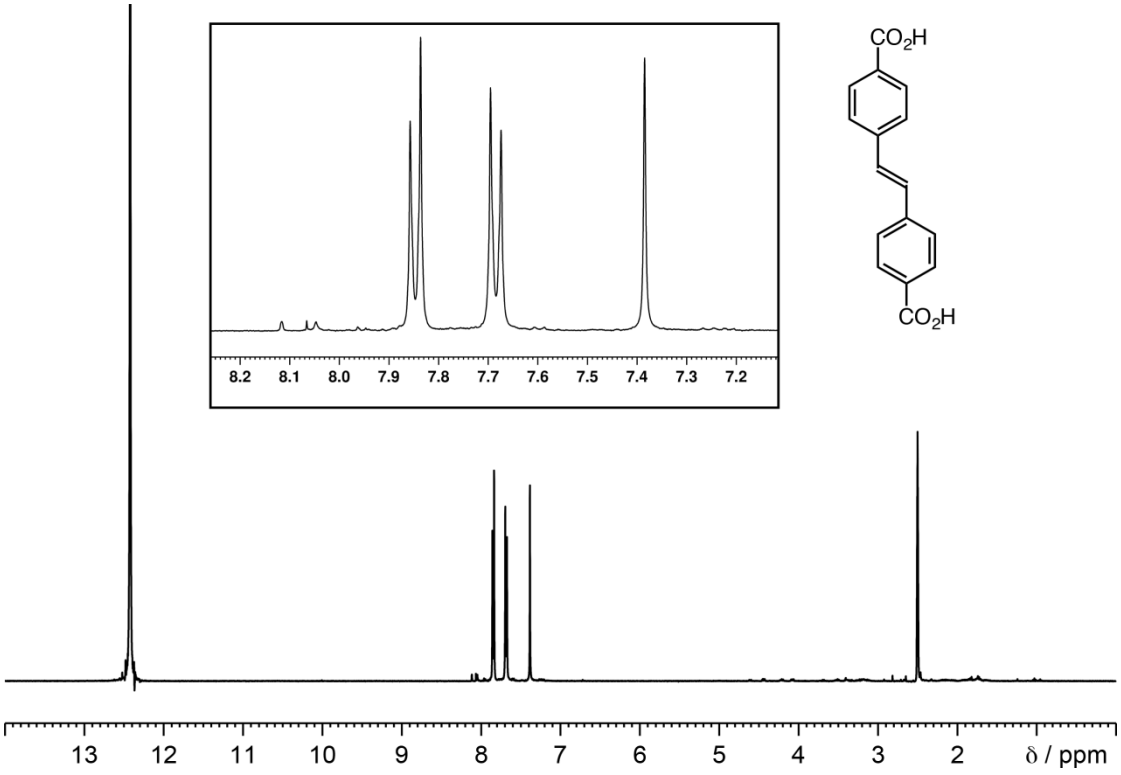

Figure S39. ^{1}H NMR (DMSO-d_6 / D_2SO_4) of digested **Hf-L8** prepared by L-proline modulation.

S11. Thermogravimetric Analysis

Thermogravimetric analysis was used to examine the thermal stability of both the activated Zr and Hf MOFs (Section S10), along with further probing any incorporation of modulators within the MOFs.

The ^{1}H NMR spectra described in Section S10 suggest that L-proline is incorporated into **Zr-L5** and **Hf-L5** in significant quantities, but not so in the other materials examined. TGA profiles of the MOFs are given in Figures S40-S47, and show behaviour similar to that of UiO-66 described previously.[S25] Typically, a small initial solvent loss at lower temperatures (< 250 °C) is followed by a plateau of relative stability until around 500 °C, where a large mass loss occurs that is attributed to degradation of the organic linkers.

In the profiles of **Zr-L5** and **Hf-L5**, an additional mass loss event occurs around 300-450 °C, which indicates the presence of L-proline in the structures, either trapped in the pores or bound to the Zr_6 clusters at defect sites. This loss of mass is likely to be combustion of L-proline, in line with reports of thermal removal of defect bound trifluoroacetate from UiO-66 which occurs at 325 °C.[S31] TGA suggests an L-proline content of 10% *w/w* in each case, which correlates closely to the NMR spectroscopic analysis in Section S10. A very small analogous mass loss event is noticeable for **Hf-L8**, with corresponding minute peaks in the ^{1}H NMR spectrum in the region expected for L-proline.

Comparison of TGA profiles for the analogous Zr and Hf MOFs of the individual ligands (Figures S48-S51) shows that changing the metal from Zr to Hf has little effect on the thermal properties of the MOF. Each pair of profiles shows that the MOFs exhibit the same mass loss events at similar temperatures; **Zr-L5** and **Hf-L5** show loss of incorporated L-proline, for example, while the onset of the combustion of **L6** occurs around 525 °C whether it is bound to Zr or Hf. The mass loss of the Hf analogues is somewhat lower, as a result of the increased molecular weight of Hf, with minor variances a consequence of the slightly differing solvent content in the pores of the MOFs prior to analysis.

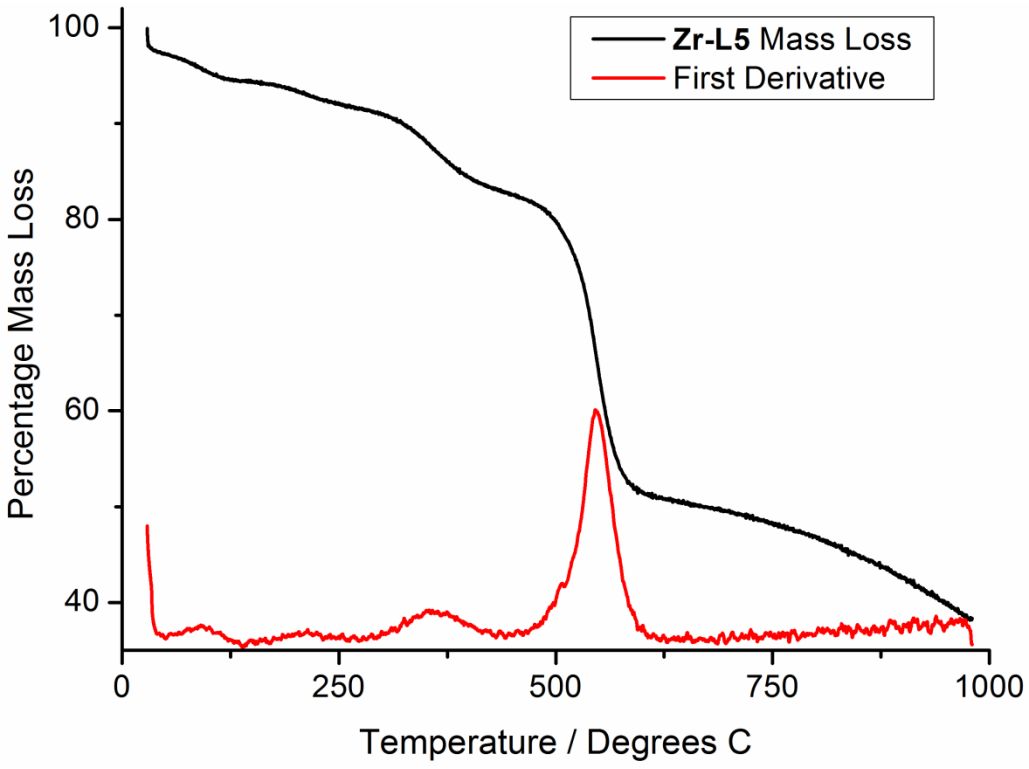

Figure S40. TGA trace of **Zr-L5** with the first derivative showing mass loss events.

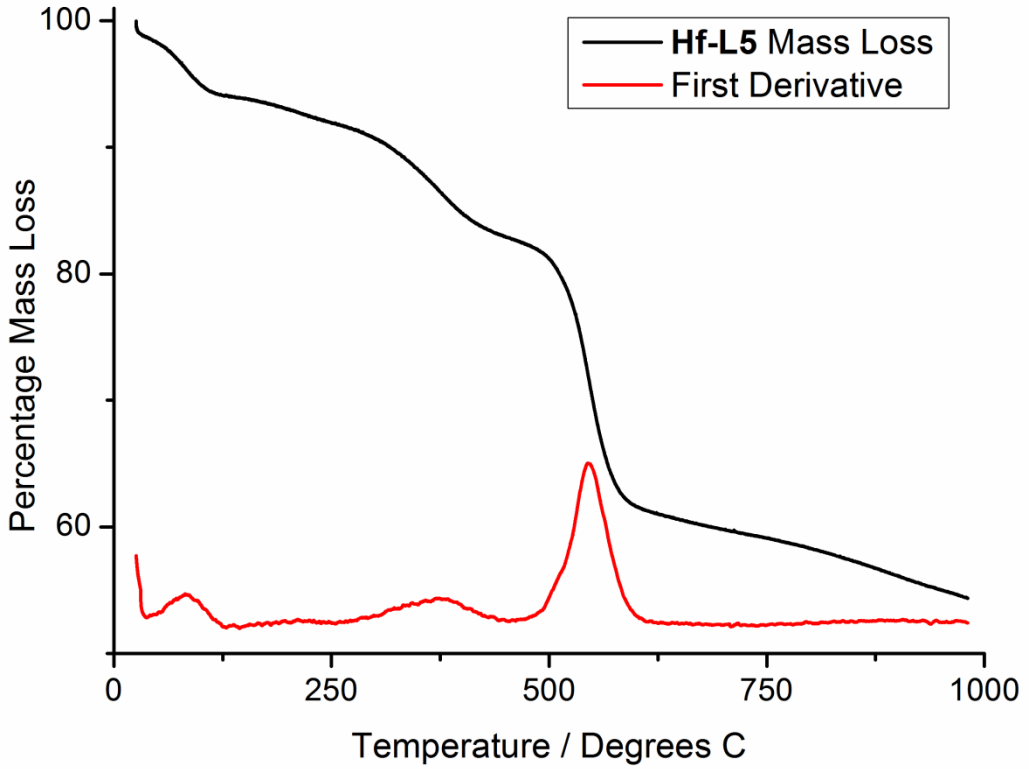

Figure S41. TGA trace of **Hf-L5** with the first derivative showing mass loss events.

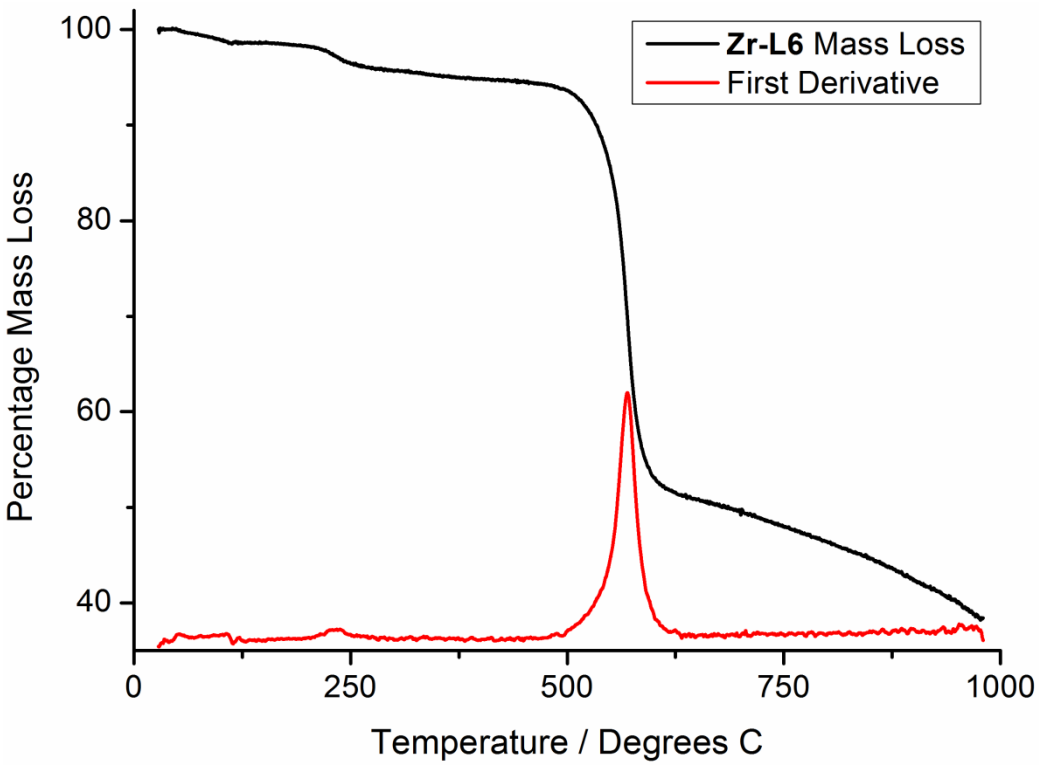

Figure S42. TGA trace of **Zr-L6** with the first derivative showing mass loss events.

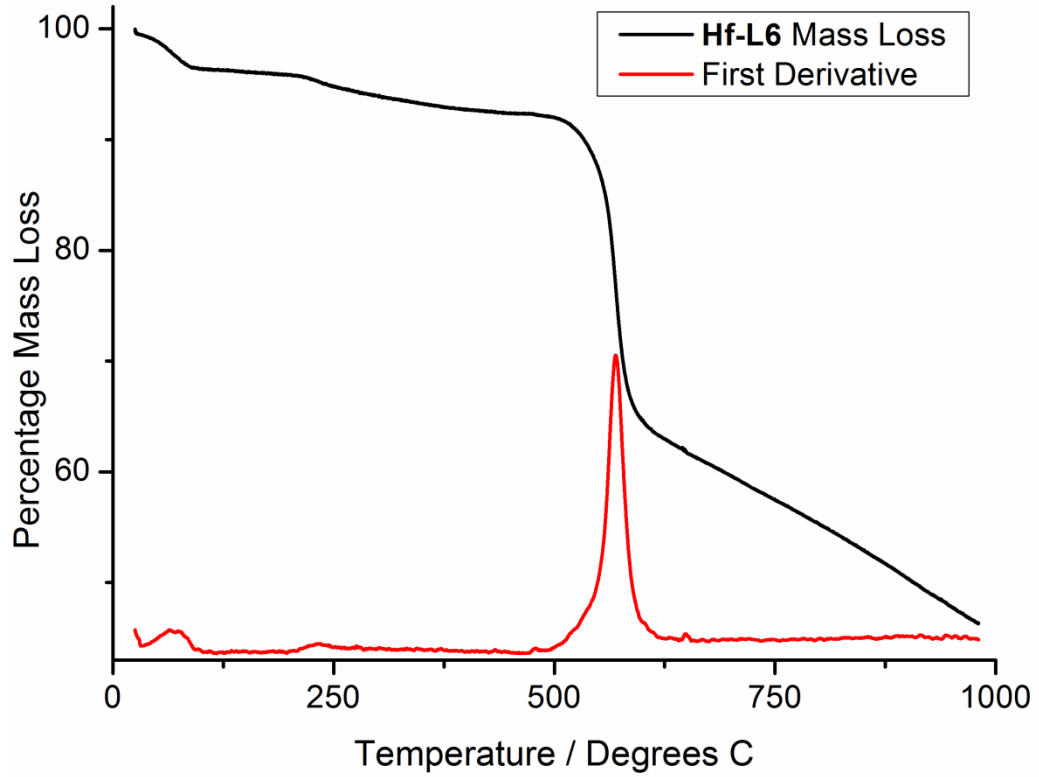

Figure S43. TGA trace of **Hf-L6** with the first derivative showing mass loss events.

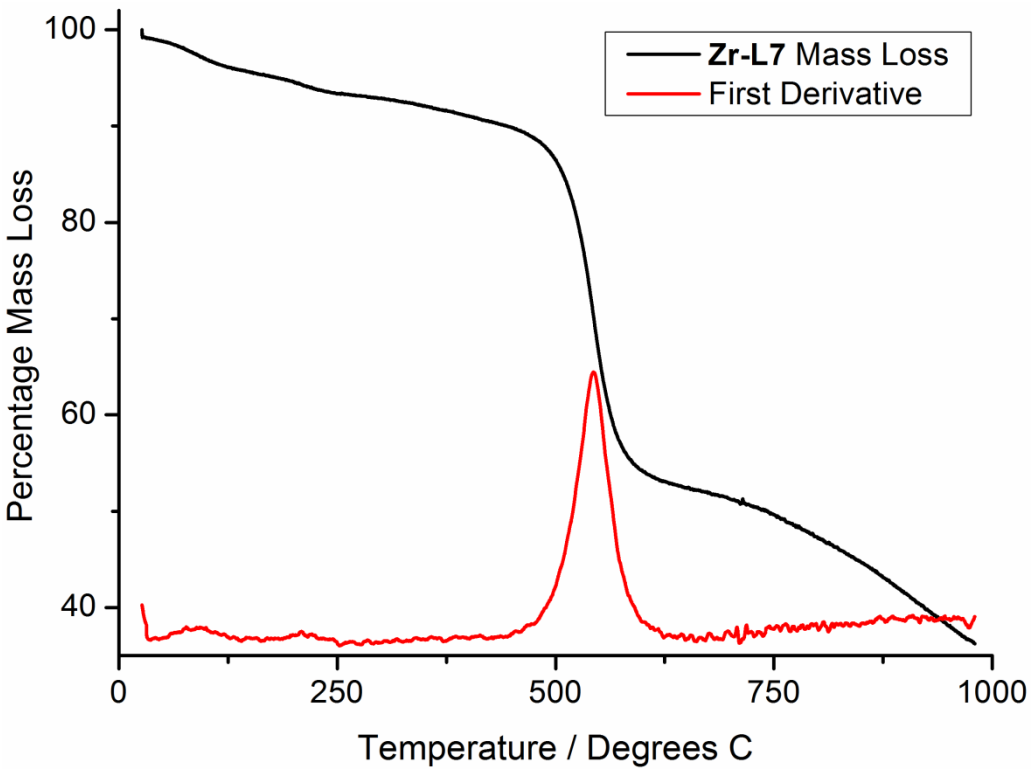

Figure S44. TGA trace of **Zr-L7** with the first derivative showing mass loss events.

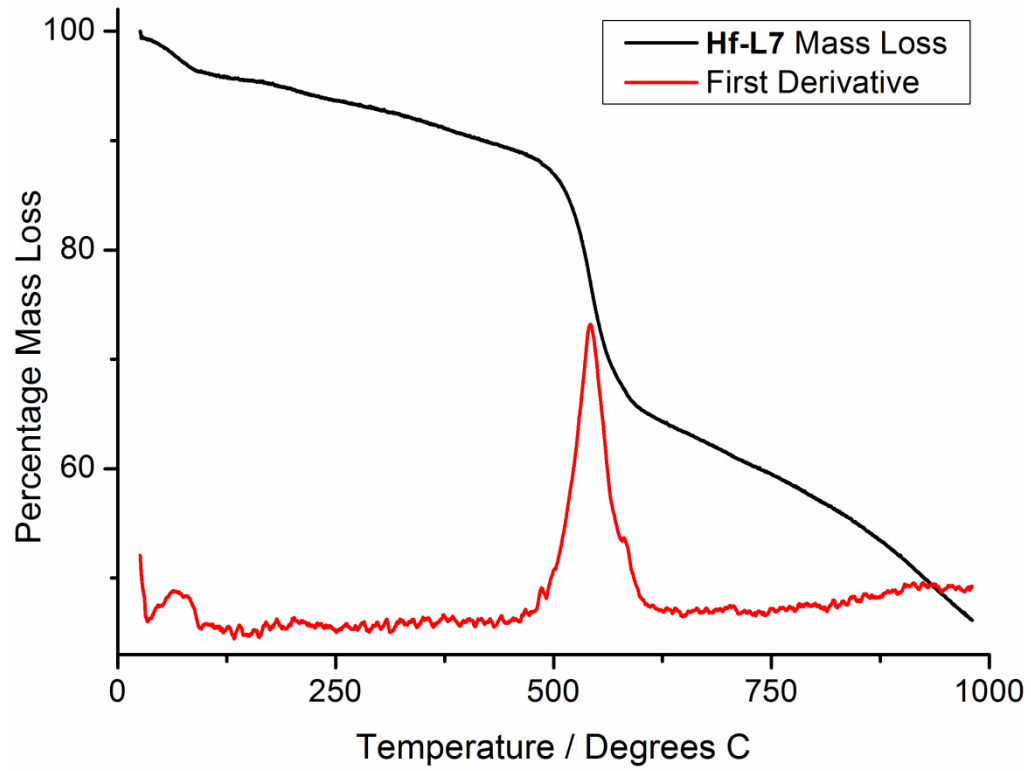

Figure S45. TGA trace of **Hf-L7** with the first derivative showing mass loss events.

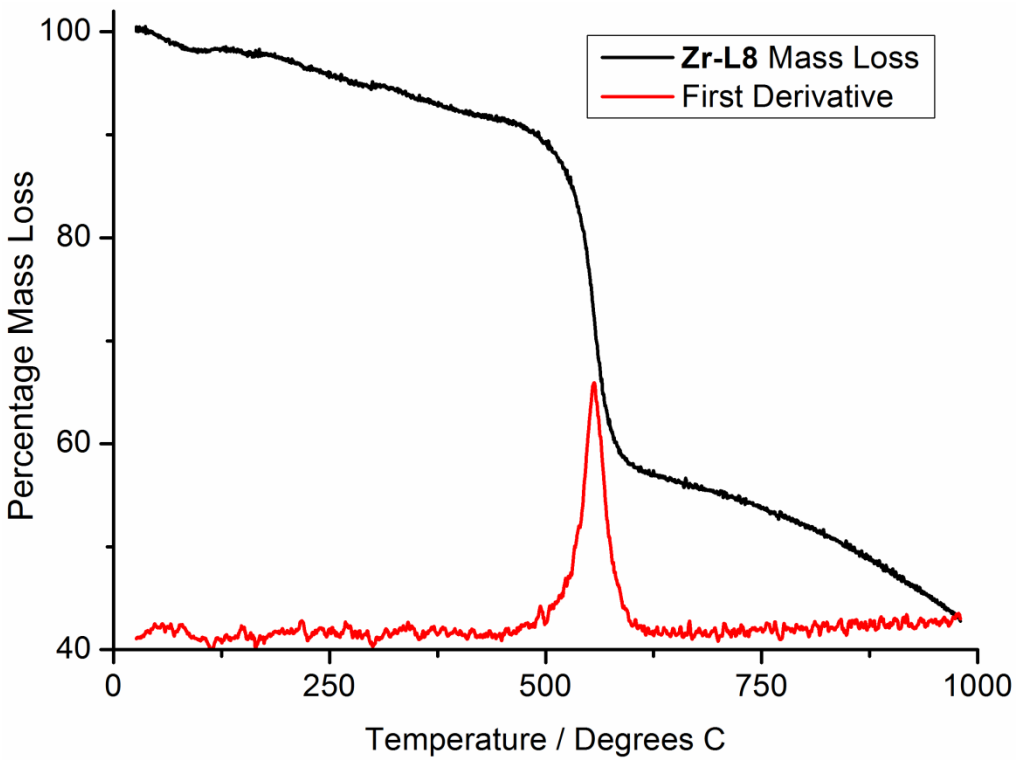

Figure S46. TGA trace of **Zr-L8** with the first derivative showing mass loss events.

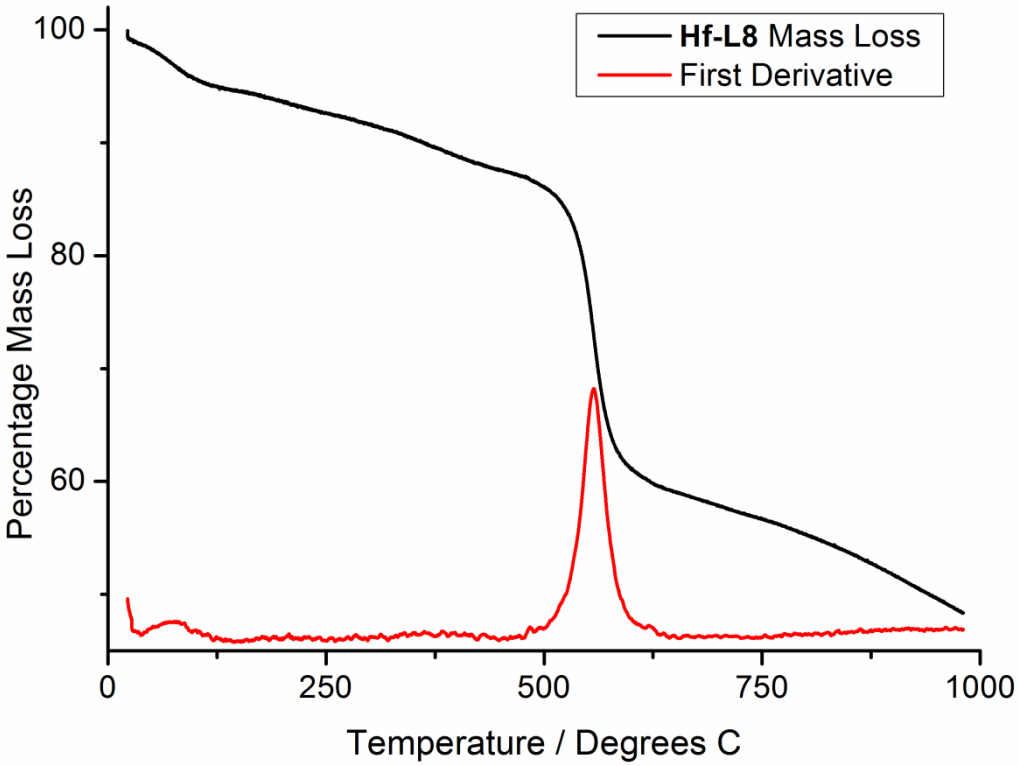

Figure S47. TGA trace of **Hf-L8** with the first derivative showing mass loss events.

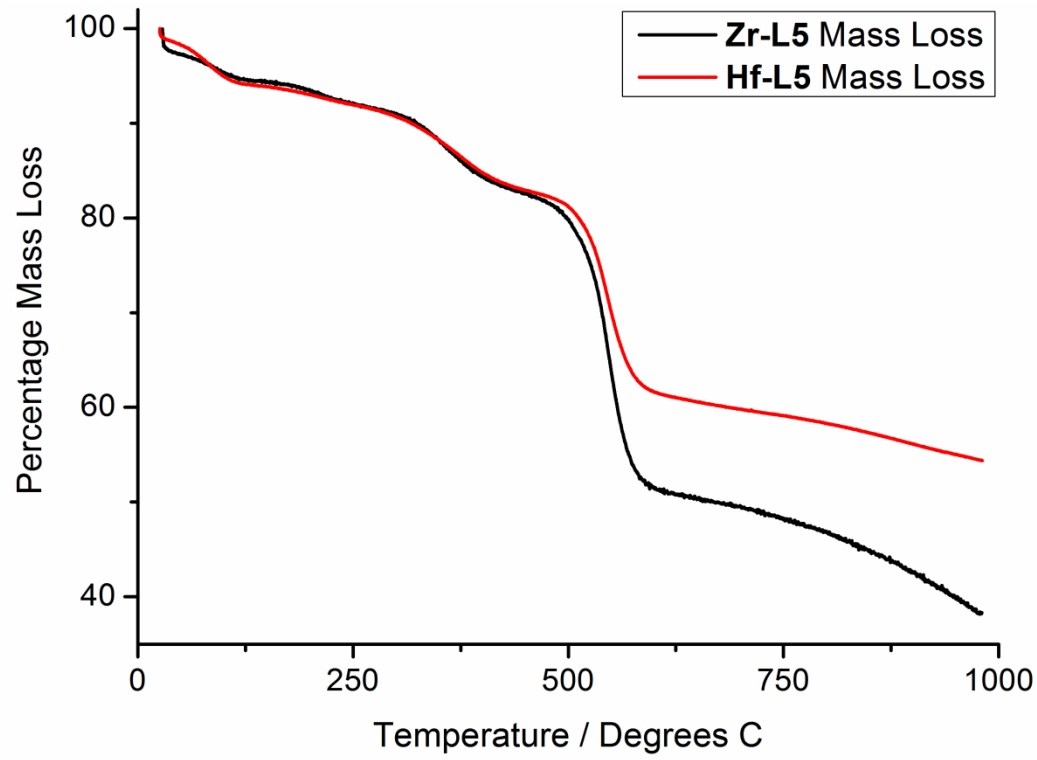

Figure S48. Comparison of the TGA traces of **Zr-L5** and **Hf-L5**.

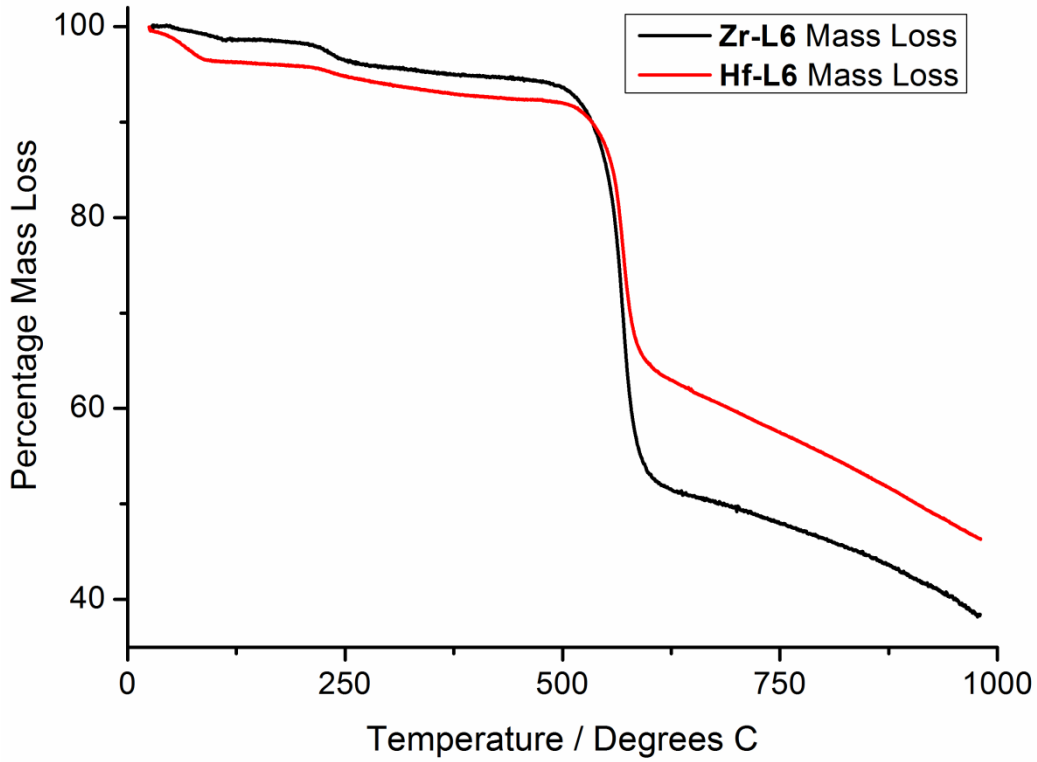

Figure S49. Comparison of the TGA traces of **Zr-L6** and **Hf-L6**.

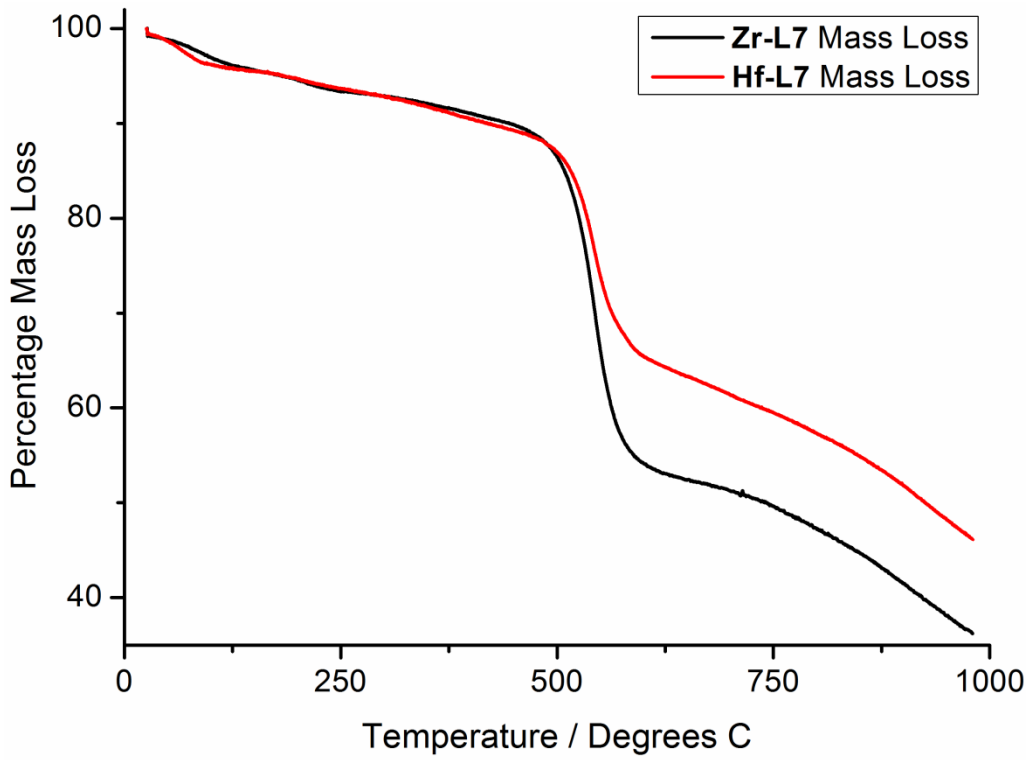

Figure S50. Comparison of the TGA traces of **Zr-L7** and **Hf-L7**.

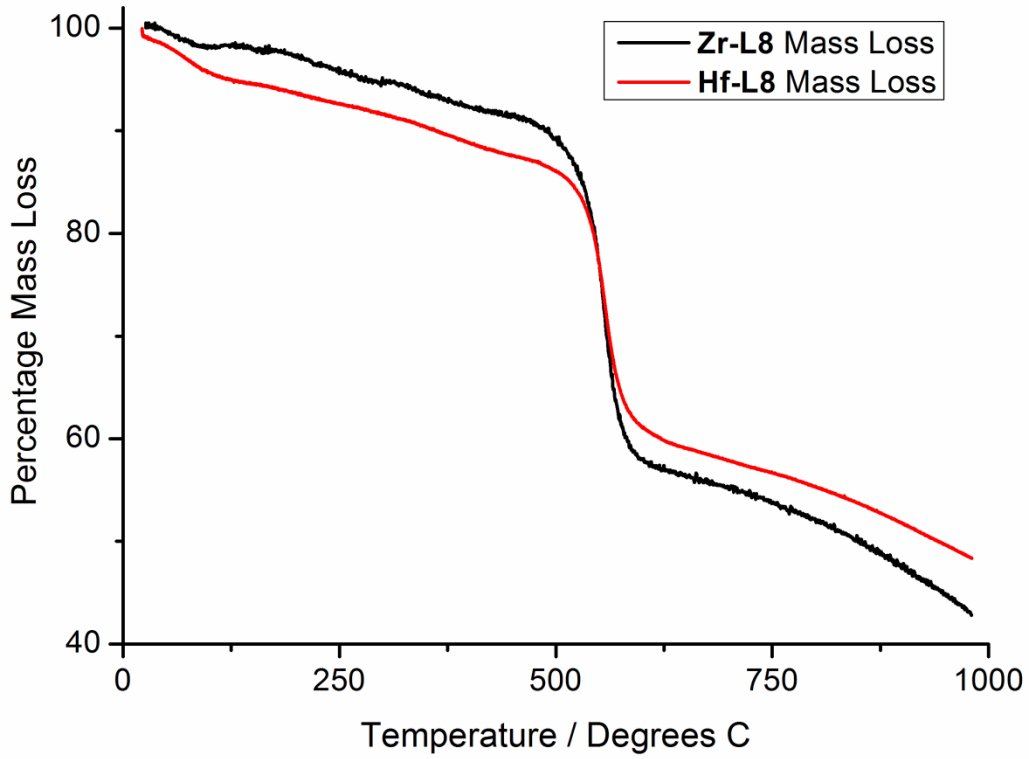

Figure S51. Comparison of the TGA traces of **Zr-L8** and **Hf-L8**.

S12. Surface Area Measurement

The porosities of the exchanged Zr and Hf MOFs of **L5-L8** (Section S10) were examined by N_2 adsorption isotherms collected at 77 K (Figures S52-S59). The samples were further activated by evacuation under vacuum (internal turbo pump) at 120 °C for 20 h. In several cases lower than expected surface areas were obtained, possibly as a result of pore collapse under the THF activation conditions and, as such, chloroform was used to activate **Zr-L7**, **Hf-L5**, **Hf-L7** and **Hf-L8**. The process of chloroform exchange was identical to the THF exchange with the exclusion of being heated in an oven; rather the samples were left to settle at room temperature.

The BET surface areas of the Zr MOFs are close to expected values based on previous reports. The BET surface area of **Zr-L5**, 1300 m^2g^{-1}, corresponds closely to the value derived by Kaskel *et al.* (1400 m^2g^{-1}) when the material was first reported as DUT-52.[S2] Our slightly lower value may be a result of the L-proline included within the material lowering the accessible pore space. **Zr-L6** has a surface area of 2465 m^2g^{-1}, very close to that measured by Hupp and Farha (2500 m^2g^{-1}).[S27] The only previous reports of **Zr-L7** have BET surface areas of (i) 3000 m^2g^{-1} measured by Ar adsorption isotherm,[S33] and (ii) 3200 m^2g^{-1} for N_2 adsorption,[S34] which are again close to the value for our L-proline modulated sample, as measured by N_2 adsorption, of 2830 m^2g^{-1}. **Zr-L8** has a slightly higher BET surface area of 2950 m^2g^{-1}, which is likely a consequence of its slightly larger unit cell volume and hence available pore space.

The Hf MOFs would be expected to have lower gravimetric surface areas compared to their Zr analogues as a consequence of their increased molecular weights. The values measured for **Hf-L6** (1930 m^2g^{-1}) and **Hf-L7** (2270 m^2g^{-1}) decrease by a factor consistent with their change in molecular weight, indicating they exhibit similar porosity to their Zr analogues. The values measured for **Hf-L5** (810 m^2g^{-1}) and **Hf-L8** (2020 m^2g^{-1}), however, are lower than expected, even accounting for the increase in mass. We have been unable to explain this phenomenon, but note that SEM analysis of **Hf-L8** (see Figures S27) shows spherical microcrystalline aggregates rather than discrete single crystals, which may account for the lowering of accessible pore space. Additionally, both MOFs show signs of L-proline incorporation which may further decrease the porosity.

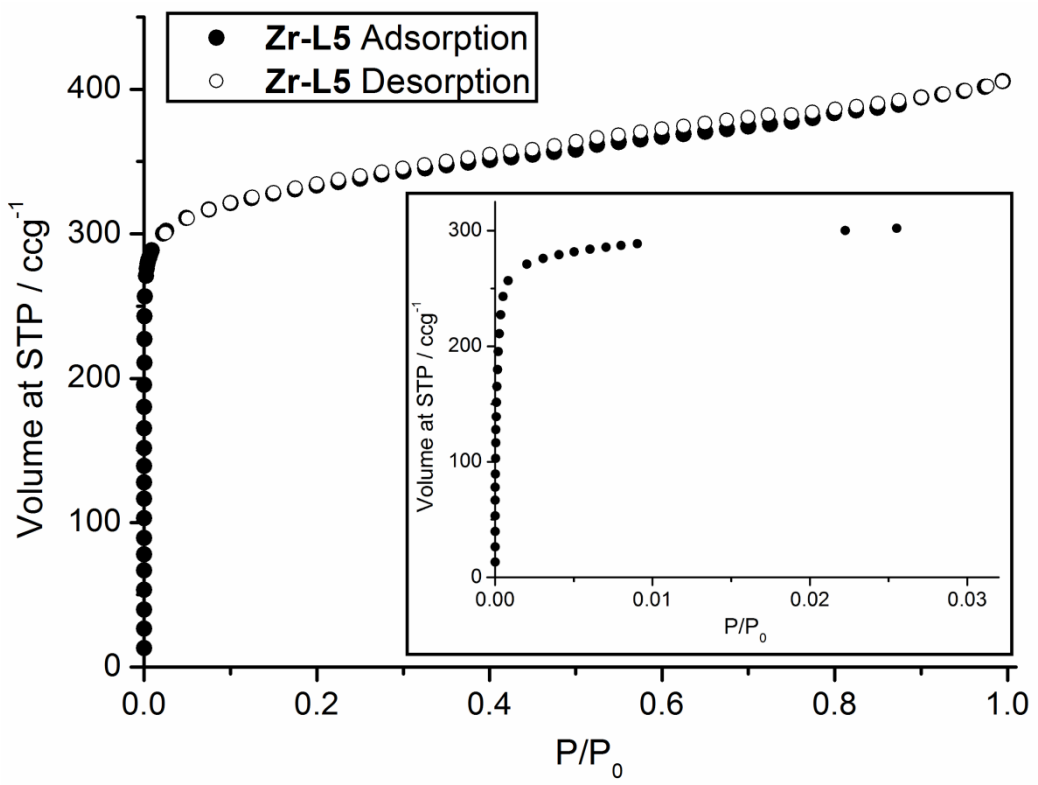

Figure S52. N_2 adsorption isotherm collected at 77 K for **Zr-L5**, which has a BET surface area of 1300 m^2g^{-1}.

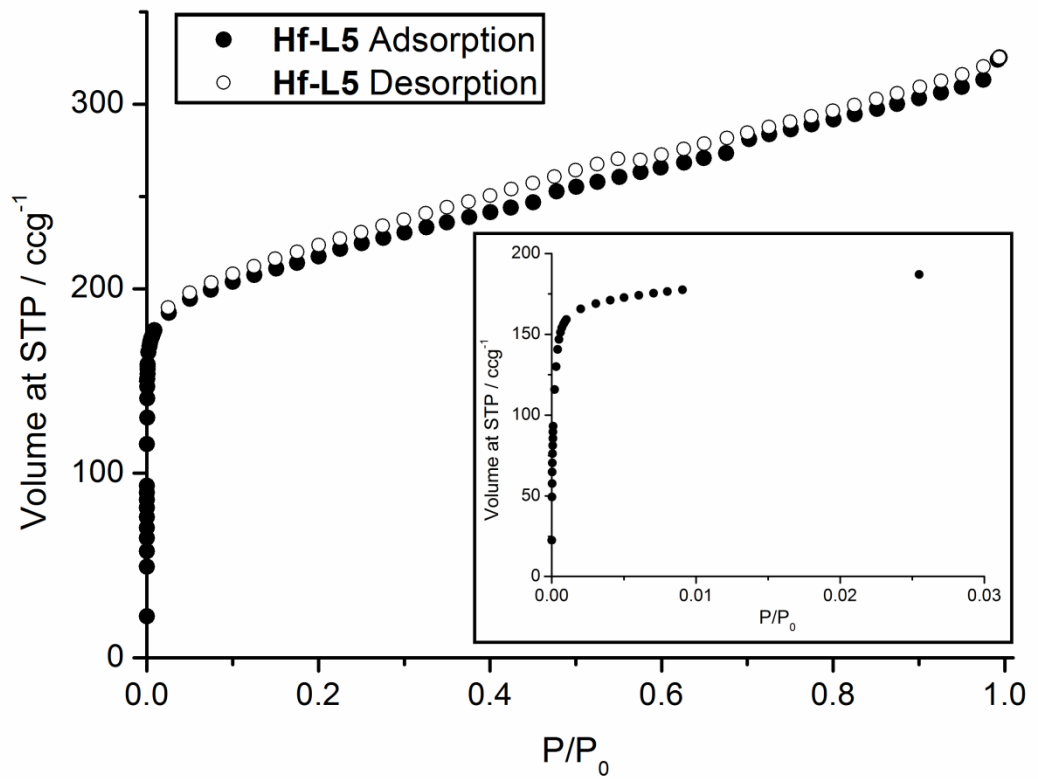

Figure S53. N_2 adsorption isotherm collected at 77 K for **Hf-L5**, which has a BET surface area of 810 m^2g^{-1}.

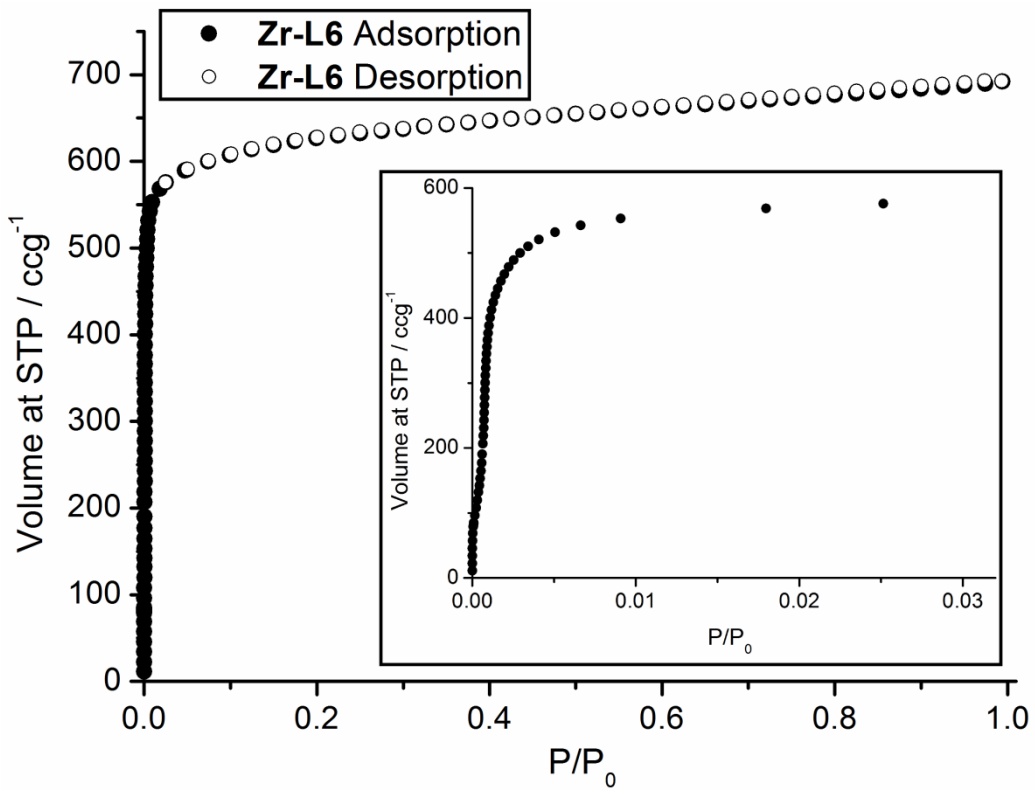

Figure S54. N_2 adsorption isotherm collected at 77 K for **Zr-L6**, which has a BET surface area of 2465 m^2g^{-1}.

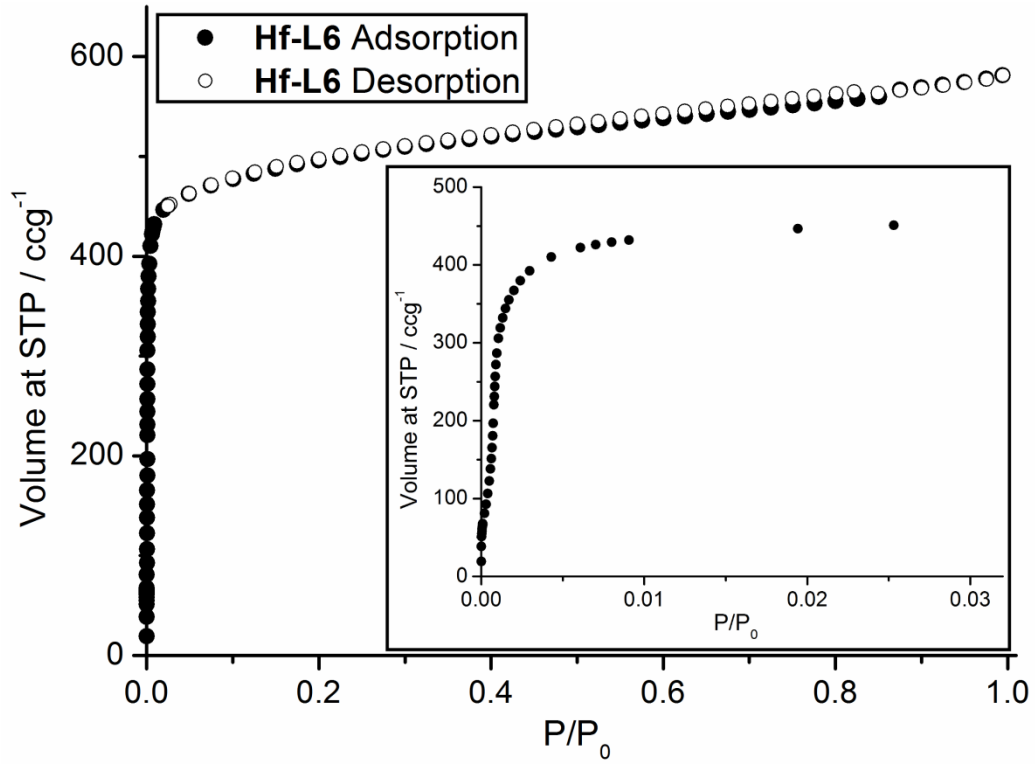

Figure S55. N_2 adsorption isotherm collected at 77 K for **Hf-L6**, which has a BET surface area of 1930 m^2g^{-1}.

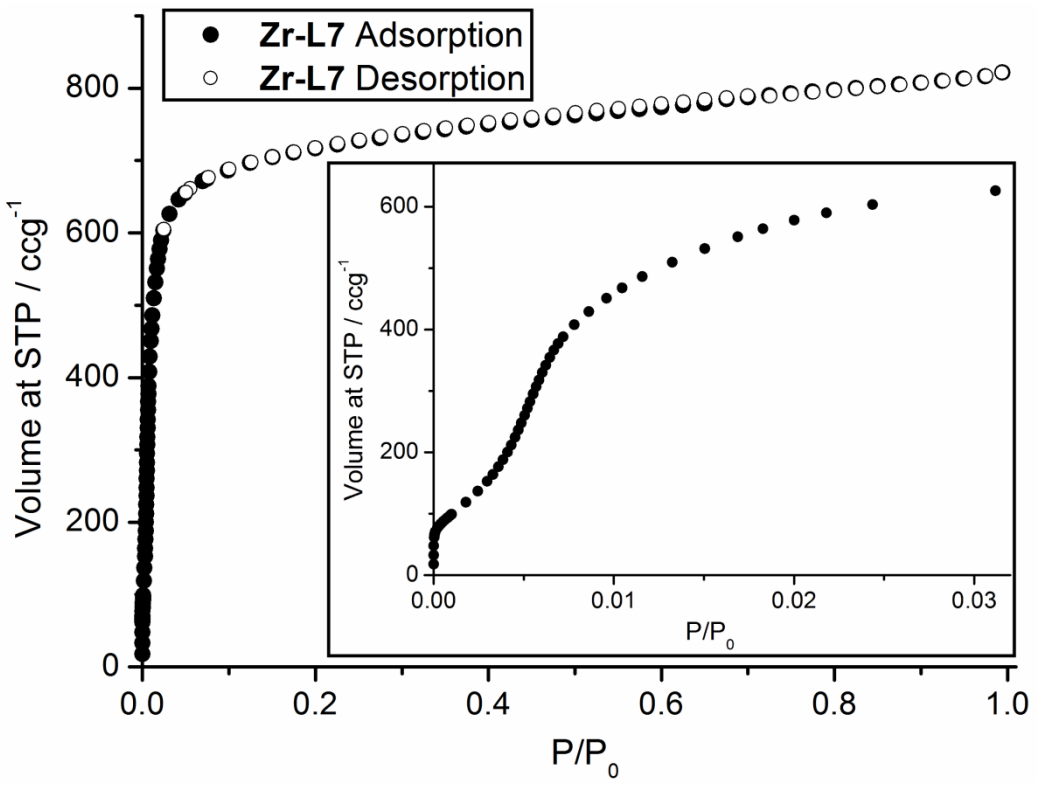

Figure S56. N_2 adsorption isotherm collected at 77 K for **Zr-L7**, which has a BET surface area of 2830 m^2g^{-1}.

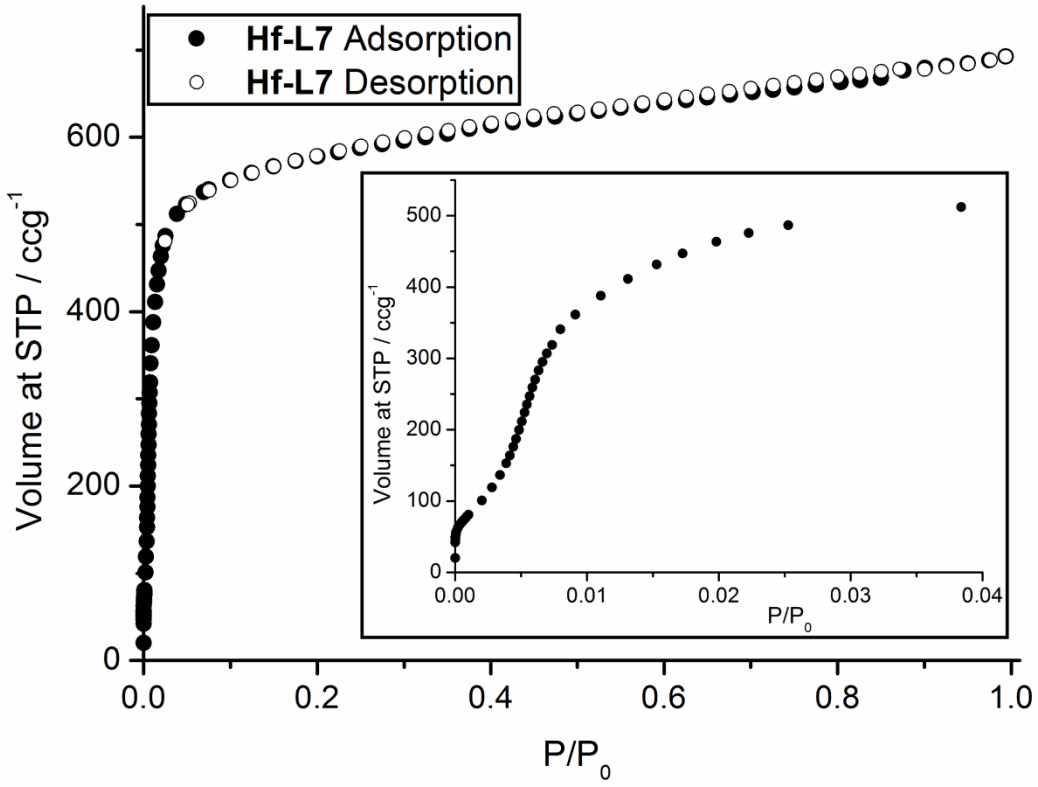

Figure S57. N_2 adsorption isotherm collected at 77 K for **Hf-L7**, which has a BET surface area of 2270 m^2g^{-1}.

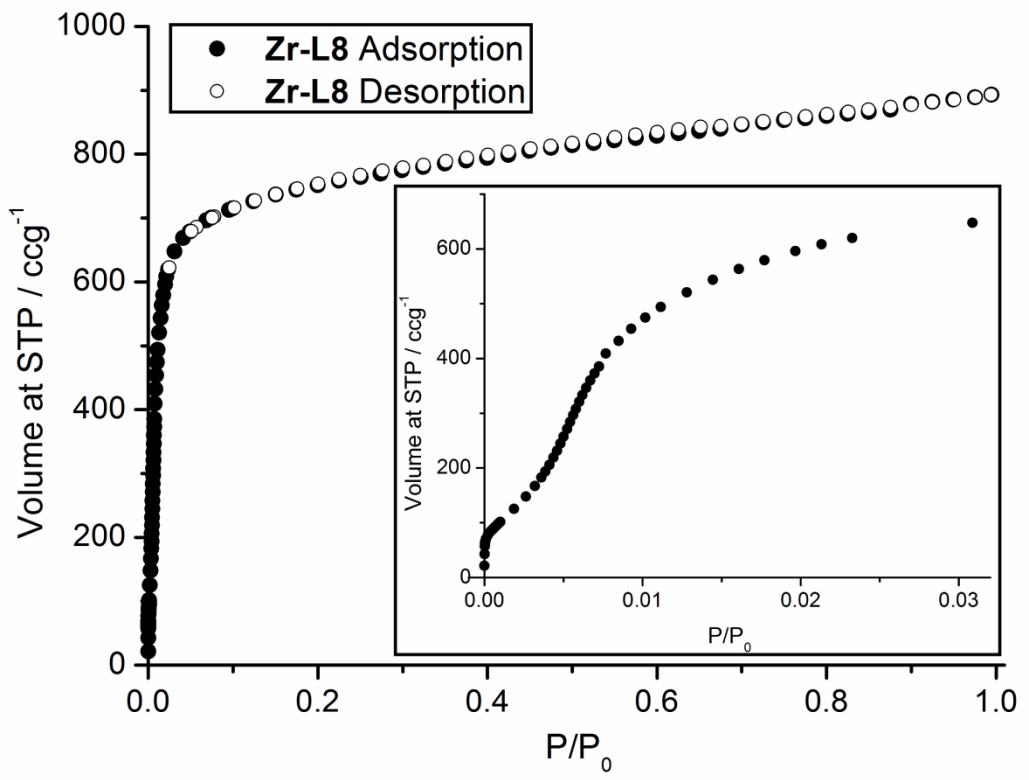

Figure S58. N_2 adsorption isotherm collected at 77 K for **Zr-L8**, which has a BET surface area of 2950 m^2g^{-1}.

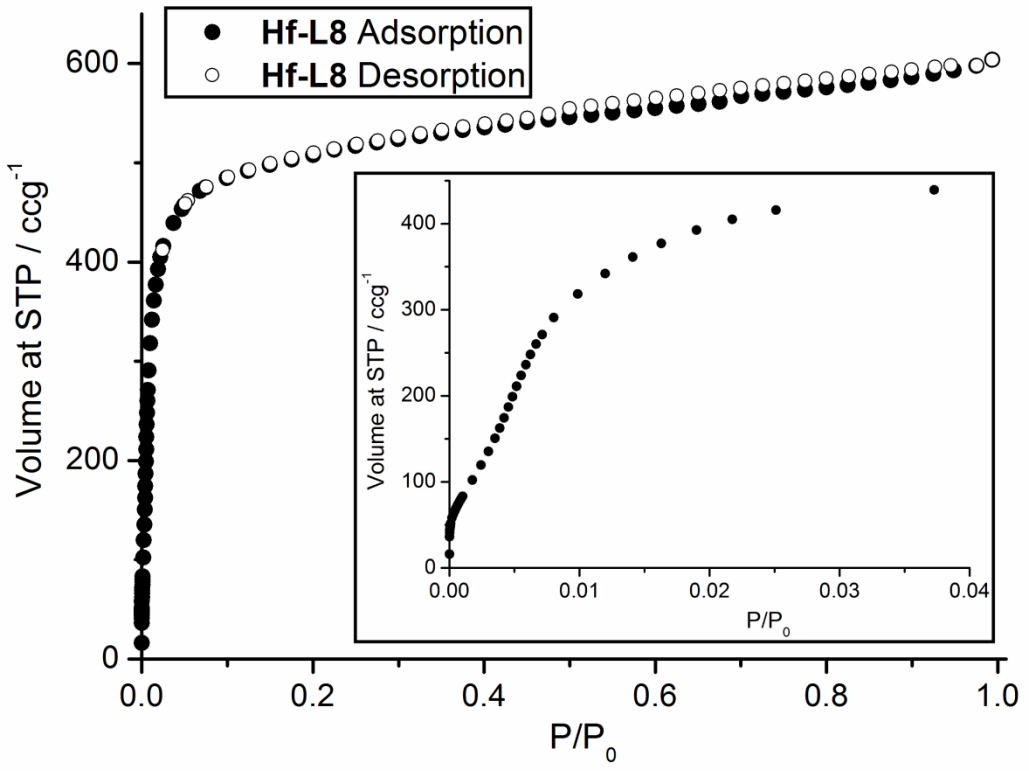

Figure S59. N_2 adsorption isotherm collected at 77 K for **Hf-L8**, which has a BET surface area of 2020 m^2g^{-1}.

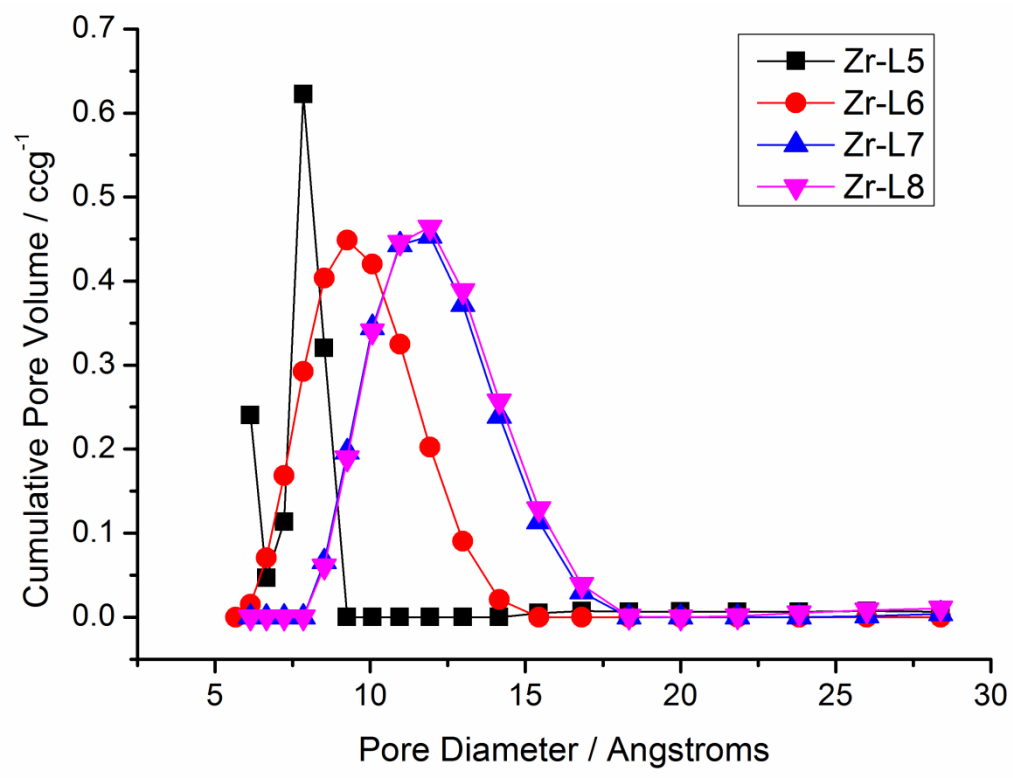

Figure S60. QSDFT-calculated pore size distributions for the Zr MOFs of **L5**-**L8**.

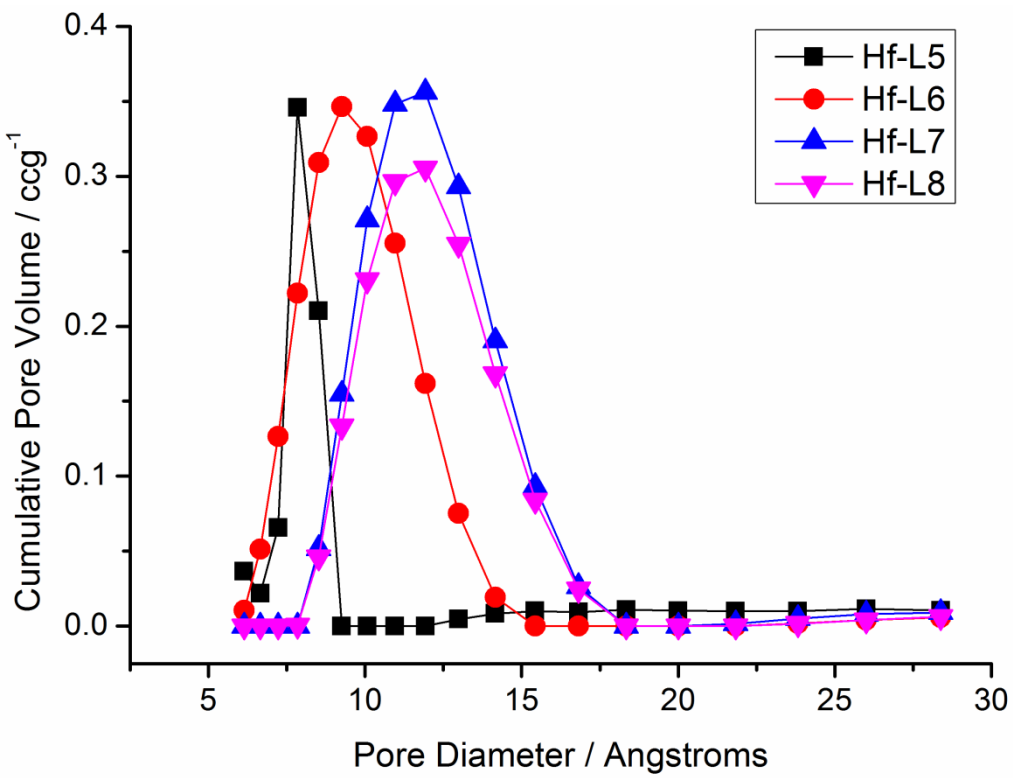

Figure S61. QSDFT-calculated pore size distributions for the Hf MOFs of **L5**-**L8**.

Pore size distributions (Figure S60 and S61) were calculated from the N_2 adsorption isotherms using QSDFT (N_2 on carbon at 77 K, slit/cylindrical pore model) and, for both the Zr and Hf MOFs, show the expected trend of larger pore diameters as the linker length increases. For **Hf-L5** and **Hf-L8** the pore sizes are as expected, being the same diameter as their Zr MOF analogues but with reduced cumulative pore volumes, which would suggest that their lower than expected surface areas result from inaccessible pore space rather than structural deformation.

S13. Modulator Comparison

The efficacy of L-proline as a modulator in comparison to the commonly used modulators, benzoic acid and acetic acid, was examined using the synthetic conditions described in Sections S2 (Zr MOFs) and S8 (Hf MOFs), where five equivalents of the organic modulator was used in concert with one equivalent of HCl. Syntheses of the Zr and Hf MOFs of **L7** and **L8** were attempted and the extent of crystallinity evaluated by PXRD (Figure S62).

While benzoic and acetic acid have found use as modulating agents when used in vast excesses (typically 30 equivalents for benzoic acid and >100 for acetic acid), they are not effective modulators when only five equivalents are used, in stark contrast to L-proline. This reduction in modulator quantity necessary for successful MOF synthesis is expected to improve the cost and efficiency of MOF synthesis.

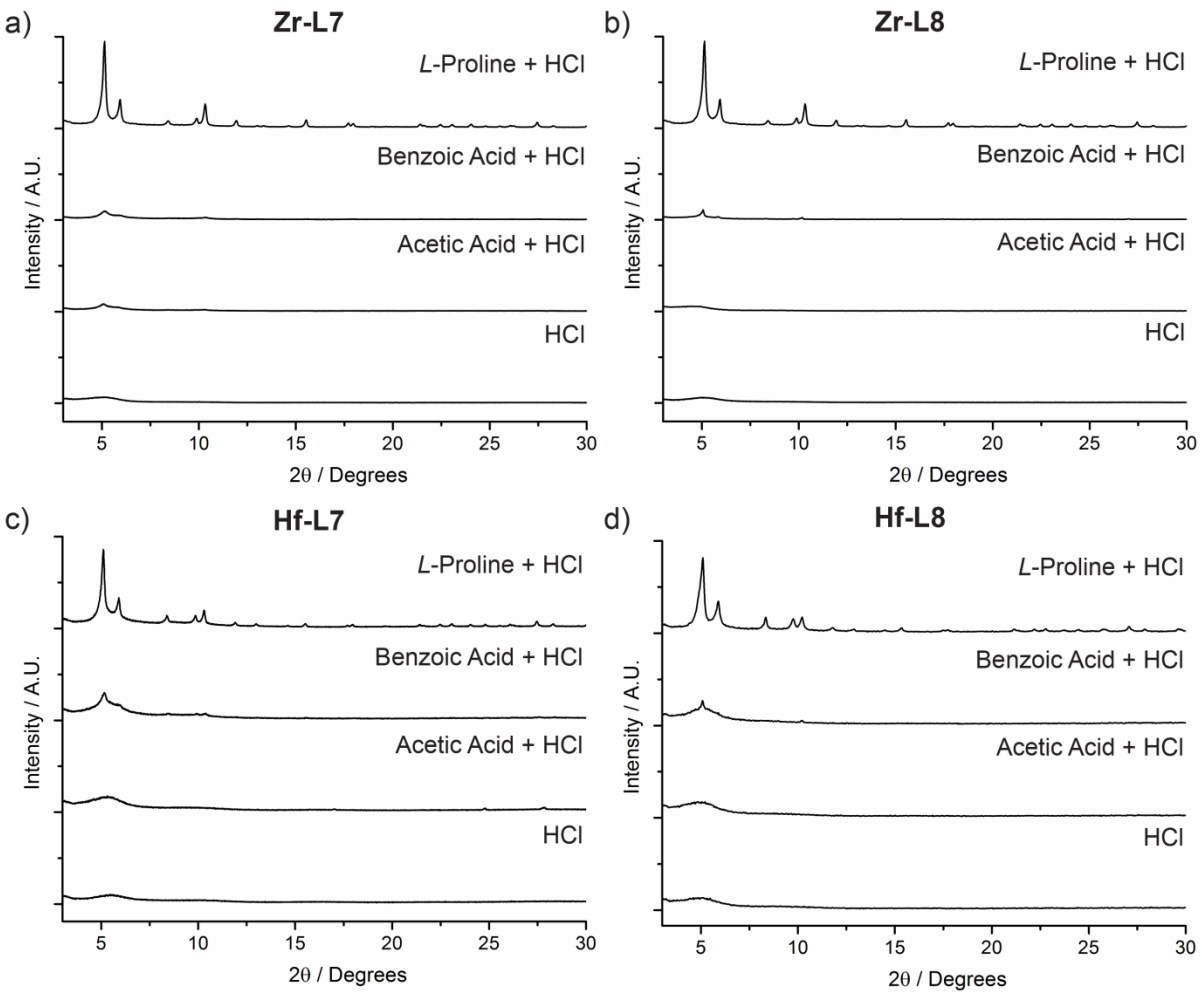

Figure S62. PXRD patterns detailing the efficacy of different modulators in the syntheses of a) **Zr-L7**, b) **Zr-L8**, c) **Hf-L7** and d) **Hf-L8**. One equivalent of HCl and five equivalents of modulator were used in solvothermal syntheses, as per the labelling scheme.

S14. References

S1. Y. Li, Y. Liu, W. Gao, L. Zhang, W. Liu, J. Lu, Z. Wang and Y.-J. Deng, *CrystEngComm*, 2014, **16**, 7037–7042.

S2. V. Bon, I. Senkovska, M. S. Weiss and S. Kaskel, *CrystEngComm*, 2013, **15**, 9572–9577.

S3. G. Nickerl, M. Leistner, S. Helten, V. Bon, I. Senkovska and S. Kaskel, *Inorg. Chem. Front.*, 2014, **1**, 325–330.

S4. S. Øien, D. Wragg, H. Reinsch, S. Svelle, S. Bordiga, C. Lamberti and K. P. Lillerud, *Cryst. Growth. Des.*, 2014, **14**, 5370–5372.

S5. N. Ko, J. Hong, S. Sung, K. E. Cordova, H. J. Park, J. K. Yang and J. Kim, *Dalton Trans.*, 2015, **44**, 2047–2051.

S6. O. V. Gutov, M. G. Hevia, E. C. Escudero-Adán and A. Shafir, *Inorg. Chem.*, 2015, **54**, 8396–8400.

S7. C. Hobday, R. J. Marshall, C. F. Murphie, T. Richards, D. Allan, T. Duren, F.-X. Coudert, R. S. Forgan, C. A. Morrison, S. A. Moggach and T. D. Bennett, *Angew. Chem. Int. Ed.*, 2016, accepted for publication.

S8. R. J. Marshall, T. Richards, C. Hobday, C. F. Murphie, C. Wilson, S. A. Moggach, T. D. Bennett and R. S. Forgan, *Dalton Trans.*, 2016, DOI: 10.1039/C1035DT03178H

S9. J. VandeVondele, M. Krack, F. Mohamed, M. Parrinello, T. Chassaing and J. Hutter, *Comput. Phys. Commun.*, 2005, **167**, 103–128.

S10. A. D. Becke, *Phys. Rev. A*, 1988, **38**, 3098–3100.

S11. C. Lee, W. Yang and R. G. Parr, *Phys. Rev. B*, 1988, **37**, 785–789.

S12. S. Grimme, J. Antony, S. Ehrlich and H. Krieg, *J. Chem. Phys.*, 2010, **132**, 154104.

S13. S. Goedecker, M. Teter and J. Hutter, *Phys. Rev. B*, 1996, **54**, 1703–1710.

S14. C. Hartwigsen, S. Goedecker and J. Hutter, *Phys. Rev. B*, 1998, **58**, 3641–3662.

S15. M. Krack, *Theor Chem Acc*, 2005, **114**, 145–152.

S16. J. VandeVondele and J. Hutter, *J. Chem. Phys.*, 2007, **127**, 114105.

S17. G. J. Martyna, M. L. Klein and M. Tuckerman, *J. Chem. Phys.*, 1992, **97**, 2635–2643.

S18. L. Chen, J. P. S. Mowat, D. Fairen-Jimenez, C. A. Morrison, S. P. Thompson, P. A. Wright and T. Düren, *J. Am. Chem. Soc.*, 2013, **135**, 15763-15773.

S19. M. J. McGrath, J. I. Siepmann, I. F. W. Kuo, C. J. Mundy, J. VandeVondele, J. Hutter, F. Mohamed and M. Krack, *ChemPhysChem*, 2005, **6**, 1894–1901.

S20. J. Schmidt, J. VandeVondele, I. F. W. Kuo, D. Sebastiani, J. I. Siepmann, J. Hutter and C. J. Mundy, *J. Phys. Chem. B*, 2009, **113**, 11959–11964.

S21. A. M. Reilly, S. Habershon, C. A. Morrison and D. W. H. Rankin, *J. Chem. Phys.*, 2010, **132**, 134511.

S22. A. M. Reilly, S. Habershon, C. A. Morrison and D. W. H. Rankin, *J. Chem. Phys.*, 2010, **132**, 094502.

S23. A. M. Reilly, D. A. Wann, C. A. Morrison and D. W. H. Rankin, *Chem. Phys. Lett.*, 2007, **448**, 61-64.

S24. C. F. Macrae, I. J. Bruno, J. A. Chisholm, P. R. Edgington, P. McCabe, E. Pidcock, L. Rodriguez-Monge, R. Taylor, J. van de Streek and P. A. Wood, *J. Appl. Crystallogr.*, 2008, **41**, 466–470.

S25. L. Valenzano, B. Civalleri, S. Chavan, S. Bordiga, M. H. Nilsen, S. Jakobsen, K. P. Lillerud and C. Lamberti, *Chem. Mater.*, 2011, **23**, 1700–1718.

S26. W. Miller, C. W. Smith, D. S. Mackenzie and K. E. Evans, *J. Mater. Sci.*, 2009, **44**, 5441–5451.

S27. M. J. Katz, Z. J. Brown, Y. J. Colon, P. W. Siu, K. A. Scheidt, R. Q. Snurr, J. T. Hupp and O. K. Farha, *Chem. Commun.*, 2013, **49**, 9449–9451.

S28. P. W. Betteridge, J. R. Carruthers, R. I. Cooper, K. Prout and D. J. Watkin, *J. Appl. Crystallogr.*, 2003, **36**, 1487.

S29. A. Spek, *Acta Cryst. C*, 2015, **71**, 9–18.

S30. A. Schaate, P. Roy, A. Godt, J. Lippke, F. Waltz, M. Wiebcke and P. Behrens, *Chem. Eur. J.*, 2011, **17**, 6643–6651.

S31. F. Vermoortele, B. Bueken, G. Le Bars, B. Van de Voorde, M. Vandichel, K. Houthoofd, A. Vimont, M. Daturi, M. Waroquier, V. Van Speybroeck, C. Kirschhock and D. E. De Vos, *J. Am. Chem. Soc.*, 2013, **135**, 11465–11468.

S32. B. Van de Voorde, I. Stassen, B. Bueken, F. Vermoortele, D. De Vos, R. Ameloot, J.-C. Tan and T. D. Bennett, *J. Mat. Chem. A*, 2015, **3**, 1737–1742.

S33. A. Schaate, S. Dühnen, G. Platz, S. Lilienthal, A. M. Schneider and P. Behrens, *Eur. J. Inorg. Chem.*, 2012, **2012**, 790–796.

S34. L. T. M. Hoang, L. H. Ngo, H. L. Nguyen, H. T. H. Nguyen, C. K. Nguyen, B. T. Nguyen, Q. T. Ton, H. K. D. Nguyen, K. E. Cordova and T. Truong, *Chem. Commun.*, 2015, **51**, 17132–17135.